Five-axis Flank Milling and Modeling the Spiral Bevel Gear with a Ruled Tooth Surface Design

Yuansheng Zhou

A Thesis
In the Department
of
Mechanical & Industrial Engineering

Presented in Partial Fulfillment of Requirements
For the Degree of
Doctor of Philosophy (Mechanical Engineering) at
Concordia University
Montreal, Quebec, Canada

September 2015

CONCORDIA UNIVERSITY
SCHOOL OF GRADUATE STUDIES

This is to certify that the thesis prepared

By: Yuansheng Zhou

Entitled: Five-axis Flank Milling and Modeling the Spiral Bevel Gear with a Ruled Tooth Surface Design

and submitted in partial fulfillment of the requirements for the degree of

DOCTOR OF PHILOSOPHY (Mechanical Engineering)

complies with the regulations of the University and meets the accepted standards with respect to originality and quality.

Signed by the final examining committee:

Chair

Dr. Deyi Xue External Examiner

Dr. Liangzhu Leon Wang External to Program

Dr. Chun-Yi Su Examiner

Dr. Ali Akgunduz Examiner

Dr. Zezhong Chevy Chen Thesis Supervisor

Approved by

Chair of Department or Graduate Program Director

September 2015

Dean of Faculty

Abstract

Five-axis Flank Milling and Modeling the Spiral Bevel Gear with a Ruled Tooth Surface Design

Yuansheng Zhou, Ph.D.
Concordia University, 2015

Spiral bevel gears usually are cut by the machine tools which are specifically made for manufacturing spiral bevel gear. For some practical applications, such as repair, prototype, and small batch, there are only several spiral bevel gears need to be machined. It seems not wise to buy a gear manufacturing machine tool for cutting those several gears. Consequently, some other manufacturing methods are introduced to cope with this situation. Recent advances in computer numerical control (CNC) milling machine tools make it possible to manufacture good quality spiral bevel gears. Moreover, CNC milling machine tools are usually cheaper than the specific gear manufacturing machine tools. Even more, they are not only cut gears but also other parts. Therefore, computer numerical control (CNC) milling is introduced in industry to cut spiral bevel gears.

End milling and flank milling are two modes of CNC milling. Compared to end milling, flank milling has been highlighted in quality enhancement, manufacturing time and cost reduction. Theoretically, the result of flank milling a developable ruled surface does not contain geometric deviations.

Hence, flank milling has been widely used to machine the parts with ruled surface or the surface close to ruled surface, such as turbines and blades. Due to the fact that the tooth surfaces of spiral bevel gears are close to ruled surface (the tooth surface of Format-cut spiral bevel is part of a cone), flank milling can also be used to cut spiral bevel gears.

However, there is no literature about flank milling spiral bevel gears. Moreover, the current existing tooth surface models (except the tooth surface of Format-cut spiral bevel gear) are implicit, which makes further calculation inefficient and difficult. To address these two problems, a new ruled tooth surface design is proposed to spiral bevel gears design. Subsequently, the design model is used to be machined with five-axis flank milling by introducing a new tool path planning approach. To obtain the simulate machined tooth surface, a new geometric envelope approach is proposed to calculate the cutter envelope surface as a closed-form representation. Then the result of geometric deviations, which are obtained by comparing the design tooth surface and the simulate machined tooth surface, shows the flank milling is appropriate to cut spiral bevel gears. Furthermore, the conventional face-milled model is also used as the design model for flank milling, and another result of geometric deviations is obtained. Subsequently, both results are compared, and the comparison shows that the proposed design reduces the geometric deviations effectively. Moreover, the closed-form simulate machined tooth surface can only be obtained by using the proposed design.

Keywords: Five-axis flank milling; spiral bevel gear; envelope surface; design; modeling; tooth surface; ruled surface

Acknowledgments

I would like to express my sincere thanks and gratitude to my supervisor Prof. Zezhong Chevy Chen for his invaluable guidance, support and enthusiasm throughout my research. I have gained valuable research experience and significantly improved my technical skills under his supervision.

I am grateful to the supports from CSC (China Scholarship Council) and Concordia University/CSC Joint Scholarship.

The assistance of the faculty and staff of ENCS is appreciated. Thanks to my colleagues. They provide lots of help and create an excellent atmosphere. Although it is boring to mention their names, I have to give my thanks to the following persons, Jiang Zhu, Shuangxi Xie, Chun Du, Liming Wang, Wasif, Mohsens, Aqeel, Sherif, Ruibiao Song, Long Yan, Yongshou Liang, Pengbing Zhao, Yangtao Li, Jiapu Zhu, Minhui Li, Liyong Chang, Hanshi Chen.

Thanks to these friends, Bin Yu, Chen Wei, XingRong Yang, Qiang Wang, Xulong Zhou, Minghui Zhou, Zhengguo Zhou, Guanhan Yao, Ke Xu, Yu Ying and many others. I would like to give my sincere thanks to Wenjuan, Jing and Marianne.

I dedicate this work to my families, my dear parents, sisters and others. They never hesitate to support any my need. I cannot finish my research without their wonderful love, which has been given without any expectation.

Contents

List of Figures

List of Tables

Chapter 1

Introduction

1.1 Background

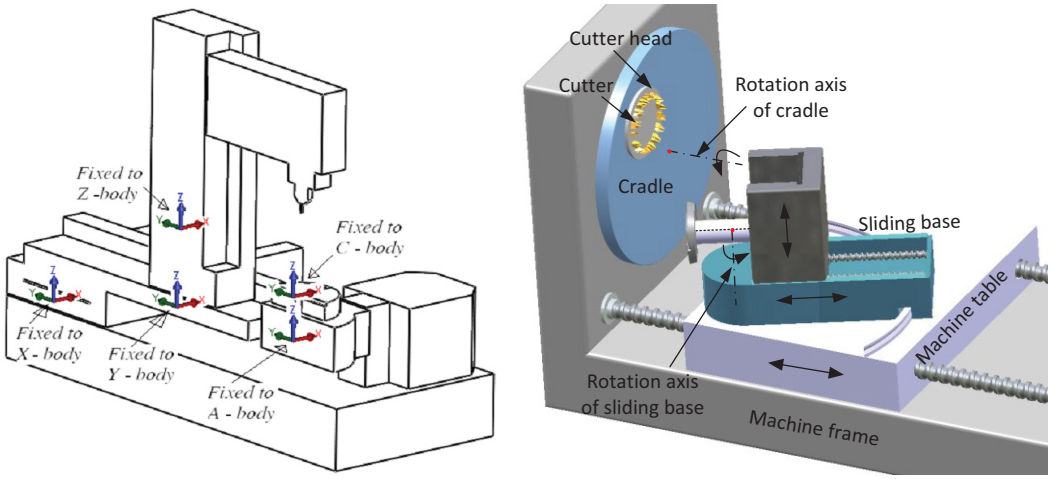

(a) Five-axis CNC milling machine tool

(b) Face-milling machine tool

Figure 1.1: Conventional face-milling machine tool and five-axis CNC milling machine tool.

Spiral bevel gears are significant industry components for power transmission, as in the transmission systems of automobile and helicopter. A spiral bevel gear is the gear with bevel blank and curved teeth. On the one hand, spiral bevel gears have an additional overlapping tooth action in comparison

with straight bevel or spur gears. On the other hand, the manufacturing of spiral bevel gears is more complicated. Three major conventional approaches to manufacture spiral bevel gears are face milling, face hobbing and hobbing. All of those conventional approaches are equipped with special gear manufacturing machine tools, which are relied on the works of corresponding manufacturers, such as Gleason Corporation, Klingelnberg, OC Oerlikon.

Recent advances in computer numerical control (CNC) milling machine tools make it possible to manufacture good quality spiral bevel gears. CNC milling machine tools have different configurations with conventional gear manufacturing machine tools. As shown in Fig. 1.1, a five-axis milling machine is compared with a conventional face-milling machine to cut spiral bevel gears. Due to the different configurations, the methods used for both machine tools to cut spiral bevel gear are also different. The general comparison is summarized in Table 1.1.

Table 1.1: The comparison between CNC milling and face milling

	CNC milling	Face milling	Result of CNC milling
Machine tools	CNC milling machine	Face-milling machine	Cheaper cost
Cutting tools	Milling tools	Special cutting tools	Cheaper cost
Application	Gears, blades, disks, etc	Only gears	Broader application
Cutting time[I]	About 6 hours	Less than 20 minutes	Lower efficiency

I: The cutting time is obtained by approximately estimating to a spiral bevel gear with module of 4.8338 and tooth number of 33. The cutting time of CNC milling is estimated according to machining simulation in CATIA V5R20. For face-milling, it is estimated according to [1].

In summary, although CNC milling has a lower production rate to cut spiral bevel gears than the conventional approaches, it takes advantage of the following aspects: (1) a broad of range of gears can be manufactured

with a CNC milling machine tool; (2) crown gears can also be manufactured; (3) not only gears but also other parts can be machined. Consequently, CNC milling spiral bevel gears has been introduced in industry, especially for the application of small batch, prototype and repair.

1.2 Literature review

1.2.1 Conventional approaches to manufacturing spiral bevel gears

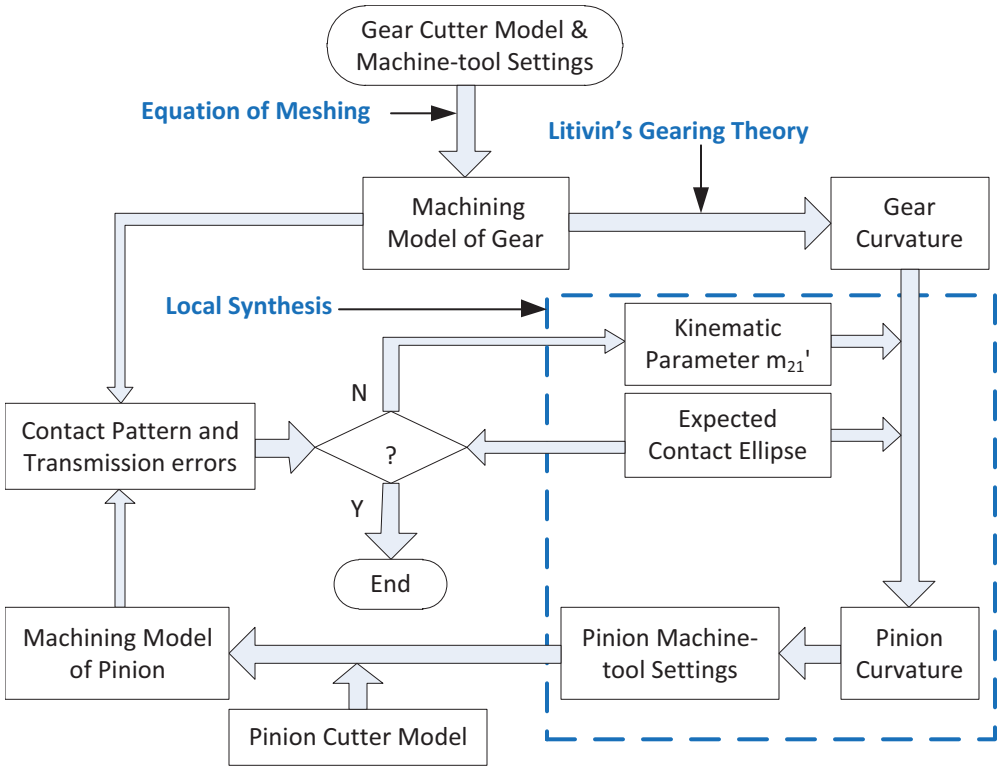

Figure 1.2: The process of conventional approaches.

In the process of the conventional approaches, a series of steps are applied to manufacture the spiral bevel gears to achieve requirements of their work performances. The work performances of a pair of spiral bevel gear are the-

oretically evaluated by two indexes, contact pattern and transmission errors. Both indexes are determined by the geometry of both tooth surfaces of a pair of spiral bevel gears.

Generally, the process used to cut spiral bevel gears in the conventional approaches can be illustrated as Fig. 1.2. It contains the following three major steps. (1) The bigger member of a pair of spiral bevel gear, named gear, is manufactured primarily according to some basic work requirements. Based the cutter geometry and machining settings, the mathematical model of the gear tooth surface can be obtained. (2) With the geometry gear tooth surface, the cutters and machining settings for pinion, which is the smaller member of a pair of spiral bevel gears, are determined. Subsequently, the mathematical model of the pinion tooth surface is also obtained. (3) The contact pattern and transmission errors can be calculated according to the tooth surfaces of both gear and pinion. In some cases, it may be an iteration process since the requirements of contact pattern and transmission errors could be not satisfied by the result of step (3). In a word, the whole process is to generate the reasonable shapes of tooth surfaces by choosing the right cutters and machining settings. Subsequently, the result satisfies the requirements of the work performances.

Some well-established knowledge methodologies have been used for manufacturing the spiral bevel gears in conventional approaches. Specially, the now classic Litvin's approach has been widely applied in conventional approaches to manufacture spiral bevel gears, as shown in Fig. 1.2. There are several significant methodologies in Litvin's approach, such as the equation

of meshing, theory of gearing, local synthesis [2–6]. These methodoogies are summarized as follows.

- The equation of meshing is developed by litvin et al. to calculate the gear tooth surface. With the consideration of the gear generating process, the tooth surface can be represented as an implicit form of three parameters, and one of which has to be eliminated according to a necessary condition of the generating process. This necessary condition is written as the equation of meshing. The equation of meshing is referred to as envelope theory in the filed of CNC milling.
- With the tooth surface model, curvature analysis is necessary to investigate the contact pattern and transmission errors of the gear drive. Mathematically, curvature analysis can be implemented with the results of classic differential geometry [7]. However, since the tooth surface of the generated gear is expressed as an implicit form with the equation of meshing, it is complicated and inefficient to calculate the derivatives of the tooth surface with differential geometry approach. Subsequently, the alternative approaches are proposed to curvature analysis. Litvin et al. proposed theory of gearing to do curvature analysis for conjugated surfaces. In this now classic approach, a systematic methodology is established to derive the curvature relationship between two conjugate surfaces based on the analysis of the motion of the contact point. This method employs kinematic relationships and scalar components in an orthogonal reference frame, and it does not use the parametric coordinates.

- Local synthesis to calculate the pinion machining settings based on the contact ellipse of gear and pinon at a chosen point. Since the contact ellipse is determined by the curvatures of the gear and pinion, the pinion curvature is determined while given the gear curvatures and contact ellipse. Subsequently, the machining settings for the pinion are obtained by applying the theory of gearing.

There are some other works besides the aforementioned works. Based on the equation of meshing, envelope surface and its curvature analysis can be implemented with different methods. These methods can be categorized into two groups, Litvin's and invariant approaches, depending on whether the derivation process is related with coordinate systems or not. In the following literature review, the tooth surface generation is introduced separately with both approaches. Subsequently, the curvature analysis based on both approaches is also illustrated respectively.

Based on the equation of meshing, Fong and Tsay [8] calculated the tooth surface model for circular cut spiral bevel gears. Tsay and Lin [9] proposed a mathematical model for different types of hypoid gears. Shih et al. [10] introduced a universal hypoid generator mathematical model for face hobbed spiral bevel and hypoid gears. Lelkes et al. [11] generated the model for Klingelnberg bevel gears. Fan [12] proposed a complete modeling of a face-hobbed spiral bevel gear by expressing the machine-tool settings as a function of the cradle increment angle. Vimercati [13] modeled the tooth surface of face-hobbed hypoid gears with the accurate geometric representation. Xie [14] proposed a genuine cutter geometric model for the spiral bevel and hypoid

gears by defining the cutting edges on the blade rake face. Muhammad [15] introduced a new approach to CNC programming for an accurate model of multi-axis face-milling of hypoid gears. Chen et al. [16] introduced the generalized motion to represent the gear generation motions to obtain the gear tooth surface model. Puccio et al. [17] calculated the tooth surface model by applying the invariant approach, where the geometric relations in gear generation are described as vectorial forms. Subsequently, a more general case of the gear generation with supplemental motion is also introduced [18]. Wang and Zhang [19] extended the invariant approach with tensor expression.

Different from Litvin's approach, the invariant approach describes the gear generating process without referring to coordinate systems, and this makes the overall formulation compact. Two significant issues of the invariant approach are vector (or tensor) expression and motion description. Wu and Luo [20] used vector expression to formulate gear generation, and Dooner [21] introduced screw theory to describe the kinematic motion. Puccio et al. [17] represented gear generation based on geometric relations in vectorial form, and a more general case [18] of the gear generation with supplemental motion is introduced subsequently. Wang and Zhang [19] extended the invariant approach with tensor expression.

With the tooth surface geometry, the curvature analysis has been investigated. Chen [22] introduced non-principal parametric coordinates and developed curvature expression in a given direction in a non-orthogonal reference frame. The case with the generalized motion has been developed by Chen et al. [16]. Wu and Luo [20] obtained the curvature equations by introduc-

ing screw theory to describe the relative motion of conjugate surfaces, and Yan and Cheng [23] applied this approach to some cam-follower mechanisms. Ito and Takahashi [24] investigated curvatures in hypoid gears with classic differential geometry and kinematic relationships. Dooner [21] proposed the third law of gearing with screw theory to obtain the limiting relationship between the curvatures of two conjugate surfaces. Puccio et al. [25] used the invariant approach to do curvature analysis of conjugate surfaces. An extension of the invariant approach to the general case of the gear generation with supplemental motions is introduced consequently [18]. Puccio et al. [26] gave a comprehensive comparison in different methods and expressed all these methods with vector form. Wang and Zhang [19] developed the invariant approach with rotation and curvature tensors to illustrate theory of gearing and local synthesis.

All of the above research calculates the tooth surface based on the equation of meshing, and the derivatives of the equation of meshing are used to investigate curvature analysis with alternative approaches. However, the whole calculation process can be more simple and straightforward. To fulfill these purposes, a new geometric meshing theory is proposed in this thesis in Section 2. If we follow the convention of CNC milling, the geometric meshing theory is called as geometric envelope approach. We will use geometric envelope approach in the remainder of this thesis.

1.2.2 CNC milling approaches to manufacturing spiral bevel gears

Over the last few decades, the progress of CNC milling spiral bevel gears has aroused public concern in gear manufacturing industry. It has been applied in the traditional gear manufacture companies, such as Gleason Corporation, DMG Mori, etc. According to the tool position and orientation with regard to the machined surface, CNC milling has two modes, flank milling (also referred to as side or peripheral milling) and end milling. End milling removes the material around the midst of the tool flat end, while it is along the flank side of the tool in flank milling. End milling spiral bevel gears has been implemented in some works [27–29]. Besides the machining time, there are two other limitations for end milling spiral bevel gears. First, the scallop will be generated among two adjacent tool paths. Consequently, the further manufacturing process may be needed to satisfy high qualify requirement. Second, it is very difficult to obtain the simulate machined tooth surface, which is the fundamental input to evaluate work performances prior to the real machining.

From the view of design, Huston and Coy [30] described the tooth surface of an ideal spiral bevel gear with the involute curve and logarithmic spiral. Since the involute curve has been widely used in spur gears and helical gears, Huston and Coy applied it as the profile. A logarithmic spiral is chosen as the lengthwise curve of the crown gear, and then it is spindled from the disk into a cone. Later, Huston and Coy [31] gave the analysis of the tooth surface design for circular cut spiral bevel gears. Although the designs proposed by

Huston and Coy [30,31] are difficult to be machined by the conventional gear manufacturing machine tools [32], the fundamental idea has been introduced for CNC milling spiral bevel gears, such as the works in [27–29]. Suh et al. [27] designed the tooth surface by rotating the spherical involute curve along the circular cut spiral curve. Subsequently, the design tooth surface is machined by both four-axis and 3/4 axis CNC milling. Moreover, Suh et al. [28] also designed spiral bevel gears with crown, and then machined in four-axis CNC milling machine tools. Alves et al. [29] designed the tooth surface by applying the spherical involute tooth profiles along a logarithmic spiral on the pitch cone. Then the tooth surface is machined with five-axis CNC milling. All the manufacturing modes in [27–29] are end milling. Consequently, as mentioned before, it is very difficult to obtain the simulate machined tooth surface prior to the real machining. Measurements are applied in [27–29] to obtain the machined models of the tooth surface after machining.

Compared to end milling, flank milling has many advantages in quality enhancement, manufacturing time and cost reduction [33, 34]. Theoretically, five-axis flank milling the developable ruled surface does not contain geometric deviations (or geometrical deviations, which are the differences between the design surface and the simulate machined surface). Therefore, it has been widely used to machine the parts with ruled surface, even some generic free-form surfaces. For a detailed insight on five-axis flank milling, readers can refer to [35]. However, there is no literature about flank milling spiral bevel gears, and no ruled tooth surface design available for spiral bevel gears.

1.2.3 The calculation of envelope surface

Theoretically, the tooth surface model of spiral bevel gears is part of the envelope surface of the cutter along the given tool path. Hence, it is significant to calculate the envelope surface in gear manufacturing. In the filed of gear manufacturing, the approaches as stated in Section 1.2.1 apply the equation of meshing to calculate the envelope surface. Moreover, there are also some mathematical algorithms developed in the filed of CNC milling to compute the envelope surface, such as sweep-envelope differential equation (SEDE), singularity theory (also referred to as manifold stratification or Jacobian rank deficiency method) and envelope theory. Blackmore et al. [36, 37] proposed the SEDE algorithm to compute the envelope surface and applied it in CNC machining simulation. Wang et al. [38] extended the SEDE method to the general deformed envelope surface. Abdel-Malek and Yeh [39, 40] used an implicit equation to calculate the envelope surface by introducing the Jacobian rank-deficiency condition. In the later work [41], this approach was developed to the consecutive sweeps of n parameters. Subsequently, it was applied to calculate the material removed in the five-axis CNC machining process. The basic idea of the envelope theory is sourced from differential geometry [42]. Wang et al. [43] used the tangency condition of the envelope theory to obtain the envelope surface by computing a family of grazing curves. Martin and Stephenson [44] and Weld and Leu [45] initially adopted the envelope theory to formulate the envelope surface.

The envelope surface of general objects is studied by several approximate

methods. Kim et al. [46] approximated the swept volume of a complex polyhedron along a given trajectory. Rossignac et al. [47] computed the envelope surface of a free-form solid by introducing a polyscrew approximation of the screw motion. Erdim and Ilieş [48] proposed a generic point membership classification approach to compute the envelope surface of 3-dimensional objects in general motions. Juttler and Wagner [49] summarized the basic theory of spatial rational B-spline motions and introduced a linear control structure. Subsequently, the envelope surface swept out by a moving polyhedron is calculated. Xia and Ge [50] introduced the exact non-uniform rational B-splines (NURBS) representations of the envelope surfaces of the swept volume of a cylinder undergoing a rational Bézier or B-spline motions. Yang et al. [51] computed the approximate swept volumes of NURBS surfaces or solids by slicing NURBS surfaces into sliced curves.

The applications of the envelope surface to CNC machining simulation are studied in several approaches. Chen and Cai [52] applied the envelope surface to three-axis virtual milling of sculptured surfaces. Bohez et al. [53] presented an algorithm based on the sweep plane approach to determine the machined part geometry in five-axis CNC machining with the general cutter of automatically programmed tool (APT). Park et al. [54] proposed a hybrid cutting simulation methodology based on a general discrete vector model.

Many researchers have taken much effort to apply the envelope theory to five-axis CNC machining. Yang and Lee [55] presented a nonparametric R-map model to describe discrete surfaces to obtain machined surface. Chiou and Lee [56] presented a shape-generating approach to find the envelope sur-

face by constructing G-buffer models for five-axis CNC machining. Maeng et al. [57] proposed a Z-map method to compute the intersection points between a set of z-axis aligned vectors and the envelope surface. Chung et al. [58] proposed a single valued function to represent the envelope surface for the generalized cutter in three-axis CNC machining. In this work, the grazing curves were calculated with the silhouette curve equations. Roth et al. [59] presented a modified principle of silhouettes to determine the grazing curves on the envelope surface of a toroidal cutter in five-axis CNC machining. Later this method is extended by Mann and Bedi [60] to compute the envelope surface of all rotary milling cutters in five-axis CNC machining. Lee and Nestler [61, 62] applied the gauss map to compute the envelope surface of a cutter undergoing simultaneous five-axis movement. In this work, the complete envelope surface with self-penetration (or self-intersection) is also presented. Based on envelope theory, all these approaches in [55–62] computed the envelope surface with numerical methods.

The closed-form methods are also widely studied based on envelope theory. Hu and Ling [63] generated the envelope surface of the natural quadric surface by introducing the instantaneous screw axis to describe the sweep motion. Chiou and Lee [64] presented a closed-form solution to the envelope surface of the APT cutters to simulate five-axis CNC machining. Subsequently, this method was used to optimize the cutter configuration for five-axis tool-end machining [65] and five-axis ruled surface machining [66]. Lartigue and Affouard [67] calculated the envelope surface by kinematic approach to correct the tool path in five-axis flank milling. Weinert et al. [68] proposed an an-

alytical method to calculate the envelope surface of a fillet end cutter for five-axis CNC milling based on the moving frame method, which simplify the calculation. Du et al. [69] extended this method to APT cutters with several different formulas for different cutters, such as fillet end, ball end and flat end. In addition, they presented solution analysis and special case analysis. Zhu et al. [70] calculated the envelope surface of the general rotary cutter undergoing general spatial motion for multi-axis machining. Gong and Wang [71] presented two closed-form solutions for calculating the envelope surface of a generic cutter directly from CL data based on the moving frame.

By combining with the envelope theory, the theory of two-parameter families of spheres (or referred to as sphere congruence) has been introduced to analytically calculate the envelope surface in five-axis CNC machining. The cutter surface is represented as the envelope surface of one-parameter spheres. Subsequently, by introducing another parameter as the cutter motion parameter, the envelope surface is obtained as two-parameter families of spheres [72, 73]. Similar theory is applied to calculate the boundary of the screw-sweep of canal surface [74].

Compared to the other methods, the theory of two-parameter families of spheres provides a simpler calculation. However, the computation process is still not straightforward since the cutter surface has to be represented as the envelope surface of one-parameter spheres prior to further calculation. Moreover, as aforementioned, the computation of the curvature of the envelope surface will be more complicated. To address these two problems, the geometric envelope approach is introduced in this thesis. The most elegant

feature of this geometric envelope approach is that the generated surface can be obtained as a closed-form vector representation with parameters h and ϕ, and then curvature analysis can be directly and efficiently implemented with differential geometry equations. The details are stated in Section 2.

1.3 Research problems and objectives

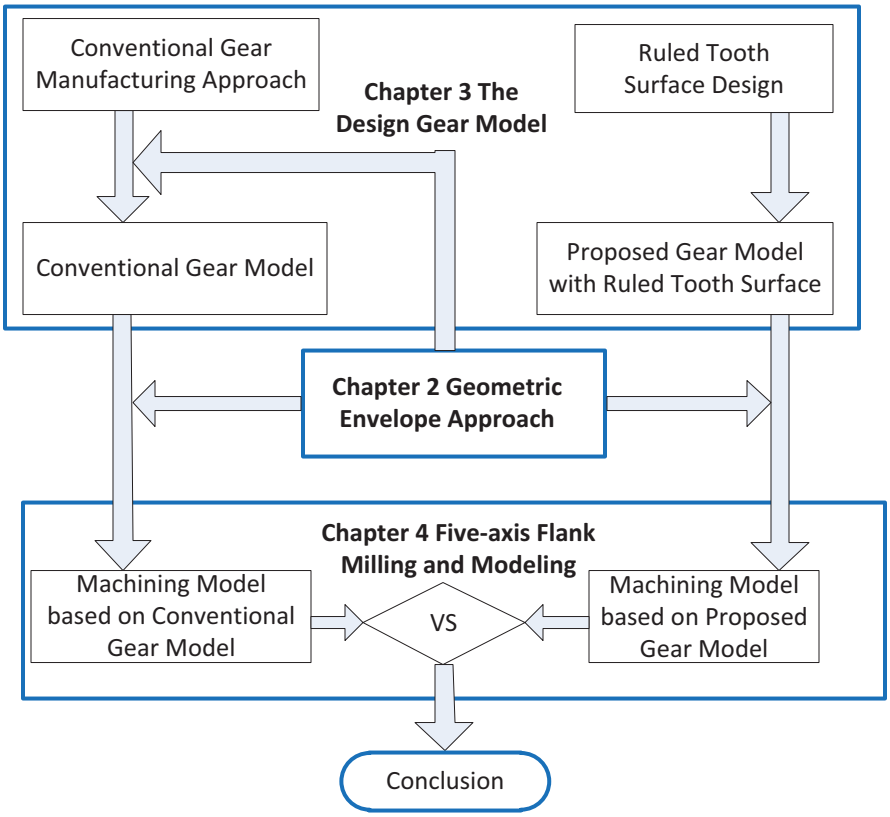

Figure 1.3: Thesis organization.

As stated in the literature review, there are three major problems summarized as follows.

- The calculation of the envelope surface is complicated and not straightforward

- There is no ruled tooth surface design for spiral bevel gears
- There is no literature about five-axis flank milling spiral bevel gears

To address these problems, this thesis proposes some objectives organized as shown in Fig. 1.3. The details are stated as follows.

- In Chapter 2, a new geometric envelope approach (also referred to as geometric meshing theory in the convention of the filed of gear manufacturing) is proposed to obtain a closed-form vector representation of the envelope surface. Subsequently, curvature analysis can be implemented directly and efficiently with differential geometry equations
- In Chapter 3, a ruled tooth surface is proposed to design the tooth surface of spiral bevel gear.
- In Chapter 4, the tool path planning is implemented for five-axis flank milling. Furthermore, the closed-form representation of the simulate machined tooth surface is obtained by using the envelope geometric approach.
- A conclusion is conducted in Chapter 5.

Chapter 2

A new geometric envelope approach

2.1 Envelope surface

2.1.1 An introduce of envelope surface

Envelope surface is mentioned as the boundary surface of the swept volume formed by a object moving in a space. The surface of the object and envelope surface are also called as generating surface and generated surface, respectively. The whole process is called as generating process. Envelope surface has been widely used to simulate the machined surface in many fields of current manufacturing industry. While a product is machining, the machined surface is obtained by removing a certain amount of material from the stock. Subsequently, the machined surface can be calculated as part of the envelope surface of the cutter moving along the given tool path. The details about the envelope surface are introduced as follows.

Assume a generating process is related to a generating surface continuously moving in the three dimensional Euclidean space $\mathbb{E}^3$. With the generating

process, a family of surfaces is formed with respect to all configurations of the generating surface at every moment. Taking an example of Fig. 2.1, the generating surface is a conical surface $\mathbf{r}(h, \theta)$, in which h is the parameter of generatrix and θ is the parameter of rotation. The conical surface undergoes a general motion from the initial configuration to a new configuration corresponding to a moment of the generating process. Assume the parameter of motion is ϕ, then the family of the conical surfaces can be represented as $\mathbf{r}(h, \theta, \phi)$ in $\mathbb{E}^3$ with respect to a chosen fixed point $\mathrm{o}^{(f)}$. At a given instance ϕ^*, the configuration of the generating surfaces can be described as $\mathbf{r}(h, \theta, \phi^*)$.

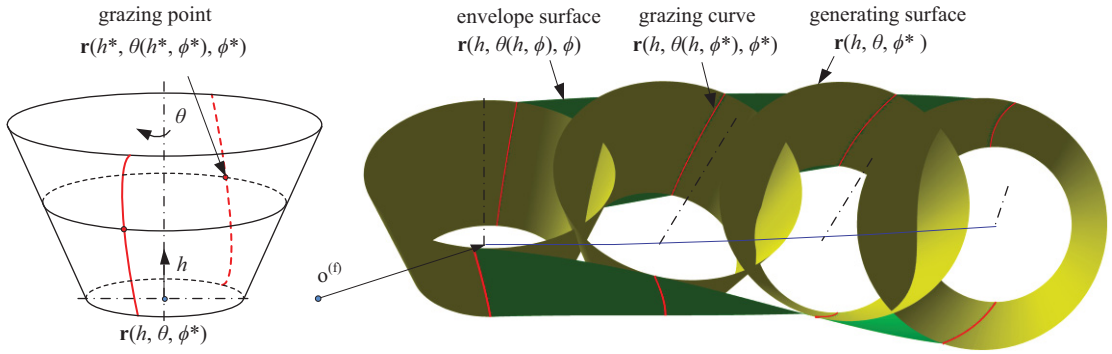

Figure 2.1: The envelope surface of the family of the generating surfaces

During the generating process, the generated surface and the generating surface stay in line contact at every moment. Line contact means that the generating surface tangent at the generated surface along the line. This line is called grazing curve (also referred to as contact line, characteristic curve, critical curve, swept profile, silhouette curve, generating curve, imprint curve, etc). For a given instance ϕ^*, the grazing curve can be represented by eliminating either h or θ. Taking the example of eliminating parameter θ, the grazing curve can be obtained as $\mathbf{r}(h, \theta(h, \phi^*), \phi^*)$. By sampling parameter

ϕ with different values, a series of grazing curves can be obtained, and the generated surface is formed by connecting these grazing curves. In order to obtain a grazing curve, grazing points, which are the points on this grazing curve, should be calculated first. For a specified grazing curve corresponding to ϕ^*, when the parameter h is given as a specified value h^*, the grazing point which is corresponding to ϕ^* and h^* can be represented as $\mathbf{r}(h^*, \theta(h^*, \phi^*), \phi^*)$. By sampling h with different values, the grazing curve is generated by connecting all the grazing points. Hence, the calculation of the grazing point is the key step to obtain the generated surface.

In order to calculate the grazing point, a necessary condition is derived according to the tangent condition between the generating surface and generated surface. The necessary condition is that the unit normal $\mathbf{n}(h, \theta(h, \phi), \phi)$ of the generating surface at the grazing point is orthogonal to the velocity $\mathbf{v}(h, \theta(h, \phi), \phi)$ of the generating surface at the grazing point [2,3,42,43]. This necessary condition is represented as

$$\mathbf{n}(h, \theta(h, \phi), \phi) \cdot \mathbf{v}(h, \theta(h, \phi), \phi) = 0 \tag{2.1}$$

Eq.(2.1) is called equation of meshing in the literature of gear manufacturing, and it is refereed to as envelope theory in the literature of CNC milling. In Eq.(2.1), θ is obtained with given h and ϕ. However, it is not easy to solve Eq.(2.1), especially for the gear generating process, or the five-axis CNC milling, which are involved with different coordinate systems and supplemental motions. In order to make this issue clear, a typical process to calculate the envelope surface used in previous research is illustrated in Section 2.1.2.

2.1.2 The calculation of the envelope surface

Generally, the typical procedure of the currently prevalent way to calculate the envelope surface includes the following steps I $\sim$ IV.

Step I is the definition of the initial configuration of the generating surface. The expression of the position vector of the generating surface $\mathbf{r}(h,\theta)$ at the initial instance $\phi = 0$ can be established first, then the unit normal $\mathbf{n}(h,\theta)$ of generating surface at $\phi = 0$ can be represented as

$$\mathbf{n}(h,\theta) = \frac{\mathbf{r}_h \times \mathbf{r}_\theta}{\mid \mathbf{r}_h \times \mathbf{r}_\theta \mid} \tag{2.2}$$

where

$$\mathbf{r}_h = \frac{\partial \mathbf{r}(h,\theta)}{\partial h}, \mathbf{r}_\theta = \frac{\partial \mathbf{r}(h,\theta)}{\partial \theta}$$

Step II is the calculation of the instantaneous configuration of the generating surface. For a given instance ϕ, the position vector of the generating surface at the currently instantaneous configuration is $\mathbf{r}(h,\theta,\phi)$. Assume there is an instantaneous operator $\mathbf{M}(\phi)$, which will transfer the generating surface from the initial configuration $\mathbf{r}(h,\theta)$ to the instantaneous configuration $\mathbf{r}(h,\theta,\phi)$. Then $\mathbf{r}(h,\theta,\phi)$ can be obtained as

$$\mathbf{r}(h,\theta,\phi) = \mathbf{M}(\phi) \cdot \mathbf{r}(h,\theta) \tag{2.3}$$

Also the instantaneous unit normal $\mathbf{n}(h,\theta,\phi)$ of the generating surface can be obtained as

$$\mathbf{n}(h,\theta,\phi) = \mathbf{M}(\phi) \cdot \mathbf{n}(h,\theta) \tag{2.4}$$

The instantaneous operator $\mathbf{M}(\phi)$ can be obtained in different ways. The classic Litvin's approach [2, 3] calculates $\mathbf{M}(\phi)$ as a homogeneous transformation matrix (HTM) based on kinematic chain. $\mathbf{M}(\phi)$ is also represented with the rotation vector [17] and the rotation tensor [19] in the invariant approach.

Step III is the calculation of the velocity of the generating surface. The methods used to calculate the velocity in previous research can be included in two ways. The first one is the derivative approach, which is based on the derivative of the instantaneous configuration $\mathbf{r}(h, \theta, \phi)$ with respect to ϕ. According to Eq. (2.3), the velocity can be obtained as

$$\mathbf{v}(h, \theta, \phi) = \frac{d\mathbf{M}(\phi)}{d\phi} \cdot \mathbf{r}(h, \theta) \tag{2.5}$$

The second way is the instantaneous angular velocity approach. When the instantaneous angular velocity and the velocity of a point on the instantaneous axis are obtained as $\boldsymbol{\omega}(\phi)$ and $\mathbf{v}_{\mathrm{o}}(\phi)$, respectively, the velocity of the generating surface can be calculated as

$$\begin{aligned} \mathbf{v}(h, \theta, \phi) &= \mathbf{v}_{\mathrm{o}}(\phi) + \boldsymbol{\omega}(\phi) \times \mathbf{r}(h, \theta, \phi) \\ &= \mathbf{v}_{\mathrm{o}}(\phi) + \boldsymbol{\omega}(\phi) \times (\mathbf{M}(\phi) \cdot \mathbf{r}(h, \theta)) \end{aligned} \tag{2.6}$$

Step IV is to solve the equation of meshing by submitting the unit normal and the velocity. Submitting Eqs. (2.4) and (2.5) into Eq. (2.1), the equation of meshing can be written as

$$[\mathbf{M}(\phi) \cdot \mathbf{n}(h, \theta)] \cdot \left[\frac{d\mathbf{M}(\phi)}{d\phi} \cdot \mathbf{r}(h,\ \theta) \right] = 0 \tag{2.7}$$

The equation of meshing can also be solved by submitting Eqs. (2.4) and (2.6) into Eq. (2.1)

$$[\mathbf{M}(\phi) \cdot \mathbf{n}(h, \theta)] \cdot [\mathbf{v}_{\mathrm{o}}(\phi) + \boldsymbol{\omega}(\phi) \times (\mathbf{M}(\phi) \cdot \mathbf{r}(h, \theta))] = 0 \tag{2.8}$$

On one hand, either Eq.(2.7) or Eq.(2.8) involves operator $\mathbf{M}(\phi)$ twice, and this makes the equation of meshing complicated, especially for the gear generating process with the supplemental motion such as modified roll, helical motion and tilt motion. On the other hand, the calculation process is not straightforward. For calculating a single contact point, the calculation process is to obtain θ with specified ϕ^* and h^* based on the equation of meshing. First, these two items in the equation of meshing, $\mathbf{n}$ and $\mathbf{v}$, are expressed as the functions of θ in the initial configuration and subsequently transformed into the instantaneous configuration. Then θ is obtained as θ^* by solving the equation of meshing, and the contact point is obtained as $\mathbf{r}(h^*, \theta^*)$ in the initial configuration. Furthermore, the final representation $\mathbf{r}(h^*, \theta^*, \phi^*)$ is obtained by transforming $\mathbf{r}(h^*, \theta^*)$ into the instantaneous configuration.

The generated surface is obtained by combining the equation of meshing, either Eq. (2.7) or Eq. (2.8) with the expression of the instantaneous configuration of the generating surface, Eq. (2.3). Since it is complicated to find the closed-form solution for the equation of meshing, it is usually represented as an implicit function

$$f(h, \theta, \phi) = 0 \tag{2.9}$$

Combining Eqs. (2.3) and (2.9), the implicit form of the generated surface

can be expressed as

$$\begin{cases} \mathbf{r}(h,\theta,\phi) = \mathbf{M}(\phi)\cdot\mathbf{r}(h,\theta) \\ f(h,\theta,\phi) = 0 \end{cases} \tag{2.10}$$

It is difficult to directly use differential geometry equations to do curvature analysis based on Eq. (2.10) because the derivatives of the equation of meshing is involved. Some alternative approaches are used to do curvature analysis, such as theory of gearing [3], invariant approach [25]. Both of these two approaches calculate the curvature of the generated surface based on two similar systems of three linear equations [3, 25, Eq. (13.1.27), p. 264 and Eq. (90), p. 393, respectively].

The above processes of the calculation of the generated surface and curvature analysis can be simplified. First, The expressions of $\mathbf{n}$ and $\mathbf{v}$ are not necessary to relate with θ, and the contact point can be calculated directly in the instantaneous configuration. Moreover, the generated surface can be expressed as a closed-form representation. A better approach is proposed recently by combining with the envelope theory and the theory of two-parameter families of spheres (or referred to as sphere congruence) [72–74]. This approach analytically calculate the envelope surface in five-axis CNC machining. The cutter surface is represented as the envelope surface of one-parameter spheres. Subsequently, by introducing another parameter as the cutter motion parameter, the envelope surface is obtained as two-parameter families of spheres [72,73]. Similar theory is applied to calculate the boundary of the screw-sweep of canal surface [74].

Compared to the other methods, the theory of two-parameter families of spheres provides a simpler calculation. However, the computation process is still not straightforward since the cutter surface has to be represented as the envelope surface of one-parameter spheres prior to further calculation. Moreover, the curvature analysis is still very challenging. To address these two problems, the geometric envelope approach is introduced to straightforwardly and efficiently to calculate the envelope surface of the specific circular surface, which is a general case of surface including the surface of revolution, canal surface and tube surface. Subsequently, curvature analysis can be implemented directly and efficiently with differential geometry equations. The details are stated in Section 2.2.

2.2 A geometric envelope approach for the specific circular surface

The geometric envelope approach is introduced to calculate the envelope surface of a special group of generating surface, which is called the specific circular surface in this thesis. First, the specific circular surface and its geometric characteristic are introduced. Subsequently, a geometric equation is derived according to the geometric characteristic. Moreover, a simplified equation of the envelope theory is obtained for the specific circular surface. Consequently, the geometric envelope approach is obtained by combining both equations.

2.2.1 Specific circular surface and the geometric equation

As shown in Fig. 2.2, a circular surface is a one-parameter family of circles with its center following the curve $\mathbf{o}(h)$ in Euclidean space $\mathbb{E}^3$ [75, 76]. Each circle is called as generating circle. A circular surface can be defined as

$$\mathbf{r}(h,\theta) = \mathbf{o}(h) + R(h) \cdot (\mathbf{N}(h) \cdot \cos\theta + \mathbf{B}(h) \cdot \sin\theta) \tag{2.11}$$

where

h is the parameter to define the trajectory curve of the circle center $\mathbf{o}(h)$;

$R(h)$ is the radius of the generating circle;

θ is the parameter to define the generating circle;

$\mathbf{N}$ and $\mathbf{B}$ are two unit orthogonal vectors lying on the plane of the generating circle whose unit normal is $\mathbf{T}$ ($\mathbf{T}$ is different with $\mathbf{t}$, which is the unit tangent vector of $\mathbf{o}(h)$). $\{\mathbf{T}, \mathbf{N}, \mathbf{B}\}$ is the Frenet–Serret frame.

Specially, a group of circular surfaces are introduced with the following property: given a generating circle, the normals of the circular surface at all points of this generating circle intersect at a point $\mathbf{q}$, which lies on the line passing through $\mathbf{o}$ and paralleling with $\mathbf{T}$. Assume that $\mathbf{p}$ is a point on this generating circle. ρ is the distance between $\mathbf{q}$ and $\mathbf{p}$. We have

$$\rho(h) = R(h) \cdot \csc\alpha(h) \tag{2.12}$$

where α is the angle formed by $\mathbf{T}$ and $\mathbf{n}$, which is the unit normal vector of the circular surface at $\mathbf{p}$. For clarity, ρ, α, $\mathbf{q}$ and $\mathbf{T}$ are named in this

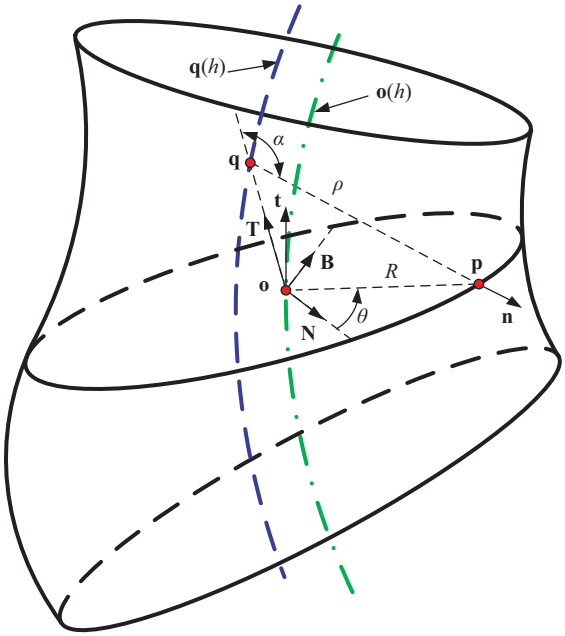

Figure 2.2: The specific circular surface.

thesis as effective radius, effective angle, effective center curve and unit circle normal, respectively.

The circular surfaces with above property is named as specific circular surface in this thesis. It includes surface of revolution [77], canal surface [72–74] and tube surface [74]. According to its property, the specific circular surface also can be represented as

$$\mathbf{r}(h,\theta) = \mathbf{q}(h) + \rho(h) \cdot \mathbf{n}(h,\theta). \tag{2.13}$$

Assume that $\mathbf{n}$ always directs away from $\mathbf{q}$ (also away from the object body of the circular surface). This assumption is applied throughout this thesis.

For a specific circular surface, we have

$$\mathbf{n}(h,\theta)\cdot\mathbf{T}(h)=\cos\alpha(h). \tag{2.14}$$

Eq. (2.14) is useful to derive the envelope surface as a result of closed-form representation. Since Eq. (2.14) is a geometric characteristic of the specific circular surface, it is regarded as the geometric equation.

2.2.2 Geometric envelope approach

When the specific circular surface moves continuously under a general motion, a family of the specific circular surface is obtained. Assuming that the motion parameter is ϕ, the family of the specific circular surface can be expressed according to Eq. (2.13) as

$$\mathbf{r}(h,\theta,\phi)=\mathbf{q}(h,\phi)+\rho(h)\cdot\mathbf{n}(h,\theta,\phi). \tag{2.15}$$

The velocity of the specific circular surface can be calculated by differentiating Eq. (2.15) with respect to ϕ. We have

$$\mathbf{v}(h,\theta,\phi)=\frac{\partial\mathbf{q}(h,\phi)}{\partial\phi}+\rho(h)\cdot\frac{\partial\mathbf{n}(h,\theta,\phi)}{\partial\phi}. \tag{2.16}$$

According to the envelope theory, the specific circular surface and its envelope surface are tangent with each other along a curve at every instant during the moving process [43]. This curve is regarded as the grazing curve. The point on the grazing curve is the grazing point. To calculate the grazing point, the tangent condition is used as a necessary condition which is written

as an equation of the envelope theory [43]

$$\mathbf{n} \cdot \mathbf{v} = 0. \tag{2.17}$$

By Submitting Eq. (2.16) into Eq. (2.17), we have a simplified equation of the envelope theory as

$$\begin{aligned} \mathbf{n} \cdot \mathbf{v} &= \mathbf{n}(h, \theta, \phi) \cdot \left(\frac{\partial \mathbf{q}(h, \phi)}{\partial \phi} + \rho(h) \cdot \frac{\partial \mathbf{n}(h, \theta, \phi)}{\partial \phi} \right) \\ &= \mathbf{n}(h, \theta, \phi) \cdot \frac{\partial \mathbf{q}(h, \phi)}{\partial \phi} = \mathbf{n}(h, \theta, \phi) \cdot \mathbf{v}_{\mathrm{q}}(h, \phi) = 0. \end{aligned} \tag{2.18}$$

Eq. (2.18) means that if $\mathbf{p}$ is a grazing point, the normal of the specific circular surface at $\mathbf{p}$ is orthogonal to $\mathbf{v}_{\mathrm{q}}$, which is the velocity of the specific circular surface at $\mathbf{q}$. This is a special characteristic when the envelope theory is applied to the specific circular surface. Another important feature of Eq. (2.18) is that $\mathbf{v}_{\mathrm{q}}$ is not related with the parameter θ. It is very helpful to represent the grazing point as a closed-form expression.

Considering the geometric equation, Eq.(2.14), under the general motion, we have

$$\mathbf{n}(h, \theta, \phi) \cdot \mathbf{T}(h, \phi) = \cos \alpha(h). \tag{2.19}$$

Combining Eqs.(2.18) with (2.19), the geometric envelope approach is obtained as a system of two independent equations. With the given values for h and ϕ, $\mathbf{v}_{\mathrm{q}}$ and $\mathbf{T}$ become two knowns based on the corresponding motion description. Since the unit normal $\mathbf{n}$ can be expressed with two arbitrary independent parameters in any chosen coordinate system, it can be solved with two independent equations. Therefore, the unit normal $\mathbf{n}$ of the graz-

ing point can be directly calculated with the geometric envelope approach. Moreover, both $\mathbf{v}_{\mathrm{q}}$ and $\mathbf{T}$ are independent of θ. Hence $\mathbf{n}$ is also independent of θ. By eliminating θ, the geometric envelope approach can be written as

$$\begin{cases} \mathbf{n}(h,\phi)\cdot\mathbf{v}_{\mathrm{q}}(h,\phi)=0 \\ \mathbf{n}(h,\phi)\cdot\mathbf{T}(h,\phi)=\cos\alpha(h). \end{cases} \tag{2.20}$$

2.2.3 The closed-form solution of the geometric envelope approach

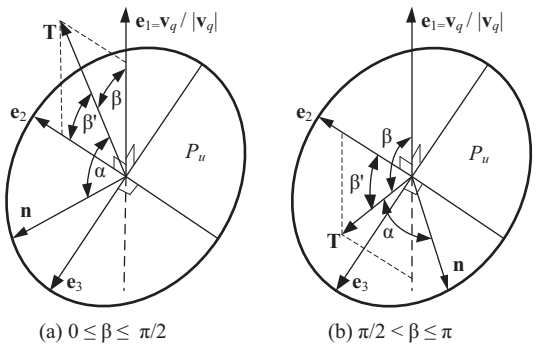

Figure 2.3: The calculation of the unit normal $\mathbf{n}$.

According to the invariant envelope theory, the envelope surface can be calculated. A vector calculation is derived to obtain the closed-form result. The vector calculation is conducted by illustrating the invariant envelope theory with two geometric conditions. As shown in Fig. 2.3, assume that P_u represents the plane orthogonal to $\mathbf{e}_1$, which is the unit vector of $\mathbf{v}_q$. According to the first equation in Eq. (2.20), $\mathbf{n}$ should lie on P_u. Moreover, $\mathbf{n}$ should form an angle α with $\mathbf{T}$ according to the second equation in Eq. (2.20). $\mathbf{n}$ can be obtained according to these two geometric conditions.

As shown in Fig. 2.3, assume that $\mathbf{e}_2$ is the unit vector of the projection of $\mathbf{T}$ onto P_u. By introducing $\mathbf{e}_3=\mathbf{e}_1\times\mathbf{e}_2$, $\{\mathbf{e}_1,\mathbf{e}_2,\mathbf{e}_3\}$ are three basis vectors of

a right-handed fame. Assume that the angle between $\mathbf{e}_1$ and $\mathbf{T}$ is β, $\beta \in [0, \pi]$, then we have

$$\sin\beta = \mid \mathbf{T} \times \mathbf{e}_1 \mid, \cos\beta = \mathbf{T} \cdot \mathbf{e}_1 \tag{2.21}$$

$$\mathbf{T} = \cos\beta \cdot \mathbf{e}_1 + \sin\beta \cdot \mathbf{e}_2. \tag{2.22}$$

By substituting that Eq. (2.22) into the second equation of Eq. (2.20), we have

$$\mathbf{n} \cdot (\sin\beta \cdot \mathbf{e}_2 + \cos\beta \cdot \mathbf{e}_1) = \sin\beta \cdot (\mathbf{n} \cdot \mathbf{e}_2) = \cos\alpha. \tag{2.23}$$

Usually, $\beta \neq 0$ or π. When $\beta = 0$ or π, theres is no solution for $\mathbf{n}$ unless $\alpha = \pi/2$ and $\mathbf{e}_1 = \pm\mathbf{T}$ (the case $\alpha = \pi/2$ will be discussed later as a particular case of the invariant envelope theory). If $\beta \neq 0$ or π, Eq. (2.23) can be derived as

$$\mathbf{n} \cdot \mathbf{e}_2 = \frac{\cos\alpha}{\sin\beta}. \tag{2.24}$$

With Eq. (2.24), we know that it should be $\mid \cos\alpha / \sin\beta \mid \leq 1$, or $\mathbf{n}$ does not exist. This condition can be geometrically explained according to Fig. 2.3. Assume that the angle between $\mathbf{T}$ and $\mathbf{e}_2$ is β'. $\beta' = \pi/2 - \beta$ when $\beta \subseteq [0, \pi/2]$, and $\beta' = \beta - \pi/2$ when $\beta \subseteq (\pi/2, \pi]$. Since $\mathbf{e}_2$ is the unit vector of the projection of $\mathbf{T}$ onto P_u, we have $0 \leq \beta' \leq \alpha \leq \pi/2$. Hence, if the solution of $\mathbf{n}$ exists, $\mid \cos\alpha / \sin\beta \mid \leq 1$.

With Eq. (2.24) and considering that $\mathbf{n}$, $\mathbf{e}_2$ and $\mathbf{e}_3$ all lie on P_u, we have

$$\begin{aligned} \mathbf{n} &= (\mathbf{n} \cdot \mathbf{e}_2) \cdot \mathbf{e}_2 + (\mathbf{n} \cdot \mathbf{e}_3) \cdot \mathbf{e}_3 \\ &= \frac{\cos\alpha}{\sin\beta} \cdot \mathbf{e}_2 \pm \sqrt{1 - \left(\frac{\cos\alpha}{\sin\beta}\right)^2} \cdot \mathbf{e}_3. \end{aligned} \tag{2.25}$$

Referring to Eq. (2.22), we have

$$\mathbf{e}_2 = \frac{1}{\sin\beta} \cdot \mathbf{T} - \cot\beta \cdot \mathbf{e}_1 \tag{2.26}$$

$$\mathbf{e}_3 = \mathbf{e}_1 \times \mathbf{e}_2 = \frac{1}{\sin\beta} \cdot (\mathbf{e}_1 \times \mathbf{T}) \,. \tag{2.27}$$

By substituting Eqs. (2.26)and (2.27) into Eq. (2.25), we have

$$\begin{aligned} \mathbf{n} &= \frac{\cos\alpha}{\sin^2\beta} \cdot \mathbf{T} - \frac{\cos\alpha \cdot \cos\beta}{\sin^2\beta} \cdot \mathbf{e}_1 \pm \frac{\sqrt{\sin^2\beta - \cos^2\alpha}}{\sin^2\beta} \cdot (\mathbf{T} \times \mathbf{e}_1) \\ &= \frac{\cos\alpha}{(\mathbf{T} \times \mathbf{e}_1)^2} \cdot \mathbf{T} - \frac{(\mathbf{T} \cdot \mathbf{e}_1) \cdot \cos\alpha}{(\mathbf{T} \times \mathbf{e}_1)^2} \cdot \mathbf{e}_1 \pm \frac{\sqrt{(\mathbf{T} \times \mathbf{e}_1)^2 - \cos^2\alpha}}{(\mathbf{T} \times \mathbf{e}_1)^2} \cdot (\mathbf{T} \times \mathbf{e}_1) \,. \end{aligned} \tag{2.28}$$

Since $\mathbf{e}_1$ is the unit vector of $\mathbf{v}_q$, then we have

$$\mathbf{e}_1 = \frac{\mathbf{v}_q}{|\ \mathbf{v}_q\ |}, \mathbf{T} \times \mathbf{e}_1 = \frac{\mathbf{T} \times \mathbf{v}_q}{|\ \mathbf{v}_q\ |}, \mathbf{T} \cdot \mathbf{e}_1 = \frac{\mathbf{T} \cdot \mathbf{v}_q}{|\ \mathbf{v}_q\ |}. \tag{2.29}$$

By substituting Eq. (2.29) into Eq. (2.28), Eq. (2.28) can be replaced as

$$\mathbf{n} = \frac{\cos\alpha \cdot \mathbf{v}_q^2}{(\mathbf{T} \times \mathbf{v}_q)^2} \cdot \mathbf{T} - \frac{(\mathbf{T} \cdot \mathbf{v}_q) \cdot \cos\alpha}{(\mathbf{T} \times \mathbf{v}_q)^2} \cdot \mathbf{v}_q \pm \frac{\sqrt{(\mathbf{T} \times \mathbf{v}_q)^2 - \cos^2\alpha \cdot \mathbf{v}_q^2}}{(\mathbf{T} \times \mathbf{v}_q)^2} \cdot (\mathbf{T} \times \mathbf{v}_q) \,. \tag{2.30}$$

Eqs. (2.28) and (2.30) are two closed-form expressions for the unit normal $\mathbf{n}$ of the envelope surface at the grazing point. Furthermore, the closed-form expression of the envelope surface can be obtained according to Eq. (2.15) as

$$\mathbf{s}(h, \phi) = \mathbf{q}(h, \phi) + \rho(h) \cdot \mathbf{n}(h, \phi) \tag{2.31}$$

where $\mathbf{n}(h, \phi)$ has been calculated in Eq. (2.28) or Eq. (2.30).

There are several significant features for this envelope surface expression.

- It is a closed-form expression with respect to two parameters, h and ϕ. According to [77], it is more efficient than the closed-form methods mentioned in [63–71, 73, 74], where the parameter θ is eliminated by solving the trigonometric function
- The expression is invariant to coordinate system because it is written in vector form. Subsequently, the result can be calculated by choosing any convenient coordinate system
- To calculate the grazing point, the velocity of $\mathbf{q}$ is calculated rather than $\mathbf{p}$. This is very useful to simplify the computation in the later calculation of the accurate envelope surface according to the accurate cutter motion in practical machining
- The envelope surface is related to four terms: $\rho(h)$, $\alpha(h)$, $\mathbf{q}(h,\phi)$ and $\mathbf{T}(h,\phi)$ since $\mathbf{v}_{\mathrm{q}}(h,\phi)$ is the derivative of $\mathbf{q}(h,\phi)$ with to ϕ. $\rho(h)$ and $\alpha(h)$ are effective radius and effective angle, respectively. They are only related to the shape of the specific circular surface. $\mathbf{q}(h,\phi)$ and $\mathbf{T}(h,\phi)$ are not only determined by the effective center curve and unit circle normal, respectively, but also the motion of the specific circular surface

Particular case for surface of revolution

while the generating surface is a surface of revolution, it is can be treat as the special case of the specific circular surface. As shown in Fig. 2.4, the generatrix is given as a regular curve $\mathbf{c}(h)$ and h is the parameter. The generating surface is the surface of revolution by rotating $\mathbf{c}(h)$ along the

cutter axis $\mathbf{l}$, and θ is the parameter of rotation. o is the intersection point of $\mathbf{l}$ and the bottom plane which is corresponded to $h = 0$. R_c is the distance from the cutting edge point to the cutter axis. Z_c is the distance from the cutting edge point to the bottom plane. $\mathbf{n}$ is the unit normal of the generating surface at a point p, and assume $\mathbf{n}$ is positive when it is far away from $\mathbf{l}$. p_h is the intersection point of $\mathbf{n}$ and $\mathbf{l}$, and α is the angle from $\mathbf{n}$ to $\mathbf{l}$. ρ is the distance between p and p_h, and h is the distance from o to p_h.

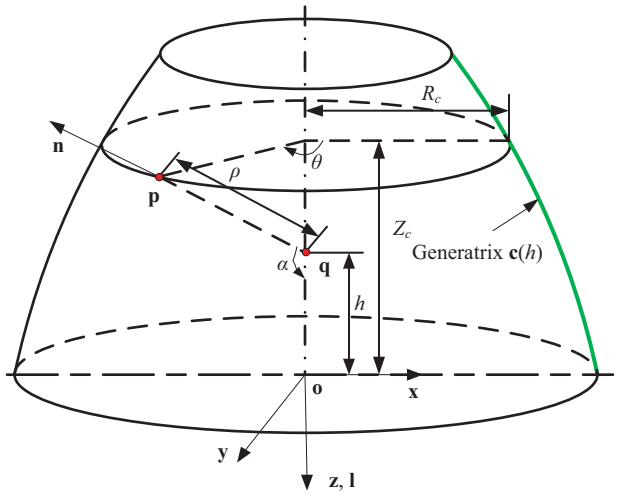

Figure 2.4: A generic model to represent the surface of revolution of the generating surface

The surface of revolution can be represented with a vector form or a scalar form. The vector form is invariant with coordinate systems but the scalar form is related with. Compared to the scalar form, the vector form is simple and compact to carry out theoretical development. After theoretical development, the practical computation can be implemented with the scalar form by choosing a convenient coordinate system. The surface of revolution can

be expressed with the vector form as

$$\mathbf{r}(h,\theta) = \mathbf{o} + h \cdot \mathbf{l} + \rho(h) \cdot \mathbf{n}(h,\theta) \tag{2.32}$$

where

$$\rho(h) = R_c(h) \cdot \csc\alpha(h)$$

For the surface of revolution as shown in Fig. 2.4, the unit circle normal is coincident with $\mathbf{l}$, which is the unit vector of the cutter axis, and the effective center curve is coincident with the cutter axis. We have

$$\mathbf{T}(h) = \mathbf{l}, \mathbf{q}(h) = \mathbf{o}_\mathrm{c} + h \cdot \mathbf{l}. \tag{2.33}$$

By substituting Eq. (2.33) into Eqs. (2.30) and (2.31), the envelope surface of the surface of revolution is written as

$$\mathbf{r}(h,\phi) = \mathbf{o}_\mathrm{c}(\phi) + h \cdot \mathbf{l}(\phi) + \rho(h) \cdot \mathbf{n}(h,\phi) \tag{2.34}$$

where

$$\mathbf{n}(h,\phi) = \frac{\cos\alpha \cdot \mathbf{v}_\mathrm{q}^2}{(\mathbf{l}\times\mathbf{v}_\mathrm{q})^2}\cdot\mathbf{l} - \frac{(\mathbf{l}\cdot\mathbf{v}_\mathrm{q})\cdot\cos\alpha}{(\mathbf{l}\times\mathbf{v}_\mathrm{q})^2}\cdot\mathbf{v}_\mathrm{q} \pm \frac{\sqrt{(\mathbf{l}\times\mathbf{v}_\mathrm{q})^2 - \cos^2\alpha\cdot\mathbf{v}_\mathrm{q}^2}}{(\mathbf{l}\times\mathbf{v}_\mathrm{q})^2}\cdot(\mathbf{l}\times\mathbf{v}_\mathrm{q})\,. \tag{2.35}$$

Particular case for cylindrical surface

For cylindrical surface, we have $\alpha(h) = \pi/2$, and the effective center curve $\mathbf{q}(h)$ is coincident with the center curve $\mathbf{o}(h)$. Eq. (2.20) can be derived as

$$\begin{cases} \mathbf{n}(h,\phi) \perp \mathbf{v}_{\mathrm{q}}(h,\phi) \\ \mathbf{n}(h,\phi) \perp \mathbf{T}(h,\phi). \end{cases} \tag{2.36}$$

Then we have

$$\mathbf{n}(h,\phi) = \pm \frac{\mathbf{T}(h,\phi) \times \mathbf{v}_{\mathrm{q}}(h,\phi)}{\mid \mathbf{T}(h,\phi) \times \mathbf{v}_{\mathrm{q}}(h,\phi) \mid}. \tag{2.37}$$

The result of Eq. (2.37) can also be obtained by substituting $\alpha(h) = \pi/2$ into Eq. (2.30). Subsequently, the envelope surface of the cylindrical surface can be obtained by substituting Eq. (2.37) into Eq. (2.31). We have

$$\mathbf{r}(h,\phi) = \mathbf{q}(h,\phi) \pm \rho(h) \cdot \frac{\mathbf{T}(h,\phi) \times \mathbf{v}_{\mathrm{q}}(h,\phi)}{\mid \mathbf{T}(h,\phi) \times \mathbf{v}_{\mathrm{q}}(h,\phi) \mid}. \tag{2.38}$$

2.3 Curvature analysis of the envelope surface

With the closed-form representation of the envelope surface, its curvature analysis can be directly implemented with differential geometry equations. In this section, the basic derivatives of both envelope surface and its normal are calculated first. Subsequently, the curvature analysis is implemented with two methods based on differential geometry equations.

2.3.1 Basic derivatives

The derivatives of the unit normal of the envelope surface can be calculated with Eqs. (2.30) and (2.31) can be derived as

$$\mathbf{n}\cdot(\mathbf{T}\times\mathbf{v}_q)^2=\cos\alpha\cdot\mathbf{v}_q^2\cdot\mathbf{T}-(\mathbf{T}\cdot\mathbf{v}_q)\cdot\cos\alpha\cdot\mathbf{v}_q\pm\sqrt{(\mathbf{T}\times\mathbf{v}_q)^2-\cos^2\alpha\cdot\mathbf{v}_q^2}\cdot(\mathbf{T}\times\mathbf{v}_q) \tag{2.39}$$

Assume

$$f_1=(\mathbf{T}\times\mathbf{v}_q)^2\,,f_2=\cos\alpha\cdot\mathbf{v}_q^2,f_3=-\cos\alpha\cdot(\mathbf{T}\cdot\mathbf{v}_q)\,,f_4=\pm\sqrt{(\mathbf{T}\times\mathbf{v}_q)^2-\cos^2\alpha\cdot\mathbf{v}_q^2} \tag{2.40}$$

Submitting Eq. (2.40) into Eq. (2.39), Eq. (2.39) can be derived as

$$f_1\cdot\mathbf{n}=f_2\cdot\mathbf{T}+f_3\cdot\mathbf{v}_q+f_4\cdot(\mathbf{T}\times\mathbf{v}_q) \tag{2.41}$$

Taking the derivatives of both sides of Eq. (2.41) with respect to h, we have

$$\frac{\partial f_1}{\partial h}\cdot\mathbf{n}+f_1\cdot\frac{\partial\mathbf{n}}{\partial h}=\frac{\partial f_2}{\partial h}\cdot\mathbf{T}+\frac{\partial f_3}{\partial h}\cdot\mathbf{v}_q+f_3\cdot\frac{\partial\mathbf{v}_q}{\partial h}+\frac{\partial f_4}{\partial h}\cdot(\mathbf{T}\times\mathbf{v}_q)+f_4\cdot\frac{\partial(\mathbf{T}\times\mathbf{v}_q)}{\partial h} \tag{2.42}$$

Then the derivative of $\mathbf{n}$ with respect to h is given as

$$\begin{aligned}\mathbf{n}_h=\frac{\partial\mathbf{n}}{\partial h}=&\frac{1}{f_1}\cdot\left[-\frac{\partial f_1}{\partial h}\cdot\mathbf{n}+\frac{\partial f_2}{\partial h}\cdot\mathbf{T}+\frac{\partial f_3}{\partial h}\cdot\mathbf{v}_q\right.\\&\left.+f_3\cdot\frac{\partial\mathbf{v}_q}{\partial h}+\frac{\partial f_4}{\partial h}\cdot(\mathbf{T}\times\mathbf{v}_q)+f_4\cdot\frac{\partial(\mathbf{T}\times\mathbf{v}_q)}{\partial h}\right]\end{aligned} \tag{2.43}$$

where

$$\begin{aligned}
\frac{\partial f_1}{\partial h} &= 2 \cdot (\mathbf{T} \times \mathbf{v}_q) \cdot \frac{\partial (\mathbf{T} \times \mathbf{v}_q)}{\partial h} = 2 \cdot (\mathbf{T} \times \mathbf{v}_q) \cdot \left(\mathbf{T} \times \frac{\partial \mathbf{v}_q}{\partial h} \right) \\
\frac{\partial f_2}{\partial h} &= -\sin\alpha \cdot \frac{d\alpha}{dh} \cdot \mathbf{v}_q^2 + 2 \cdot \cos\alpha \cdot \mathbf{v}_q \cdot \frac{\partial \mathbf{v}_q}{\partial h} \\
\frac{\partial f_3}{\partial h} &= \sin\alpha \cdot \frac{d\alpha}{dh} \cdot (\mathbf{T} \cdot \mathbf{v}_q) - \cos\alpha \cdot \frac{d(\mathbf{T} \cdot \mathbf{v}_q)}{dh} \\
\frac{\partial f_4}{\partial h} &= \frac{1}{2 \cdot f_4} \cdot \left(\frac{\partial f_1}{\partial h} + \sin 2\alpha \cdot \frac{d\alpha}{dh} \cdot \mathbf{v}_q^2 - 2 \cdot \cos^2\alpha \cdot \mathbf{v}_q \cdot \frac{\partial \mathbf{v}_q}{\partial h} \right)
\end{aligned}$$

Similarly, the derivative of $\mathbf{n}$ with respect to ϕ is given as

$$\begin{aligned}
\mathbf{n}_\phi = \frac{\partial \mathbf{n}}{\partial \phi} = & \frac{1}{f_1} \cdot \left[-\frac{\partial f_1}{\partial \phi} \cdot \mathbf{n} + \frac{\partial f_2}{\partial \phi} \cdot \mathbf{T} + f_2 \cdot \frac{d\mathbf{T}}{d\phi} + \frac{\partial f_3}{\partial \phi} \cdot \mathbf{v}_q \right. \\
& \left. + f_3 \cdot \frac{\partial \mathbf{v}_q}{\partial \phi} + \frac{\partial f_4}{\partial \phi} \cdot (\mathbf{T} \times \mathbf{v}_q) + f_4 \cdot \frac{\partial (\mathbf{T} \times \mathbf{v}_q)}{\partial \phi} \right]
\end{aligned} \tag{2.44}$$

where

$$\begin{aligned}
\frac{\partial f_1}{\partial \phi} &= 2 \cdot (\mathbf{T} \times \mathbf{v}_q) \cdot \frac{\partial (\mathbf{T} \times \mathbf{v}_q)}{\partial \phi} = 2 \cdot (\mathbf{T} \times \mathbf{v}_q) \cdot \left(\frac{d\mathbf{T}}{d\phi} \times \mathbf{v}_q + \mathbf{T} \times \frac{\partial \mathbf{v}_q}{\partial \phi} \right) \\
\frac{\partial f_2}{\partial \phi} &= 2 \cdot \cos\alpha \cdot \mathbf{v}_q \cdot \frac{\partial \mathbf{v}_q}{\partial \phi} \\
\frac{\partial f_3}{\partial \phi} &= -\cos\alpha \cdot \frac{d(\mathbf{T} \cdot \mathbf{v}_q)}{d\phi} \\
\frac{\partial f_4}{\partial \phi} &= \frac{1}{2 \cdot f_4} \cdot \left(\frac{\partial f_1}{\partial \phi} - 2 \cdot \cos^2\alpha \cdot \mathbf{v}_q \cdot \frac{\partial \mathbf{v}_q}{\partial \phi} \right)
\end{aligned}$$

With the derivatives of the unit normal, the derivatives of the envelope surface can be calculated according to Eq. (2.34) as

$$\mathbf{r}_h = \frac{\partial \mathbf{r}(h,\phi)}{\partial h} = \mathbf{T}(\phi) + \frac{d\rho(h)}{dh} \cdot \mathbf{n}(h,\phi) + \rho(h) \cdot \mathbf{n}_h \tag{2.45}$$

$$\mathbf{r}_\phi = \frac{\partial \mathbf{r}(h,\phi)}{\partial \phi} = \mathbf{v}_q(h,\phi) + \rho(h) \cdot \mathbf{n}_\phi \tag{2.46}$$

where $\mathbf{n}_h$ and $\mathbf{n}_\phi$ have been calculated in Eqs.(2.43) and (2.44), respectively.

2.3.2 Curvature analysis with differential geometry methods

With well-established differential geometry, the curvature analysis can be carried out in different ways. Two methods are introduced here as the applications of differential geometry to the envelope surface. One is fundamental form method in which the coefficients of the first and second fundamental forms are used. The other one is Rodrigues' Formula method which is based on Rodrigues' Formula.

Fundamental form method

To study the geometric properties of a regular surface around a given point, the curves which lie on the surface and pass through this point are always involved. Assume these curves are expressed as $\mathbf{r}(s)$, where s is the arc length parameter. The tangent vector of $\mathbf{r}(s)$ can be expressed as

$$d\mathbf{r} = \dot{\mathbf{r}} \cdot ds = \mathbf{r}_h \cdot dh + \mathbf{r}_\phi \cdot d\phi \tag{2.47}$$

The normal curvature along $d\mathbf{r}$ is determined by the equation [2, Eq. (7.4.15), p. 177]

$$\kappa_n = \frac{II}{I} = \frac{-d\mathbf{r} \cdot d\mathbf{n}}{d\mathbf{r}^2} = \frac{L \cdot dh^2 + 2 \cdot M \cdot dh \cdot d\phi + N \cdot d\phi^2}{E \cdot dh^2 + 2 \cdot F \cdot dh \cdot d\phi + G \cdot d\phi^2} \tag{2.48}$$

where I, II are first and second fundamental forms, respectively (proposed by the famous mathematician Gauss). E, F and G are the coefficients of the

first fundamental form, and L, M and N are the coefficients of the second fundamental form. These coefficients are obtained as

$$E = \mathbf{r}_h^2, F = \mathbf{r}_h \cdot \mathbf{r}_\phi, G = \mathbf{r}_\phi^2 \tag{2.49}$$

$$L = -\mathbf{r}_h \cdot \mathbf{n}_h, M = -\mathbf{r}_h \cdot \mathbf{n}_\phi = -\mathbf{r}_\phi \cdot \mathbf{n}_h, N = -\mathbf{r}_\phi \cdot \mathbf{n}_\phi \tag{2.50}$$

Since $\mathbf{r}_h$, $\mathbf{r}_\phi$, $\mathbf{n}_h$ and $\mathbf{n}_\phi$ have been determined in Eqs. (2.43) $\sim$ (2.46), the coefficients of the first and second fundamental forms can be obtained, then the normal curvature can be calculated with Eq. (2.48).

At a given point on a regular surface, the principal curvatures are the maximum and minimum normal curvatures at this point, and the corresponding directions are principal directions. The principal curvatures are related with Gaussian curvature and mean curvature [7, p. 181]

$$K = \kappa_1 + \kappa_2, H = \kappa_1 \cdot \kappa_2 \tag{2.51}$$

where κ_1 and κ_2 are the principal curvatures, K and H are the Gaussian curvature and mean curvature, respectively. K and H are determined as [7, p. 188]

$$K = \frac{L \cdot N - M^2}{E \cdot G - F^2}, H = \frac{L \cdot G - 2 \cdot M \cdot F + N \cdot E}{2 \cdot (E \cdot G - F^2)} \tag{2.52}$$

According to Eq. (2.51), the principal curvatures can be expressed as

$$\kappa_{1,2} = \frac{K \pm \sqrt{K^2 - 4 \cdot H}}{2} \tag{2.53}$$

In order to find the principle directions, a direction parameter is used and defined as $u = dh/d\phi\,(d\phi \neq 0)$. According to Eq. (2.47), the direction of

the tangent vector $d\mathbf{r}$ is determined by u. Submitting u into Eq. (2.48), the normal curvature κ_n can be treat as a function of u

$$\kappa_n(u) = \frac{L \cdot u^2 + 2 \cdot M \cdot u + N}{E \cdot u^2 + 2 \cdot F \cdot u + G} \tag{2.54}$$

Since the principal directions correspond to the extremum of the normal curvature, we have

$$\frac{d\kappa_n(u)}{du} = 0 \tag{2.55}$$

Combining Eqs. (2.54) and (2.55), the direction parameter of the principle directions can be calculated as

$$u_{1,2} = \frac{-(L \cdot G - N \cdot E) \pm \sqrt{(L \cdot G - N \cdot E)^2 - 4 \cdot (L \cdot F - M \cdot E) \cdot (M \cdot G - N \cdot F)}}{2 \cdot (L \cdot F - M \cdot E)} \tag{2.56}$$

When $d\phi = 0$, Eq. (2.56) can not be used. For this case, another direction parameter can be defined as $v = d\phi/dh\,(dh \neq 0)$. similarly, direction parameter of the principle directions can be calculated as

$$v_{1,2} = \frac{-(L \cdot G - N \cdot E) \pm \sqrt{(L \cdot G - N \cdot E)^2 - 4 \cdot (L \cdot F - M \cdot E) \cdot (M \cdot G - N \cdot F)}}{2 \cdot (M \cdot G - N \cdot F)} \tag{2.57}$$

Rodrigues' Formula method

Another interesting method to calculate the principle curvatures and direction is derived from the famous Rodrigues' Formula [2, 7]. According to

Rodrigues' Formula, a special relation in the principle directions is existed

$$d\mathbf{n} = -\kappa_{1,2} \cdot d\mathbf{r} \tag{2.58}$$

Eq. (2.58) can be derived as

$$-\kappa_{1,2} = \frac{d\mathbf{n}}{d\mathbf{r}} = \frac{\mathbf{n}_h \cdot dh + \mathbf{n}_\phi \cdot d\phi}{\mathbf{r}_h \cdot dh + \mathbf{r}_\phi \cdot d\phi} = \frac{\mathbf{n}_h \cdot u + \mathbf{n}_\phi}{\mathbf{r}_h \cdot u + \mathbf{r}_\phi} \tag{2.59}$$

where $\mathbf{r}_h$, $\mathbf{r}_\phi$, $\mathbf{n}_h$ and $\mathbf{n}_\phi$ have been calculated in Eqs. (2.43) $\sim$ (2.46). According to Eq. (2.59), the direction parameter of the principal directions can be expressed as

$$u_{1,2} = \frac{\mathbf{n}_\phi + \kappa_{1,2} \cdot \mathbf{r}_\phi}{-(\mathbf{n}_h + \kappa_{1,2} \cdot \mathbf{r}_h)} \tag{2.60}$$

With the consideration of the scalar components of the vectors in Eq. (2.60), we have

$$u_{1,2} = \frac{\mathrm{n}_{\phi x} + \kappa_{1,2} \cdot \mathrm{r}_{\phi x}}{-(\mathrm{n}_{hx} + \kappa_{1,2} \cdot \mathrm{r}_{hx})} = \frac{\mathrm{n}_{\phi y} + \kappa_{1,2} \cdot \mathrm{r}_{\phi y}}{-(\mathrm{n}_{hy} + \kappa_{1,2} \cdot \mathrm{r}_{hy})} = \frac{\mathrm{n}_{\phi z} + \kappa_{1,2} \cdot \mathrm{r}_{\phi z}}{-(\mathrm{n}_{hz} + \kappa_{1,2} \cdot \mathrm{r}_{hz})} \tag{2.61}$$

According to Eq. (2.61), the principle curvatures can be calculated as the unknown of a quadratic equation, which can be written as

$$a_\kappa \cdot \kappa^2 + b_\kappa \cdot \kappa + c_\kappa = 0 \tag{2.62}$$

where

$$a_\kappa = \mathrm{r}_{\phi x} \cdot \mathrm{r}_{hy} - \mathrm{r}_{\phi y} \cdot \mathrm{r}_{hx}$$

$$b_\kappa = \mathrm{r}_{\phi x} \cdot \mathrm{n}_{hy} + \mathrm{r}_{hy} \cdot \mathrm{n}_{\phi x} - \mathrm{r}_{\phi y} \cdot \mathrm{n}_{hx} - \mathrm{r}_{hx} \cdot \mathrm{n}_{\phi y}$$

$$c_\kappa = \mathrm{n}_{\phi x} \cdot \mathrm{n}_{hy} - \mathrm{n}_{\phi y} \cdot \mathrm{n}_{hx}$$

With Eq. (2.62), the principle curvatures are calculated as

$$\kappa_{1,2} = \frac{-b_\kappa \pm \sqrt{b_\kappa^2 - 4 \cdot a_\kappa \cdot c_\kappa}}{2 \cdot a_\kappa} \tag{2.63}$$

The direction parameter of the principle directions can be obtained by submitting the principle curvatures into Eq. (2.61), then the principle directions are also calculated.

Chapter 3

A new ruled tooth surface design of spiral bevel gears

3.1 The geometric model of spiral bevel gears

3.1.1 The blank model of spiral bevel gears

The blank design of the spiral bevel gear is considered as the preliminary desgin. According to the work requirements, the blank data can be determined based on the standard, such as [78]. Fig. 3.1 is the blank data of a pair of spiral bevel gear of Duplex depth type or Tilted Root Line (TRL) type, and the shaft angle is $\Sigma = 90°$. The nomenclatures of spiral bevel gears in Fig. 3.1 are shown in Table 3.1. The details can be referred to [78].

Points **A** $\sim$ **I** and Points **A'** $\sim$ **I'** are used to define the blank geometric dimensions. Since Points **A'** $\sim$ **I'** are symmetrical to points **A** $\sim$ **I** along gear axis, we just need to calculate points **A** $\sim$ **I** in gear coordinate system S_g are shown in Table 3.2. And this process is similar to pinion blank. The nomenclatures about Table 3.2 can be referred to Table 3.1. The details

about the nomenclature can be referred to [78]. By the way, one important issue is that the gear root cone generatrix is parallel with pinion face cone generatrix, and the pinion root cone generatrix is parallel with gear face cone generatrix. This issue is used to calculate the dedendum of the pinion or gear along their pith cones.

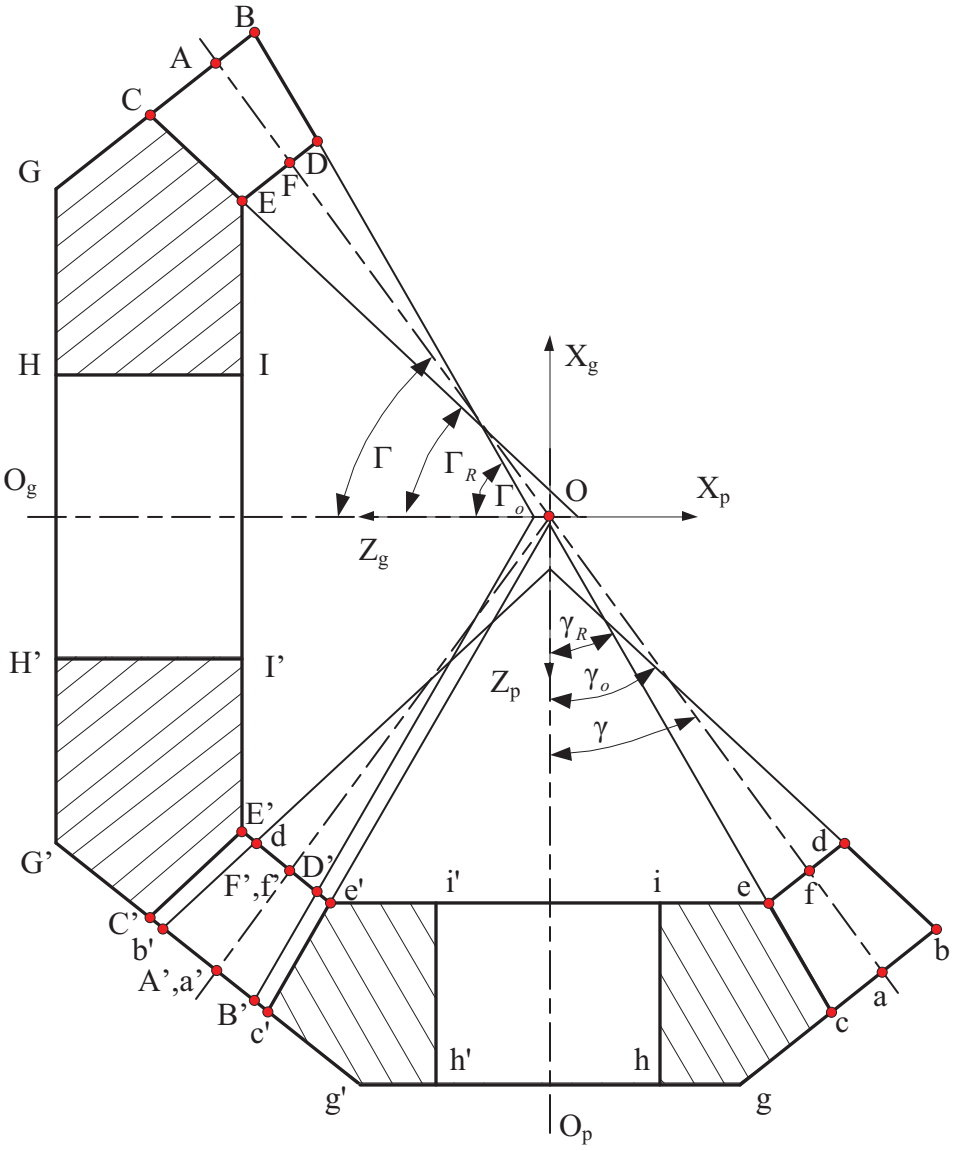

Figure 3.1: The geometry of the blanks of a pair of spiral bevel gears

Table 3.1: The nomenclature of spiral bevel gears

Sign	mean	Sign	mean
A_{o}	outer cone distance	F	face width
a_{oG}	gear outer addenduma	a_{oP}	pinion outer addendum
b_{oG}	gear outer dedendum	b_{oP}	pinion outer dedendum
δ_{G}	gear dedendum angle	δ_{P}	pinion dedendum angle
Γ_{o}	gear face angle	γ_{o}	pinion face angle
Γ_{R}	gear root angle	γ_{R}	pinion root angle

A pair of spiral bevel gear with the blank data as shown in Table 3.3 is used as an example. With the given blank data, the 3D models are modeled in CATIA V5R20 as shown Fig. 3.2.

Table 3.2: The dimension calculation of blank data

Gear points in S_{g}	pinion points in S_{p}
$\mathbf{A} = A_{\mathrm{o}} \cdot \begin{bmatrix} \sin\Gamma \\ \cos\Gamma \end{bmatrix}$	$\mathbf{a} = A_{\mathrm{o}} \cdot \begin{bmatrix} \sin\gamma \\ \cos\gamma \end{bmatrix}$
$\mathbf{B} = \mathbf{A} + a_{\mathrm{oG}} \cdot \begin{bmatrix} \cos\Gamma \\ -\sin\Gamma \end{bmatrix}$	$\mathbf{b} = \mathbf{a} + a_{\mathrm{oP}} \cdot \begin{bmatrix} \cos\gamma \\ -\sin\gamma \end{bmatrix}$
$\mathbf{C} = \mathbf{A} + b_{\mathrm{oG}} \cdot \begin{bmatrix} -\cos\Gamma \\ \sin\Gamma \end{bmatrix}$	$\mathbf{c} = \mathbf{a} + b_{\mathrm{oP}} \cdot \begin{bmatrix} -\cos\gamma \\ \sin\gamma \end{bmatrix}$
$\mathbf{D} = \mathbf{B} + \frac{F}{\cos\delta_{\mathrm{p}}} \cdot \begin{bmatrix} -\sin\Gamma_{\mathrm{o}} \\ -\cos\Gamma_{\mathrm{o}} \end{bmatrix}$	$\mathbf{d} = \mathbf{b} + \frac{F}{\cos\delta_{\mathrm{G}}} \cdot \begin{bmatrix} -\sin\gamma_{\mathrm{o}} \\ -\cos\gamma_{\mathrm{o}} \end{bmatrix}$
$\mathbf{E} = \mathbf{C} + \frac{F}{\cos\delta_{\mathrm{G}}} \cdot \begin{bmatrix} -\sin\Gamma_{\mathrm{R}} \\ -\cos\Gamma_{\mathrm{R}} \end{bmatrix}$	$\mathbf{e} = \mathbf{c} + \frac{F}{\cos\delta_{\mathrm{P}}} \cdot \begin{bmatrix} -\sin\gamma_{\mathrm{R}} \\ -\cos\gamma_{\mathrm{R}} \end{bmatrix}$

3.1.2 The tooth surface model of the conventional generated face-milled spiral bevel gear

Tooth surface geometry is the significant factor to determine the work performance of a pair of spiral bevel gears. It is used as the input to evaluate the contact pattern and transmission error. Generally, the tooth surface

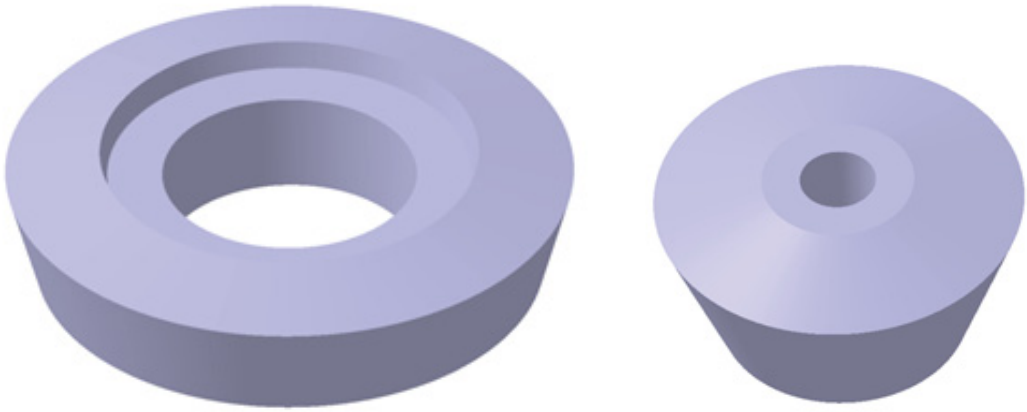

(a) Gear blank (b) Pinion blank

Figure 3.2: 3D models of the blanks of a pair of spiral bevel gears

Table 3.3: Blank data of a pair of spiral bevel gears

parameter	value
pinion tooth number	9
gear tooth number	33
module	4.8338
shaft angle	90.0000°
pinion handle	Right hand
mean spiral angle	32°
face width	27.5000 mm
outer addendum	1.7600 mm
outer dedendum	7.6700 mm
face angle	76.1167°
root angle	69.5833°

geometry is determined by the manufacturing process, which including the manufacturing approaches, machining settings, cutter geometry, etc. To better understand the conventional tooth surface geometry, The example of a face-milled spiral bevel gear generated on a Gleason's CNC machine is illustrated in this Section. This example is introduced from Litvin's work [2]. First, the generating process of the face-milled spiral bevel gear is stated. Second, kinematic relation is established for the generating process. Third, the head-cutter surfaces are illustrated as the generating surfaces. Lastly, the tooth surface is calculated with the geometric envelope approach.

The generating process of face-milled spiral bevel gears

When spiral bevel gears are generated with the face-milled method, the cutting process is a single indexing process. For each tooth side or slot, it is generated with a separate process. When the current tooth side or slot is finished, the generating process is interrupted and then the workspace is indexed to the next tooth side or slot. This process is repeated till the whole generating process is finished.

Fig. 3.3 is the simulate model of a face-milled machine tool used in Gleason. There are three rotation motions are involved in the cutting process: rotation (1) of the head-cutter along the head-cutter axis z_g, rotation (2) of the cradle along the cradle axis z_c and rotation (3) of the gear along the gear axis z_b. In industry, the generating process of face-milled spiral bevel gears can be classified as non-generated (also called as Formate®) or generated methods, and the corresponding gears are non-generated gears or generated gears, re-

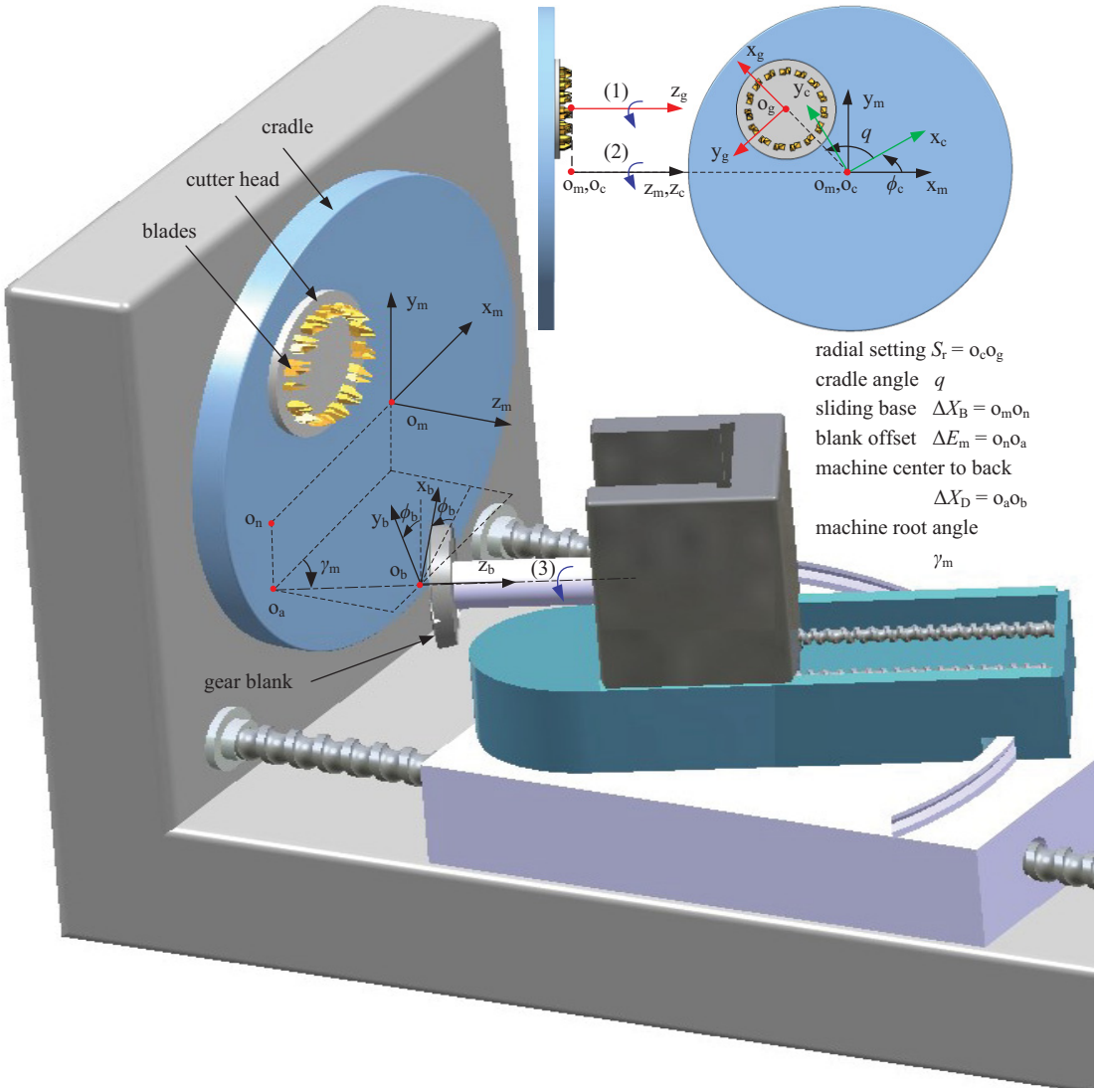

Figure 3.3: Structure and kinematic motion for the generation of face-milled spiral bevel gears

spectively. For the non-generated method, the gear is static, which means there is no rotation (3). On the contrary, rotation (3) is applied in generated method. Generally, the non-generated method offers higher productivity than the generated method. However, the generated method provides more freedom to control the tooth surface and its curvature, which are significant to the contact and transmission of the gear drive. Theoretically, the tooth surface of the non-generated gear is a part of the head-cutter surface. In contrast, the tooth surface of the generated gear is more complicated, and it is a part of the envelope surface of the family of the head-cutter surfaces in the generating process.

Since the head-cutter is mounted on the cradle, the motion of the head-cutter can be treated as a planetary motion which comprises rotations of (1) and (2). Rotation (1) is the relative motion (relative to the cradle), and rotation (2) is the transfer motion (with the cradle). Rotation (1) is chosen to provide the desired cutting velocity, and theoretically, it does not affect the result of the gear model. For generated method, rotations (2) and (3) are related, and they are called rolling or generating motions. The so-called ratio of roll or velocity ratio is used to define the relation between these two rotations, and it can be constant or varied. When ratio of roll is constant, it can be represented as

$$\phi_b(\phi_c) = m_{bc} \cdot \phi_c \tag{3.1}$$

where ϕ_b and ϕ_c are the rotation angles of the gear rotation and the cradle rotation, respectively. When the ratio of roll is varied in the generating

process, it is called as modified roll, and the corresponding modified roll function is expressed as [79]

$$\phi_b(\phi_c) = m_{bc} \cdot \left(\phi_c - C \cdot \phi_c^2 - D \cdot \phi_c^3 - E \cdot \phi_c^4 - F \cdot \phi_c^5\right) \tag{3.2}$$

where C, D, E, F are referred as the modified roll coefficients. By the way, the first and second derivatives of the modified roll function with respect to ϕ_c will be used to later calculation, and we have

$$\begin{aligned} \frac{d\phi_b}{d\phi_c} &= m_{bc} \cdot \left(1 - 2 \cdot C \cdot \phi_c - 3 \cdot D \cdot \phi_c^2 - 4 \cdot E \cdot \phi_c^3 - 5 \cdot F \cdot \phi_c^4\right) \\ \frac{d^2\phi_b}{d\phi_c^2} &= m_{bc} \cdot \left(-2 \cdot C - 6 \cdot D \cdot \phi_c - 12 \cdot E \cdot \phi_c^2 - 20 \cdot F \cdot \phi_c^3\right) \end{aligned} \tag{3.3}$$

Kinematic relation

Table 3.4: Main data of face-milling a spiral bevel gear

blade data		machine-settings	
parameter	value	parameter	value
average radius	63.5000 mm	radial setting	64.3718 mm
point width	2.5400 mm	cradle angle	-56.7800°
pressure angle	22.0000°	sliding base	0.0000 mm
fillet radius	1.5240 mm	blank offset	-0.2071 mm
		machine center to back	0.0000 mm
		machine root angle	69.5900 °
		roll ratio	1.0323
		modified roll coefficients	0.0000

The kinematic relation of the generating process can be defined base on several machine settings, as shown in Fig. 3.3. The installment of the cradle is determined by the parameters S_r and q, which are called as radial distance

and cradle angle, respectively. The settings of a generated spiral bevel gear is represented by other four parameters, and they are sliding base ΔX_B, blank offset ΔE_m, machine center to back ΔX_D and machine root angle γ_m. These machine-settings are applied in this example with the values shown in Table 3.4.

To conduct the computation with the proposed approach, a coordinate system should be chosen. Two coordinate systemes are popularly chosen in previous research. As shown in Fig. 3.3, one is the machining coordinate system $\mathrm{S_m}(\mathrm{o_m}; \mathrm{x_m}, \mathrm{y_m}, \mathrm{z_m})$, the other is the gear coordinate system $\mathrm{S_b}(\mathrm{o_b}; \mathrm{x_b}, \mathrm{y_b}, \mathrm{z_b})$. When $\mathrm{S_m}$ is chosen [17], it is convenient to represent the kinematic motion with respect to $\mathrm{S_m}$ because both the cradle and the gear blank have only one rotation operation (besides the translation operation). However, the final result need to be transformed from $\mathrm{S_m}$ to $\mathrm{S_b}$ since the tooth surface is usually defined in $\mathrm{S_b}$. On the other hand, when $\mathrm{S_b}$ is chosen [2], the result is direct obtained in $\mathrm{S_b}$, but the expression of the cradle motion in $\mathrm{S_b}$ is more complicated because it is involved two rotation operations. Both of these coordinate systems can be applied in the proposed approach, and $\mathrm{S_b}$ is chosen as an example to show the convenience of the proposed approach.

When the generating process is considered in a three dimensional Euclidean space $\mathbb{E}^3_b$, where the gear and $\mathrm{S_b}$ are fixed, the generating process can be treated as an equivalent generated motion as shown in Fig. 3.4. While the gear is fixed in $\mathbb{E}^3_b$, the head-cutter not only rotates about the cradle axis with an angle ϕ_c but also rotates about the gear axis with another angle $-\phi_b$. Then tooth surface model is formed as the envelope surface of the family

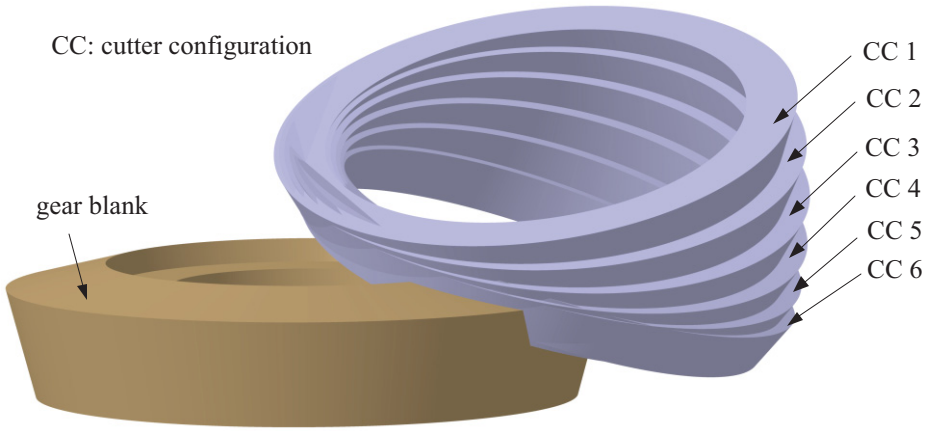

Figure 3.4: Equivalent generated motion with respect to the gear coordinate system

of the head-cutter surfaces. In order to calculate this envelope surface, it is necessary to describe the instantaneous configuration of the head-cutter surfaces with respect to S_b. This can be implemented with the HTM which transfers the head-cutter surfaces from S_g to S_b, and it can be represented as

$$\mathbf{M}_{bg}(\phi_c) = \begin{bmatrix} M_{11} & M_{12} & M_{13} & M_{14} \\ M_{21} & M_{22} & M_{23} & M_{24} \\ M_{31} & M_{32} & M_{33} & M_{34} \\ 0 & 0 & 0 & 1 \end{bmatrix} \tag{3.4}$$

The details about the derivation of $\mathbf{M}_{bg}(\phi_c)$ and its components $M_{i,j}(i = 1,2,3; j = 1,2,3,4)$ are given in Appendix A.

Head-cutter surface

The head-cutter with the blade cutting edges of a straight line with circular fillet is illustrated in this example. Each side of the blade cutting edges comprises two segments, the straight line and the circular fillet. The segment

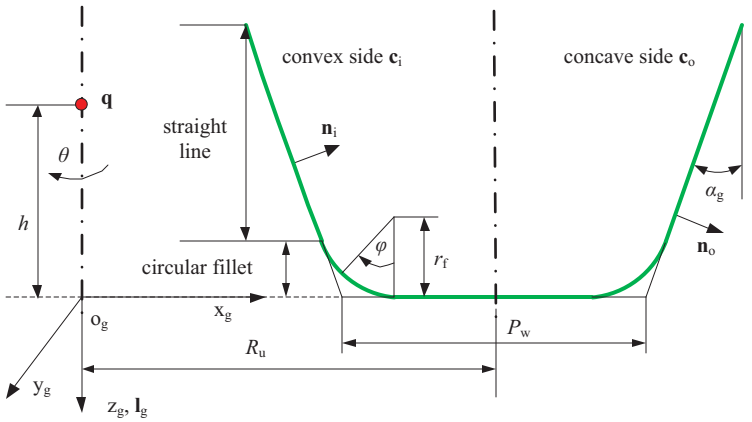

Figure 3.5: Blade cutting edges of a straight line with a circular fillet

of the straight line with the profile angle α_g generates the working part of the gear tooth surface. The circular arc of radius r_f generates the fillet of the tooth surface. Therefore, the generating surfaces, which are the head-cutter surfaces, are the surfaces of revolution formed by rotating the blade cutting edges about the head-cutter axis $\mathbf{l}_g$. The parameters of the blade cutting edges in this example are shown in Table 3.4.

The working part of head-cutter surface can be represented as

$$\mathbf{r}(h,\theta) = \mathbf{o}_g + h \cdot \mathbf{l}_g + \rho(h) \cdot \mathbf{n}(h,\theta) \tag{3.5}$$

where

$$\rho(h) = R_c(h) \cdot \csc\alpha(h), R_c(h) = \left(R_u \pm \frac{P_w}{2} \pm h \cdot \tan\alpha_g\right), \alpha(h) = \csc\left(\frac{\pi}{2} \mp \alpha_g\right)$$

The upper and lower sign refer to the concave and convex side, respectively. By the way, the derivatives of $\alpha(h)$ and $\rho(h)$ with respect to h will be used

to curvature analysis, and they are given as

$$\frac{d\alpha(h)}{dh} = 0, \frac{d\rho(h)}{dh} = \tan\alpha_g \cdot \csc\left(\frac{\pi}{2} \mp \alpha_g\right) \tag{3.6}$$

Similarly, the fillet of the head-cutter surface can be represented as

$$\mathbf{r}(\varphi,\theta) = \mathbf{o}_{\mathrm{g}} + h(\varphi)\cdot\mathbf{l}_{\mathrm{g}} + \rho(\varphi)\cdot\mathbf{n}(\varphi,\theta), \varphi \subseteq \left(0, \frac{\pi}{2} - \alpha_g\right] \tag{3.7}$$

where

$$h(\varphi) = r_c - X_w \cdot \cot\varphi = r_c - \left[R_u \pm \frac{P_w}{2} \mp r_c \cdot (\sec\alpha_g - \tan\alpha_g)\right] \cdot \cot\varphi$$
$$\rho(\varphi) = R_c(\varphi) \cdot \csc\alpha(\varphi) = (X_w \pm r_c \cdot \sin\varphi) \cdot \csc\left[\frac{\pi}{2} \pm (\varphi - \frac{\pi}{2})\right]$$

Particularly, when $\varphi = 0$, the proposed method is can not be used because of $h(\varphi)\ |_{\varphi=0} = +\infty$ and $\rho(\varphi)\ |_{\varphi=0} = +\infty$. However, the equation of meshing can be applied to calculate the contact points for this case.

Tooth surface

According to Eq. (2.34), we have to calculate $\mathbf{o}_{\mathrm{g}}(\phi_c)$, $\mathbf{l}_{\mathrm{g}}(\phi_c)$, $\mathbf{v}_q(h,\phi_c)$ and $\mathbf{v}_q(\varphi,\phi_c)$ to obtain the closed-form expression of the tooth surface, and $\mathbf{v}_q(h,\phi_c)$ and $\mathbf{v}_q(\varphi,\phi_c)$ are calculated for the working part and fillet of the tooth surface, respectively. When we consider the instantaneous configuration of the head-cutter surface in $\mathrm{S_g}$, we have

$$\mathbf{o}_{\mathrm{g}}^{\mathrm{g}} = \begin{bmatrix}0 & 0 & 0\end{bmatrix}^T, \mathbf{l}_{\mathrm{g}}^{\mathrm{g}} = \begin{bmatrix}0 & 0 & 1\end{bmatrix}^T \tag{3.8}$$

While we consider the instantaneous configuration of the head-cutter surface with respect to S_b, we can transform them from S_g to S_b as

$$\mathbf{o}_g^b(\phi_c) = \mathbf{M}_{bg}(\phi_c) \cdot \mathbf{o}_g^g = \begin{bmatrix} M_{14} & M_{24} & M_{34} \end{bmatrix}^T \tag{3.9}$$

$$\mathbf{l}_g^b(\phi_c) = \mathbf{M}_{bg}(\phi_c) \cdot \mathbf{l}_g^g = \begin{bmatrix} M_{13} & M_{23} & M_{33} \end{bmatrix}^T \tag{3.10}$$

According to Eqs. (3.9) and (3.10), $\mathbf{v}_q(h, \phi_c)$ can be calculate in S_b as

$$\mathbf{v}_q^b(h, \phi_c) = \frac{d\mathbf{o}_g^b(\phi_c)}{d\phi_c} + h \cdot \frac{d\mathbf{l}_g^b(\phi_c)}{d\phi_c} = \begin{bmatrix} \frac{dM_{14}}{d\phi_c} & \frac{dM_{24}}{d\phi_c} & \frac{dM_{34}}{d\phi_c} \end{bmatrix}^T + h \cdot \begin{bmatrix} \frac{dM_{13}}{d\phi_c} & \frac{dM_{23}}{d\phi_c} & \frac{dM_{33}}{d\phi_c} \end{bmatrix}^T \tag{3.11}$$

where $dM_{i3}/d\phi_c$ and $dM_{i4}/d\phi_c$ ($i = 1, 2, 3$) are given in Eq. (A.3) in Appendix. $\mathbf{v}_q(\varphi, \phi_c)$ can be obtained by replacing h in Eq. (3.11) with $h(\varphi)$ in Eq. (3.7). By submitting Eqs. (3.9) $\sim$ (3.11) into Eq. (2.34), the closed-form representation of the tooth surface is obtained. Moreover, the 3D model of this example is obtained in CATIA V5R20 as shown in Fig. 3.6.

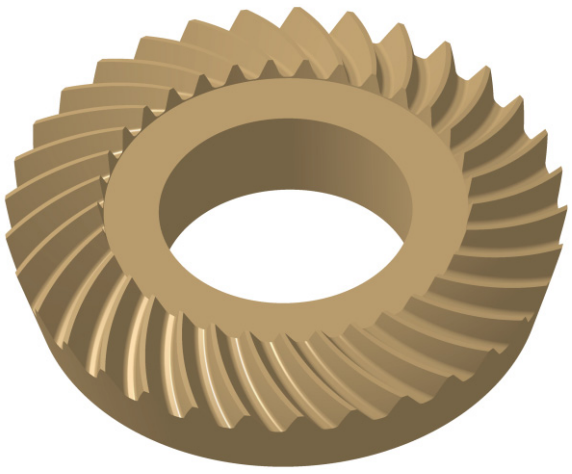

Figure 3.6: 3D gear model of a generated face-milled spiral bevel gear

Curvature analysis

Curvature analysis is only conduct to the working part of the tooth surface. As stated in Section 2.3.2, the curvature analysis can be implemented with $\mathbf{r}_h$, $\mathbf{r}_\phi$, $\mathbf{n}_h$, and $\mathbf{n}_\phi$. According to Eqs. (4.7) $\sim$ (2.46), we have to calculate $\mathbf{l}$, $\mathbf{v}_q$ and their derivatives with respect to both h and ϕ to obtain $\mathbf{r}_h$, $\mathbf{r}_\phi$, $\mathbf{n}_h$, and $\mathbf{n}_\phi$. $\mathbf{l}$ and $\mathbf{v}_q$ have been calculated in Eqs. (3.10) and (3.11), then we have

$$\frac{d\mathbf{l}_{\mathrm{g}}^{\mathrm{b}}(\phi_c)}{dh} = 0 \tag{3.12}$$

$$\frac{d\mathbf{l}_{\mathrm{g}}^{\mathrm{b}}(\phi_c)}{d\phi_c} = \begin{bmatrix} \dfrac{dM_{13}}{d\phi_c} & \dfrac{dM_{23}}{d\phi_c} & \dfrac{dM_{33}}{d\phi_c} \end{bmatrix}^T \tag{3.13}$$

$$\frac{d\mathbf{v}_q^{\mathrm{b}}(h,\phi_c)}{dh} = \frac{d\mathbf{l}_{\mathrm{g}}^{\mathrm{b}}(\phi_c)}{d\phi_c} \tag{3.14}$$

$$\frac{d\mathbf{v}_q^{\mathrm{b}}(h,\phi_c)}{d\phi_c} = \begin{bmatrix} \dfrac{d^2M_{14}}{d\phi_c^2} & \dfrac{d^2M_{24}}{d\phi_c^2} & \dfrac{d^2M_{34}}{d\phi_c^2} \end{bmatrix}^T + h \cdot \begin{bmatrix} \dfrac{d^2M_{13}}{d\phi_c^2} & \dfrac{d^2M_{23}}{d\phi_c^2} & \dfrac{d^2M_{33}}{d\phi_c^2} \end{bmatrix}^T \tag{3.15}$$

where $d^2M_{i3}/d\phi_c^2$ and $d^2M_{i4}/d\phi_c^2$ ($i = 1, 2, 3$) are given in Eq. (A.4) in Appendix A.

3.1.3 Result validation and computation efficiency comparison

As a verification and comparison, the tooth surface and its curvatures of the aforementioned example are also calculated with Litvin's approach. In Litvin's approach, the tooth surface is calculated with the equation of meshing, and the curvature of the tooth surface is computed with theory of gearing. The results of the proposed method and Litvin's approach are the

same. Therefore, the proposed method is valid.

Considering the computation efficiency, the comparison of the proposed method and Litvin's method is implemented to the calculation of the tooth surface and its curvatures, respectively. All computations are implemented with MATLAB R2010b on a 64-bit machine with Intel Core i5-2520M 2.50 GHz CPU and 4 GB main memory.

Table 3.5: Efficiency comparison of the calculation of the contact points

Case	Point number	Geometric envelope approach		Equation of meshing
		Time (s)	Ratio	Time(s)
1	100 × 100	0.193	65.2%	0.296
2	100 × 1000	0.895	45.9%	1.950

Table 3.6: Efficiency comparison of the implementation of the curvature analysis

Case	Point number	Fundamental form		Rodrigues' Formula		Theory of gearing
		Time (s)	Ratio	Time (s)	Ratio	Time (s)
1	100 × 100	0.574	84.8%	0.566	83.6%	0.677
2	100 × 1000	4.692	81.3%	4.509	78.1%	5.770

For the calculation of the tooth surface, the proposed geometric envelope approach is compared with the equation of meshing, and the comparison is shown in Table 3.5. Two cases with different numbers of the contact points are carried out for the convex side of the tooth surface. The number of the contact points is given by multiplying the number of the contact lines and the number of the contact points on each contact line. The ratio is calculated as a ratio of the computation time of the proposed method to the computation time of Litvin's method. According to Table 3.5, it illustrates that the proposed method is more efficient than Litvin's method.

For the calculation of the curvatures, both two proposed methods, fundamental form method and Rodrigues' Formula method, are compared with the method of theory of gearing, and the comparison is shown in Table 3.6. According to Table 3.6, both two proposed methods are more efficient than Litvin's method, and the Rodrigues' Formula method is the most efficient method.

Moreover, since it is usually an iterative process to find reasonable parameters to manufacture the spiral bevel gears, the proposed method is helpful to reduce the calculation time.

3.2 Ruled tooth surface design of spiral bevel gears

3.2.1 Tooth surface design of spiral bevel gears

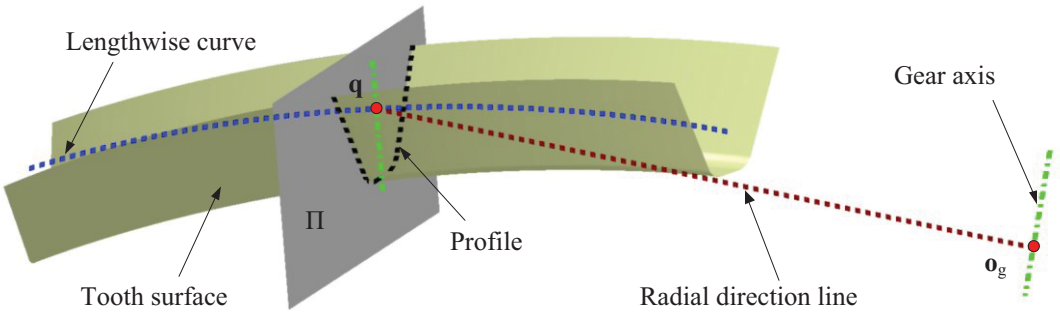

Figure 3.7: The lengthwise curve and profile of a tooth surface.

The tooth surface geometry is usually described with a lengthwise curve and a series of profiles, as shown in Fig. 3.7. The lengthwise curve is a curve defined on the pitch cone of the spiral bevel gear. Assuming that **q** is a point on the lengthwise curve, the profile corresponding to **q** is defined as

the intersection of the tooth surface with a plane $\prod$. $\prod$ is the plane passing through $\mathbf{q}$ and perpendicular to radial direction $\mathbf{o}_g\mathbf{q}$, in which $\mathbf{o}_g$ is the pitch cone apex.

It is still not clear about the precise nature of the effects of slight changes in the tooth surface geometry of high precision and high performance spiral bevel gears. Any reasonable shape can be chosen for both the lengthwise curve and profile [32]. Since the working part of the tooth surface generated from conventional approaches is close to a ruled surface, here we proposed a new ruled tooth surface design for five-axis flank milling spiral bevel gears. Ruled surface is the result of the movement of a line, named as rule, along a guiding curve. The details about ruled surface can be referred to [35,80]. For the proposed ruled tooth surface design, the lengthwise curve is the guiding curve. The working part of the profile is defined with two rules. Consequently, the ruled tooth surface design is obtained.

3.2.2 The circular lengthwise curve of the ruled tooth surface

For the lengthwise curve, currently used shapes includes straight line, circle, trochoid, involute and logarithmic spiral. The vast majority of spiral bevel gears in use are of the circular lengthwise curvature type [32]. Hence, we choose the circular lengthwise curve for the ruled tooth surface design. The corresponding design procedure can be applied to the other choices of the lengthwise curve.

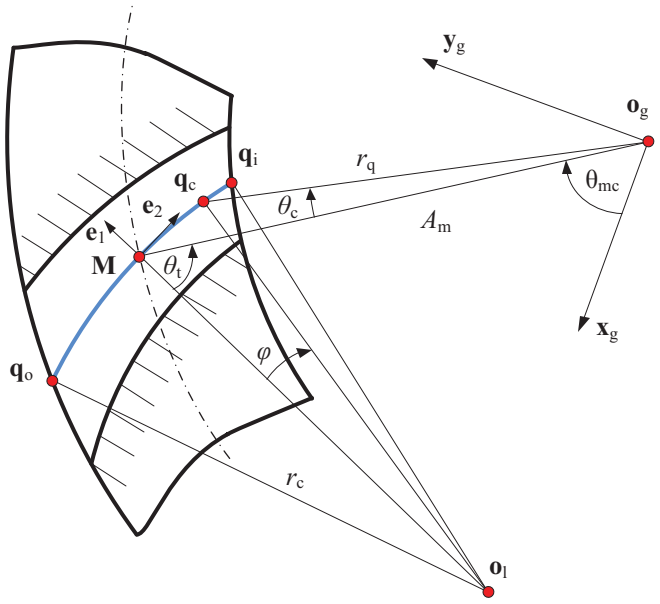

Figure 3.8: Circular lengthwise curve of the crown gear

Circular lengthwise curve of crown gears

For a crown gear, the circular lengthwise curve of a tooth is considered as a given arc in the reference plane of the crown gear. The reference plane becomes the pitch cone when the crown gear is spindled into a spiral bevel gear. Fig. 3.8 is a partial view about the intersection of the crown gear tooth flanks with the reference plane. $\mathbf{q}_o\mathbf{M}\mathbf{q}_i$ is the circular lengthwise curve, which can be defined with given mean point $\mathbf{M}$ and arc center point $\mathbf{o}_l$.

A coordinate system $S_g\left(\mathbf{o}_g;\mathbf{x}_g,\mathbf{y}_g,\mathbf{z}_g\right)$ fixed in the reference plane is established as shown in Fig. 3.8. $\mathbf{o}_g$ is the intersection point of the gear axis with the reference plane. $\mathbf{z}_g$ is the unit normal direction of the reference plane, and it directs from pitch cone apex to back cone apex. $\mathbf{M}$ is defined in S_g by

given the mean cone distance A_{m} and an initial angle θ_{mc}. We have

$$\mathbf{M} = A_{\mathrm{m}} \cdot \begin{bmatrix} \cos\theta_{\mathrm{mc}} & \sin\theta_{\mathrm{mc}} & 0 \end{bmatrix}^T. \tag{3.16}$$

Assume that $\mathbf{e}_1$ is the unit vector from $\mathbf{o}_{\mathrm{l}}$ to $\mathbf{M}$, and $\mathbf{e}_2$ is the unit tangent vector of $\mathbf{q}_{\mathrm{o}}\mathbf{M}\mathbf{q}_{\mathrm{i}}$ at $\mathbf{M}$. We have

$$\mathbf{e}_1 = \begin{bmatrix} \cos\left(\theta_{\mathrm{mc}} + \theta_{\mathrm{t}}\right) \\ \sin\left(\theta_{\mathrm{mc}} + \theta_{\mathrm{t}}\right) \\ 0 \end{bmatrix}, \mathbf{e}_2 = \begin{bmatrix} -\sin\left(\theta_{\mathrm{mc}} + \theta_{\mathrm{t}}\right) \\ \cos\left(\theta_{\mathrm{mc}} + \theta_{\mathrm{t}}\right) \\ 0 \end{bmatrix}. \tag{3.17}$$

$\mathbf{o}_{\mathrm{l}}$ is defined in S_{g} by given θ_{t} and r_{c}. θ_{t} is the commentary to spiral angle, which is given in gear design and defined as the angle between $\mathbf{e}_2$ and $\mathbf{M}\mathbf{o}_{\mathrm{g}}$. In conventional methods of spiral bevel gear manufacturing, r_{c} is the cutter radius chosen based on gear design and manufacturing methods. Here we can chosen r_{c} according to Gleason calculations for face milling methods. The details about how to chosen r_{c} can be referred to [78]. We have

$$\mathbf{o}_{\mathrm{l}} = \mathbf{M} - r_{\mathrm{c}} \cdot \mathbf{e}_1 = \begin{bmatrix} A_{\mathrm{m}} \cdot \cos\theta_{\mathrm{mc}} - r_{\mathrm{c}} \cdot \cos\left(\theta_{\mathrm{mc}} + \theta_{\mathrm{t}}\right) \\ A_{\mathrm{m}} \cdot \sin\theta_{\mathrm{mc}} - r_{\mathrm{c}} \cdot \sin\left(\theta_{\mathrm{mc}} + \theta_{\mathrm{t}}\right) \\ 0 \end{bmatrix}. \tag{3.18}$$

An arbitrary point $\mathbf{q}_{\mathrm{c}}$ on $\mathbf{q}_{\mathrm{o}}\mathbf{M}\mathbf{q}_{\mathrm{i}}$ can be expressed with parameter φ, which is the angle from $\mathbf{o}_{\mathrm{l}}\mathbf{M}$ to $\mathbf{o}_{\mathrm{l}}\mathbf{q}_{\mathrm{c}}$. We have

$$\begin{aligned} \mathbf{q}_{\mathrm{c}}(\varphi) &= \mathbf{o}_{\mathrm{l}} + \mathbf{o}_{\mathrm{l}}\mathbf{q}_{\mathrm{c}} = \mathbf{o}_{\mathrm{l}} + r_{\mathrm{c}} \cdot \left(\mathbf{e}_1 \cdot \cos\varphi + \mathbf{e}_2 \cdot \sin\varphi\right) \\ &= \begin{bmatrix} A_{\mathrm{m}} \cdot \cos\theta_{\mathrm{mc}} - r_{\mathrm{c}} \cdot \cos\left(\theta_{\mathrm{mc}} + \theta_{\mathrm{t}}\right) + r_{\mathrm{c}} \cdot \cos\left(\theta_{\mathrm{mc}} + \theta_{\mathrm{t}} + \varphi\right) \\ A_{\mathrm{m}} \cdot \sin\theta_{\mathrm{mc}} - r_{\mathrm{c}} \cdot \sin\left(\theta_{\mathrm{mc}} + \theta_{\mathrm{t}}\right) + r_{\mathrm{c}} \cdot \sin\left(\theta_{\mathrm{mc}} + \theta_{\mathrm{t}} + \varphi\right) \\ 0 \end{bmatrix}. \end{aligned} \tag{3.19}$$

The circular lengthwise curve can also be represented with parameter θ_c, which is the angle from $\mathbf{o}_g\mathbf{M}$ to $\mathbf{o}_g\mathbf{q}_c$. We have

$$\mathbf{q}_c(\varphi) = r_q \cdot \begin{bmatrix} \cos\theta_c & \sin\theta_c & 0 \end{bmatrix}^T. \tag{3.20}$$

Assuming that $\mathbf{q}_c = [q_{cx} \;\; q_{cy}]$, θ_c can be obtained as

$$\theta_c = \arctan\left(\frac{q_{cy}}{q_{cx}}\right) - \theta_{mc}. \tag{3.21}$$

r_q is the radial distance between $\mathbf{o}_g$ and $\mathbf{q}_c$. We have

$$r_q = \sqrt{q_{cx}^2 + q_{cy}^2}. \tag{3.22}$$

Circular lengthwise of spiral bevel gears

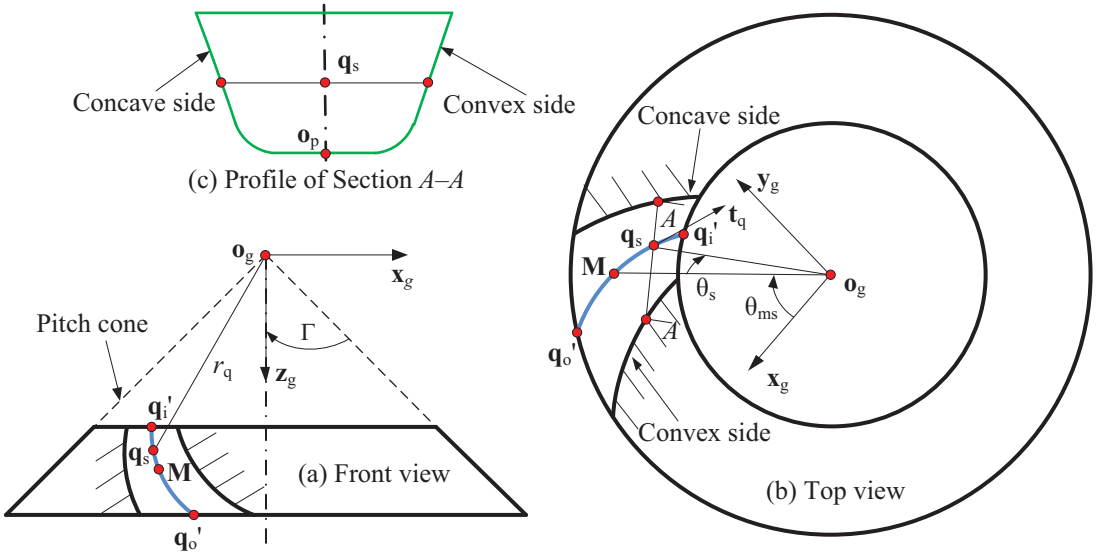

Figure 3.9: Circular lengthwise curve of the spiral bevel gear

Geometrically, a spiral bevel gear can be obtained from the crown gear, while the reference plane of the crown gear is spindled into the pitch cone

of the spiral bevel gear. Subsequently, the circular lengthwise curve of the crown gear is spindled into a new lengthwise curve on the pitch cone. As shown in Fig. 3.9, the new lengthwise curve is $\mathbf{q}'_{\mathrm{o}}\mathbf{M}\mathbf{q}'_{\mathrm{i}}$. Correspondingly, θ_{ms} and θ_{s} are used to replace θ_{mc} and θ_{c}, respectively. According to [30], we have

$$\theta_{\mathrm{ms}} = \theta_{\mathrm{mc}} \cdot \csc\Gamma, \;\; \theta_{\mathrm{s}} = \theta_{\mathrm{c}} \cdot \csc\Gamma \tag{3.23}$$

where Γ is the gear pitch angle. The parametric expression of the pitch cone in $S_{\mathrm{g}}\left(\mathbf{o}_{\mathrm{g}}; \mathbf{x}_{\mathrm{g}}, \mathbf{y}_{\mathrm{g}}, \mathbf{z}_{\mathrm{g}}\right)$ can be described as

$$\mathbf{P}\left(r, \theta\right) = r \cdot \begin{bmatrix} \sin\Gamma \cdot \cos\theta & \sin\Gamma \cdot \sin\theta & \cos\Gamma \end{bmatrix}^{T}. \tag{3.24}$$

Subsequently, the new lengthwise curve $\mathbf{q}'_{\mathrm{o}}\mathbf{M}\mathbf{q}'_{\mathrm{i}}$ can be represented with respect to parameter θ_{s} in S_{g} as

$$\mathbf{q}_{\mathrm{s}}(\theta_{\mathrm{s}}) = r_{\mathrm{q}} \cdot \begin{bmatrix} \sin\Gamma \cdot \cos\left(\theta_{\mathrm{ms}} + \theta_{\mathrm{s}}\right) & \sin\Gamma \cdot \sin\left(\theta_{\mathrm{ms}} + \theta_{\mathrm{s}}\right) & \cos\Gamma \end{bmatrix}^{T} \tag{3.25}$$

where r_{q} is obtained as Eq. (3.20). According to Eqs. (3.21) and (3.22), both r_{q} and θ_{c} are the functions with respect to parameter φ. Therefore, the parametric expression of the new lengthwise curve can also be respected to parameter φ. We will use φ to replace θ_{s} for further calculations. As a consequence, the tangent vector of this new lengthwise curve can be obtained

as the derivative of $\mathbf{q}_\mathrm{s}$ with respect to φ. We have

$$\mathbf{T}_\mathrm{q} = \frac{d\mathbf{q}_\mathrm{s}}{d\varphi} = \begin{bmatrix} \sin\Gamma \cdot \cos\left(\theta_\mathrm{ms} + \theta_\mathrm{s}\right) \cdot \dfrac{dr_\mathrm{q}}{d\varphi} - r_\mathrm{q} \cdot \sin\Gamma \cdot \sin\left(\theta_\mathrm{ms} + \theta_\mathrm{s}\right) \cdot \dfrac{d\theta_\mathrm{s}}{d\varphi} \\ \sin\Gamma \cdot \sin\left(\theta_\mathrm{ms} + \theta_\mathrm{s}\right) \cdot \dfrac{dr_\mathrm{q}}{d\varphi} + r_\mathrm{q} \cdot \sin\Gamma \cdot \cos\left(\theta_\mathrm{ms} + \theta_\mathrm{s}\right) \cdot \dfrac{d\theta_\mathrm{s}}{d\varphi} \\ \cos\Gamma \cdot \dfrac{dr_\mathrm{q}}{d\varphi} \end{bmatrix}^T \tag{3.26}$$

where

$$\begin{aligned} \frac{dr_\mathrm{q}}{d\varphi} &= \frac{r_\mathrm{c}}{r_\mathrm{q}} \cdot \left[-\mathrm{q_{cx}} \cdot \sin\left(\theta_\mathrm{mc} + \theta_\mathrm{t} + \varphi\right) + \mathrm{q_{cy}} \cdot \cos\left(\theta_\mathrm{mc} + \theta_\mathrm{t} + \varphi\right)\right] \\ \frac{d\theta_\mathrm{s}}{d\varphi} &= \frac{r_\mathrm{c} \cdot \cos\Gamma}{r_\mathrm{q}^2} \cdot \left[\mathrm{q_{cx}} \cdot \cos\left(\theta_\mathrm{mc} + \theta_\mathrm{t} + \varphi\right) + \mathrm{q_{cy}} \cdot \sin\left(\theta_\mathrm{mc} + \theta_\mathrm{t} + \varphi\right)\right]. \end{aligned}$$

The unit tangent vector of the new lengthwise curve can be calculated as

$$\mathbf{t}_\mathrm{q} = \frac{\mathbf{T}_\mathrm{q}}{|\ \mathbf{T}_\mathrm{q}\ |}. \tag{3.27}$$

3.2.3 The profile of the ruled tooth surface

As shown in Fig. 3.9, the profile is the intersection of the tooth surface and the section plane $A - A$, which passes through $\mathbf{q}_\mathrm{s}$ and normal to the radial direction $\mathbf{o}_\mathrm{g}\mathbf{q}_\mathrm{s}$. The choices of the profile shape are also various. Any profile form which obeys the basic laws of Law of Gearing can be employed conjugate action. Inspired from the fact that the work part of the profile of the generated face-milled gear is close to a straight line, here we propose the straight line design for the working part of the profile. The ruled tooth surface is formed by connecting all profiles along the lengthwise curve.

The definition of the profile is shown in Fig. 3.10. The profile is composed of two sides, the convex and concave sides. Each side has the side and bottom line segments. Additionally, an arc segment connects these two line segments. $\mathbf{p}_\mathrm{f}$ is the intersection point of the side line and arc segments. The bottom line segment with distance r_b generates the bottom of the tooth surface. The side straight line segment with pressure angle α_g generates the working part of the tooth surface. The arc segment of radius r_f generates the fillet of the tooth surface. Here we clarify that the fillet of the tooth surface is not a ruled surface, although we mention that the whole tooth surface as ruled tooth surface. To define the profile, a new coordinate system $S_\mathrm{p}\left(\mathbf{o}_\mathrm{p}; \mathbf{x}_\mathrm{p}, \mathbf{y}_\mathrm{p}, \mathbf{z}_\mathrm{p}\right)$ is

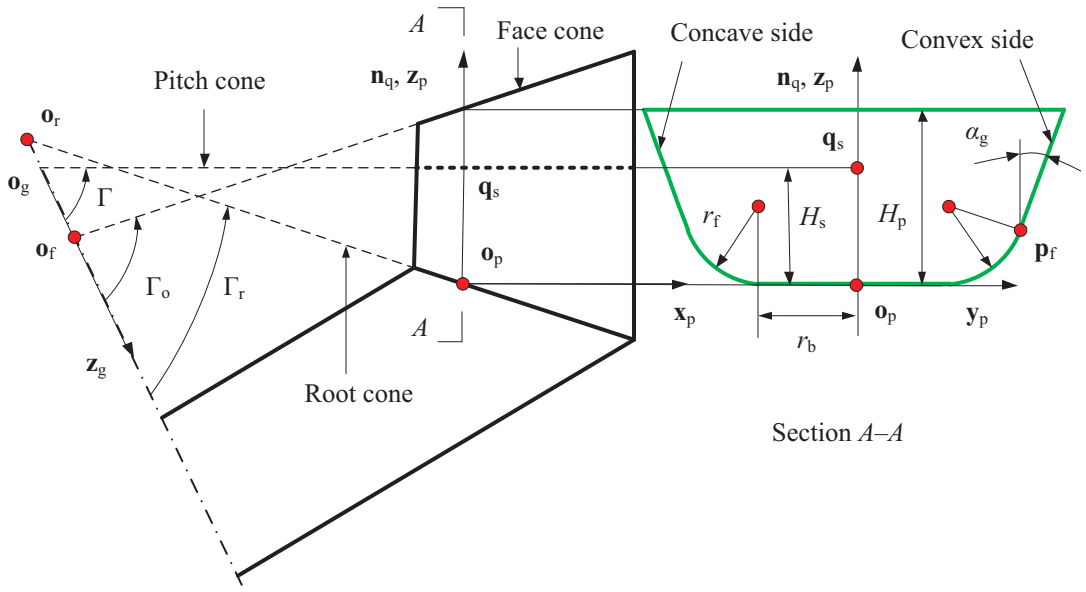

Figure 3.10: The profile definition of the ruled tooth surface.

created as shown in Fig. 3.10. $\mathbf{x}_\mathrm{p}$ is obtained as the unit vector of $\mathbf{o}_\mathrm{g}\mathbf{q}_\mathrm{s}$. $\mathbf{z}_\mathrm{p}$ is aligned with $\mathbf{n}_\mathrm{q}$, which is the unit normal of the pitch cone at $\mathbf{q}_\mathrm{s}$. $\mathbf{y}_\mathrm{p}$ is determined based on the right-hand rule. $\mathbf{o}_\mathrm{p}$ is the intersection point of $\mathbf{n}_\mathrm{q}$

and the root cone. The distance between $\mathbf{q}_\mathrm{s}$ and $\mathbf{o}_\mathrm{p}$ is H_s. H_s can be obtained as

$$H_\mathrm{s}(\varphi) = (r_\mathrm{q} + \mid \mathbf{o}_\mathrm{r}\mathbf{o}_\mathrm{g} \mid \cdot \cos\Gamma) \cdot \tan(\Gamma - \Gamma_\mathrm{r}) - \mid \mathbf{o}_\mathrm{r}\mathbf{o}_\mathrm{g} \mid \cdot \sin\Gamma \tag{3.28}$$

where Γ_r is the root angle; $\mid \mathbf{o}_\mathrm{r}\mathbf{o}_\mathrm{g} \mid$ is the distance from the root cone apex to the pitch cone apex (when the direction of $\mathbf{o}_\mathrm{r}\mathbf{o}_\mathrm{g}$ is the same with $\mathbf{z}_\mathrm{g}$, $\mid \mathbf{o}_\mathrm{r}\mathbf{o}_\mathrm{g} \mid$ is positive, or $\mid \mathbf{o}_\mathrm{r}\mathbf{o}_\mathrm{g} \mid$ is negative). Γ_r is given as gear blank data. $\mid \mathbf{o}_\mathrm{r}\mathbf{o}_\mathrm{g} \mid$ can be calculated according to the blank data as Fig. 3.11. For TRL (tileted root

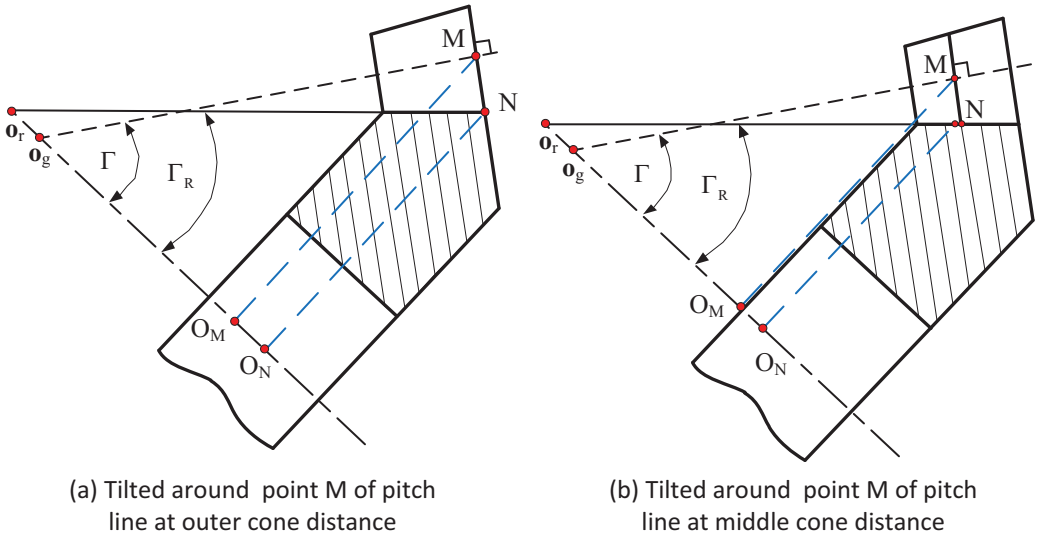

(a) Tilted around point M of pitch line at outer cone distance

(b) Tilted around point M of pitch line at middle cone distance

Figure 3.11: The distance from the root cone apex to the pitch cone apex.

line) gear, there are two types design for the pitch cone. Correspondingly, $\mid \mathbf{o}_\mathrm{r}\mathbf{o}_\mathrm{g} \mid$ has different results as

$$\mid \mathbf{o}_\mathrm{r}\mathbf{o}_\mathrm{g} \mid = \begin{cases} Case(a) & \dfrac{A_\mathrm{o} \cdot \sin\Gamma - b_\mathrm{og} \cdot \cos\Gamma}{\tan\Gamma_\mathrm{R}} - b_\mathrm{og} \cdot \sin\Gamma - A_\mathrm{o} \cdot \cos\Gamma \\ Case(b) & \dfrac{A_\mathrm{m} \cdot \sin\Gamma - b_\mathrm{g} \cdot \cos\Gamma}{\tan\Gamma_\mathrm{R}} - b_\mathrm{g} \cdot \sin\Gamma - A_\mathrm{m} \cdot \cos\Gamma \end{cases} \tag{3.29}$$

We take the case (a) as the example in this thesis. The detail calculation process of case (a) is stated as follows.

$$| \mathbf{o}_\mathrm{r}\mathbf{o}_\mathrm{g} | = | \mathbf{o}_\mathrm{r}\mathbf{o}_\mathrm{M} | - | \mathbf{o}_\mathrm{g}\mathbf{o}_\mathrm{M} | = (| \mathbf{o}_\mathrm{r}\mathbf{o}_\mathrm{N} | - | \mathbf{o}_\mathrm{M}\mathbf{o}_\mathrm{N} |) - | \mathbf{o}_\mathrm{g}\mathbf{o}_\mathrm{M} | \tag{3.30}$$

where

$$\begin{aligned} | \mathbf{o}_\mathrm{r}\mathbf{o}_\mathrm{N} | &= \frac{A_\mathrm{o} \cdot \sin\Gamma - b_\mathrm{og} \cdot \cos\Gamma}{\tan\Gamma_\mathrm{R}} \\ | \mathbf{o}_\mathrm{M}\mathbf{o}_\mathrm{N} | &= b_\mathrm{og} \cdot \sin\Gamma \\ | \mathbf{o}_\mathrm{g}\mathbf{o}_\mathrm{M} | &= A_\mathrm{o} \cdot \cos\Gamma. \end{aligned} \tag{3.31}$$

The arc segment is represented in S_p as

$$\mathbf{r}_{\mathrm{f,p}}(\alpha) = \begin{bmatrix} 0 & \pm(r_\mathrm{b} + r_\mathrm{f} \cdot \sin\alpha) & r_\mathrm{f} \cdot (1 - \cos\alpha) \end{bmatrix}^T, \quad 0 \le \alpha \le \pi/2 - \alpha_\mathrm{g}. \tag{3.32}$$

In Eq.(3.32), the item $\mathbf{r}_{\mathrm{f,p}}$ indicates the expression of vector $\mathbf{r}_\mathrm{f}$ in S_p. The other similar items in the reminder of this paper can also be explained as the same way. The upper and lower signs correspond to convex and concave sides, respectively. According to Eq.(3.32), $\mathbf{p}_\mathrm{f}$ can be obtained in S_p with $\alpha = \pi/2 - \alpha_\mathrm{g}$. We have

$$\mathbf{p}_{\mathrm{f,p}} = \begin{bmatrix} 0 & \pm(r_\mathrm{b} + r_\mathrm{f} \cdot \cos\alpha_\mathrm{g}) & r_\mathrm{f} \cdot (1 - \sin\alpha_\mathrm{g}) \end{bmatrix}^T. \tag{3.33}$$

Assuming that $\mathbf{p}_{\mathrm{f,p}} = [0 \quad \mathrm{p_{fy}} \quad \mathrm{p_{fz}}]^T$, the straight line segment can be represented in S_p as

$$\mathbf{r}_{\mathrm{l,p}}(h) = \begin{bmatrix} 0 & \mathrm{r_{ly,p}} & h \end{bmatrix}^T, \quad \mathrm{r_{ly,p}} = \pm\left[\mathrm{p_{fy}} + (h - \mathrm{p_{fz}}) \cdot \tan\alpha_\mathrm{g}\right], \quad \mathrm{p_{fz}} \le h \le H_\mathrm{p} \tag{3.34}$$

where H_{p} is the profile height, as shown in Fig. 3.10. We have

$$H_{\mathrm{p}}(\varphi) = H_{\mathrm{s}}(\varphi) + (r_{\mathrm{q}} - \mid \mathbf{o}_{\mathrm{g}}\mathbf{o}_{\mathrm{f}} \mid \cdot \cos\Gamma) \cdot \tan(\Gamma_{\mathrm{o}} - \Gamma) - \mid \mathbf{o}_{\mathrm{g}}\mathbf{o}_{\mathrm{f}} \mid \cdot \sin\Gamma \quad (3.35)$$

where Γ_{o} is the face angle and it is given as gear blank data; $\mid \mathbf{o}_{\mathrm{g}}\mathbf{o}_{\mathrm{f}} \mid$ is the distance from the pitch cone apex to the face cone apex.

3.3 Design tooth surface model and its normal

3.3.1 Geometric model of the design tooth surface

Since the profile is obtained in S_{p}, the geometric model of the design tooth surface can be obtained by transforming all profiles from S_{p} to S_{g}. Hence, it is necessary to calculate the transformation matrix from S_{p} to S_{g}. The unit normal of the pitch cone can be calculated in S_{g} according to Eq. (3.24). In this paper, we clarify that the normal direction of a surface always directs away the corresponding axis, such as the rotary axis of the pitch cone surface and the profile axis of the ruled tooth surface. For the pitch cone surface, we have

$$\mathbf{n}\,(r,\theta) = \begin{bmatrix} \cos\Gamma \cdot \cos\theta & \cos\Gamma \cdot \sin\theta & -\sin\Gamma \end{bmatrix}^{T}. \quad (3.36)$$

According to Eqs. (3.25) and (3.36), we have

$$\begin{aligned} \mathbf{x}_{\mathrm{p}}\,(\varphi) &= \begin{bmatrix} \sin\Gamma \cdot \cos\left(\theta_{\mathrm{ms}} + \theta_{\mathrm{s}}\right) & \sin\Gamma \cdot \sin\left(\theta_{\mathrm{ms}} + \theta_{\mathrm{s}}\right) & \cos\Gamma \end{bmatrix}^{T} \\ \mathbf{z}_{\mathrm{p}}(\varphi) &= \mathbf{n}_{\mathrm{q}}(\varphi) = \begin{bmatrix} \cos\Gamma \cdot \cos\left(\theta_{\mathrm{ms}} + \theta_{\mathrm{s}}\right) & \cos\Gamma \cdot \sin\left(\theta_{\mathrm{ms}} + \theta_{\mathrm{s}}\right) & -\sin\Gamma \end{bmatrix}^{T} \\ \mathbf{y}_{\mathrm{p}}(\varphi) &= \mathbf{z}_{\mathrm{p}}(\varphi) \times \mathbf{x}_{\mathrm{p}}(\varphi) = \begin{bmatrix} \sin\left(\theta_{\mathrm{ms}} + \theta_{\mathrm{s}}\right) & -\cos\left(\theta_{\mathrm{ms}} + \theta_{\mathrm{s}}\right) & 0 \end{bmatrix}^{T}. \end{aligned} \quad (3.37)$$

As shown Fig. 3.10, $\mathbf{o}_{\mathrm{p}}$ can be calculated as

$$\mathbf{o}_{\mathrm{p}}(\varphi) = \mathbf{q}_{\mathrm{s}} - H_{\mathrm{s}} \cdot \mathbf{n}_{\mathrm{q}} \tag{3.38}$$

where $\mathbf{q}_{\mathrm{s}}$ and $\mathbf{n}_{\mathrm{q}}$ are obtained in Eqs. (3.25) and (3.37), respectively. Consequently, the transformation matrix from S_{p} to S_{g} can be obtained as

$$\mathbf{M}_{\mathrm{gp}}(\varphi) = \begin{bmatrix} \mathbf{x}_{\mathrm{p}}(\varphi) & \mathbf{y}_{\mathrm{p}}(\varphi) & \mathbf{z}_{\mathrm{p}}(\varphi) & \mathbf{o}_{\mathrm{p}}(\varphi) \\ 0 & 0 & 0 & 1 \end{bmatrix} \tag{3.39}$$

Subsequently, the geometric model of the design tooth surface can be obtained in S_{g} as

$$\begin{bmatrix} \mathbf{r}_{\mathrm{f,g}}(\varphi, \alpha) & \mathbf{r}_{\mathrm{l,g}}(\varphi, h) \\ 1 & 1 \end{bmatrix} = \mathbf{M}_{\mathrm{gp}}(\varphi) \cdot \begin{bmatrix} \mathbf{r}_{\mathrm{f,p}}(\alpha) & \mathbf{r}_{\mathrm{l,p}}(h) \\ 1 & 1 \end{bmatrix}. \tag{3.40}$$

An spiral bevel gear with the proposed ruled tooth surface design is modeled as the example. The main data is show in Table 3.7. The result is implemented in CATIA V5R20. The details of the modeling process are shown in Fig. 3.12.

Table 3.7: Tooth profile design data

Parameter	Value
lengthwise curve radius	63.5000 mm
bottom line distance	1.0000 mm
profile fillet radius	1.5000 mm
side line taper angle	22.0000°

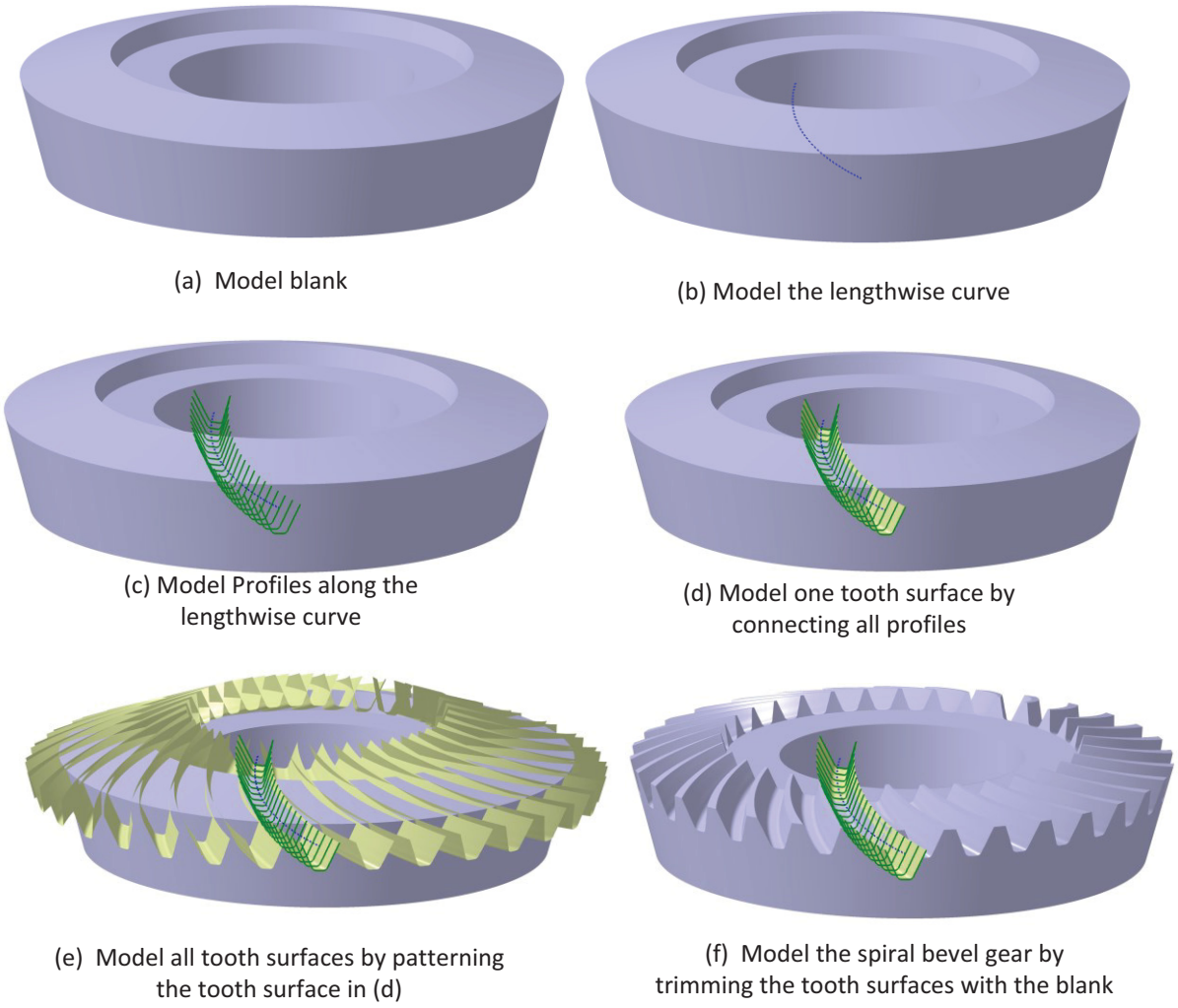

Figure 3.12: 3D gear model with ruled tooth surfaces design.

3.3.2 The normal of the design tooth surface

According to Eq. (3.40), the partial derivatives of the design tooth surface at the working part can be obtained in S_{g}. Subsequently, the unit normal of the tooth surface can be obtained in S_{g} as

$$\mathbf{n}_{\mathrm{g}}(\varphi, h) = \pm \frac{\mathbf{N}_{\varphi,\mathrm{g}} \times \mathbf{N}_{h,\mathrm{g}}}{\mid \mathbf{N}_{\varphi,\mathrm{g}} \times \mathbf{N}_{h,\mathrm{g}} \mid} \tag{3.41}$$

where upper and lower signs correspond to convex and concave sides, respectively. $\mathbf{N}_{\varphi,\mathrm{g}} \times \mathbf{N}_{h,\mathrm{g}}$ calculated as

$$\begin{aligned}\mathbf{N}_{\varphi,\mathrm{g}} \times \mathbf{N}_{h,\mathrm{g}} = {} & \pm \mathrm{r}_{\mathrm{ly,p}} \cdot \tan\alpha_{\mathrm{g}} \cdot \left(\frac{d\mathbf{y}_{\mathrm{p}}}{d\varphi} \times \mathbf{y}_{\mathrm{p}}\right) + \mathrm{r}_{\mathrm{ly,p}} \cdot \left(\frac{d\mathbf{y}_{\mathrm{p}}}{d\varphi} \times \mathbf{z}_{\mathrm{p}}\right) \\ & \pm h \cdot \tan\alpha_{\mathrm{g}} \cdot \left(\frac{d\mathbf{z}_{\mathrm{p}}}{d\varphi} \times \mathbf{y}_{\mathrm{p}}\right) + h \cdot \left(\frac{d\mathbf{z}_{\mathrm{p}}}{d\varphi} \times \mathbf{z}_{\mathrm{p}}\right) + \frac{d\mathbf{o}_{\mathrm{p}}}{d\varphi} \times \left(\pm \tan\alpha_{\mathrm{g}} \cdot \mathbf{y}_{\mathrm{p}} + \mathbf{z}_{\mathrm{p}}\right).\end{aligned} \tag{3.42}$$

where

$$\begin{aligned}\frac{d\mathbf{x}_{\mathrm{p}}(\varphi)}{d\varphi} &= \sin\Gamma \cdot \frac{d\theta_{\mathrm{s}}}{d\varphi} \cdot \left[-\sin(\theta_{\mathrm{ms}} + \theta_{\mathrm{s}}) \quad \cos(\theta_{\mathrm{ms}} + \theta_{\mathrm{s}}) \quad 0\right]^T \\ \frac{d\mathbf{y}_{\mathrm{p}}(\varphi)}{d\varphi} &= \frac{d\theta_{\mathrm{s}}}{d\varphi} \cdot \left[\cos(\theta_{\mathrm{ms}} + \theta_{\mathrm{s}}) \quad \sin(\theta_{\mathrm{ms}} + \theta_{\mathrm{s}}) \quad 0\right]^T \\ \frac{d\mathbf{z}_{\mathrm{p}}(\varphi)}{d\varphi} &= \cos\Gamma \cdot \frac{d\theta_{\mathrm{s}}}{d\varphi} \cdot \left[-\sin(\theta_{\mathrm{ms}} + \theta_{\mathrm{s}}) \quad \cos(\theta_{\mathrm{ms}} + \theta_{\mathrm{s}}) \quad 0\right]^T \\ \frac{d\mathbf{o}_{\mathrm{p}}(\varphi)}{d\varphi} &= \frac{d\mathbf{q}_{\mathrm{s}}}{d\varphi} - \tan(\Gamma - \Gamma_{\mathrm{r}}) \cdot \frac{dr_{\mathrm{q}}}{d\varphi} \cdot \mathbf{z}_{\mathrm{p}} - H_{\mathrm{s}} \cdot \frac{d\mathbf{z}_{\mathrm{p}}}{d\varphi}.\end{aligned} \tag{3.43}$$

Both items of $\frac{dr_{\mathrm{q}}}{d\varphi}$ and $\frac{d\theta_{\mathrm{s}}}{d\varphi}$ in Eq. (3.43) are calculated according to Eqs. (3.22) and (3.23) as

$$\begin{aligned}
\frac{dr_{\mathrm{q}}}{d\varphi} &= \frac{r_{\mathrm{c}}}{r_{\mathrm{q}}} \cdot \left[-\mathrm{q_{cx}} \cdot \sin\left(\theta_{\mathrm{mc}} + \theta_{\mathrm{t}} + \varphi\right) + \mathrm{q_{cy}} \cdot \cos\left(\theta_{\mathrm{mc}} + \theta_{\mathrm{t}} + \varphi\right)\right] \\
\frac{d\theta_{\mathrm{s}}}{d\varphi} &= \frac{r_{\mathrm{c}} \cdot \csc\Gamma}{r_{\mathrm{q}}^2} \cdot \left[\mathrm{q_{cx}} \cdot \cos\left(\theta_{\mathrm{mc}} + \theta_{\mathrm{t}} + \varphi\right) + \mathrm{q_{cy}} \cdot \sin\left(\theta_{\mathrm{mc}} + \theta_{\mathrm{t}} + \varphi\right)\right].
\end{aligned} \tag{3.44}$$

According to the result, the normals of the design tooth surface do not collinear along the same rule. The design tooth surface is non-developable ruled surface. Consequently, geometric deviation will be produced while it is manufactured with five-axis flank milling.

Chapter 4

Five-axis flank milling and modeling of spiral bevel gears

4.1 Five-axis flank milling

4.1.1 Flank milling cutter

In five-axis milling, the APT (automatically programmed tools) cutter is a generalized cutter which also can be used to describe other types of milling cutter. As shown in Fig. 4.1, the APT cutter surface is comprised of three parts: lower cone, corner torus and upper cone. To describe the geometry of the APT cutter, five parameters are defined and given as follows:

H, the cutter length measured along the cutter axis;

R_{l}, the radial distance from the corner center to cutter axis;

R_{t}, the radius of the corner torus;

ψ_{l}, the angle between the lower cone and the bottom plane which pass through the cutter tip point $\mathbf{o}_{\mathrm{c}}$ and vertical to the cutter axis;

ψ_u, the taper angle between the upper cone and the cutter axis. Since

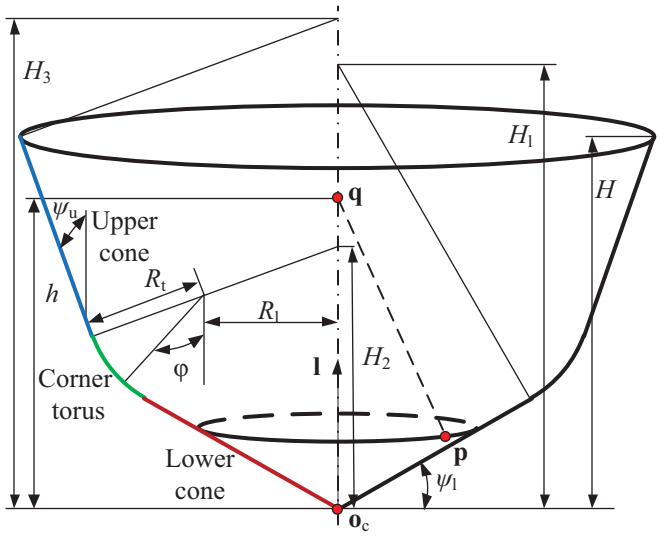

Figure 4.1: The geometry of the APT cutter surface.

the APT cutter surface is a particular case of the specific circular surface, the envelope surface of the APT cutter can be calculated with the geometric envelope approach. To calculate the envelope surface, the preparatory calculations about the effective angle and effective radius are necessary. Since the APT cutter surface is comprised of three parts, we will give the preparatory calculations to each part individually.

For the lower cone, we have

$$\alpha(h) = \pi - \psi_l, \rho(h) = h \cdot \cos\psi_l \tag{4.1}$$

where $0 < h \leq H_1$, and $H_1 = (R_l + R_t \cdot \sin\psi_l) \cdot \sec\psi_l \cdot \csc\psi_l$.

For the corner torus, it is better to use another parameter φ to represent

the generatrix, as shown in Fig. 4.1. We have

$$\alpha(\varphi) = \pi - \varphi, \rho(\varphi) = R_{\mathrm{l}} + R_{\mathrm{t}} \cdot \csc\varphi, h(\varphi) = H_2 + R_{\mathrm{l}} \cdot (\cot\varphi - \tan\psi_{\mathrm{u}}) \quad (4.2)$$

where $\frac{\pi}{2} - \psi_{\mathrm{l}} \leq \varphi \leq \frac{\pi}{2} - \psi_{\mathrm{u}}$ and $H_2 = R_{\mathrm{l}} \cdot (\tan\psi_{\mathrm{l}} + \tan\psi_{\mathrm{u}}) + R_{\mathrm{t}} \cdot \sec\psi_{\mathrm{l}}$.

For the upper cone, the parameter to represent the generatrix is h. We have

$$\alpha(h) = \frac{\pi}{2} + \psi_{\mathrm{u}}, \rho(h) = (R_{\mathrm{l}} + R_{\mathrm{t}}\cos\psi_{\mathrm{u}}) \cdot \sec\psi_{\mathrm{u}} + (h - H_2) \cdot \sin\psi_{\mathrm{u}} \quad (4.3)$$

where

$H_2 \leq h \leq H_3$,

$H_3 = H + \{R_{\mathrm{l}} + R_{\mathrm{t}} \cdot \cos\psi_{\mathrm{u}} + [H - R_{\mathrm{t}} \cdot (\sec\psi_{\mathrm{l}} - \sin\psi_{\mathrm{u}}) - R_{\mathrm{l}} \cdot \tan\psi_{\mathrm{l}}] \cdot \tan\psi_{\mathrm{u}}\} \cdot \tan\psi_{\mathrm{u}}$.

4.1.2 Cutter motion description in five-axis milling

The cutter motion is described in different ways for different stages of the five-axis milling process. At the beginning of the tool path planning stage, the cutter motion is represented as the theoretical tool path, which is generated according to the geometry relationship between the cutter and part. Subsequently, the theoretical tool path is approximated as CL (cutter location) data which records the position and orientation of the cutter at a series of CL points. Moreover, CL data is converted by the post-processor into NC code which is used to a specific CNC machine tool. Finally, the cutter motion can be executed in the practical machining stage by interpolating

two consequent CL points based on the corresponding interpolation scheme and kinematic model of the CNC machine tool. In summary, there are three modes to describe the cutter motion in different stages of the five-axis milling process: theoretical tool path, CL data, NC code. Correspondingly, the cutter motion is obtained as the theoretical cutter motion, CL data cutter motion and NC code cutter motion, respectively. Based on these three cutter motion modes, the envelope surfaces are also varied, and they are referred to in this paper as envelope surface of theoretical tool path, envelope surface of CL data and envelope surface of NC code, respectively. These three cutter motion modes are introduced as follows.

Theoretical cutter motion

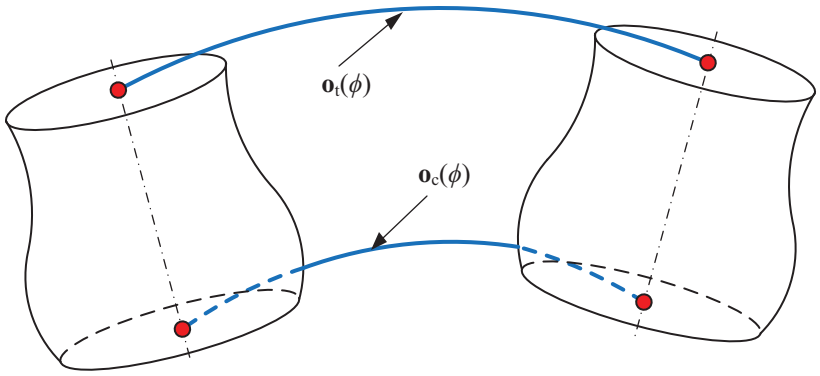

Figure 4.2: Cutter motion described with two curves.

When the cutter is treated as a rigid body, the theoretical cutter motion can be described with two curves, which correspond to the trajectories of two points of the cutter axis. As shown in Fig. 4.2, taking the tip point $\mathbf{o}_c$ and top point $\mathbf{o}_t$ of the cutter axis as the example, the cutter motion are represented

by two curves $\mathbf{o}_{\mathrm{c}}(\phi)$ and $\mathbf{o}_{\mathrm{t}}(\phi)$.With these two curves, we have

$$\mathbf{l}(\phi) = \frac{\mathbf{o}_{\mathrm{t}}(\phi) - \mathbf{o}_{\mathrm{c}}(\phi)}{\mid \mathbf{o}_{\mathrm{t}}(\phi) - \mathbf{o}_{\mathrm{c}}(\phi) \mid} \tag{4.4}$$

$$\mathbf{v}_{\mathrm{q}}(h, \phi) = (1 - h) \cdot \frac{d\mathbf{o}_{\mathrm{c}}(\phi)}{d\phi} + h \cdot \frac{d\mathbf{o}_{\mathrm{t}}(\phi)}{d\phi}. \tag{4.5}$$

When the effective angle and the effective radius are given, the envelope surface of theoretical tool path is obtained by substituting Eqs. (4.4) and (4.5) into Eqs. (2.34) and (2.35). With two curves, the cutter motion can be completely described along the tool path. These two curves can be optimized or corrected to reduce the geometric deviation of the machined surface in five-axis milling [65, 67, 72, 81–83].

CL data cutter motion

When the theoretical tool path is obtained, it will be discretized as a series of CL data, as shown in Fig. 4.3. Before post-processing the CL data into NC code for a five-axis CNC machine tool, it is important to know whether the machining error caused by the discretization is acceptable. Therefore, it is necessary to calculate the envelope surface from the CL data directly. Gong and Wang [71] proposed a method to calculate the envelope surface of a generic cutter directly from CL data. However, this method uses the moving frame. Here we proposed another method which is invariant to the frame. Consequently, the convenient frame can be chosen to simplify the calculation.

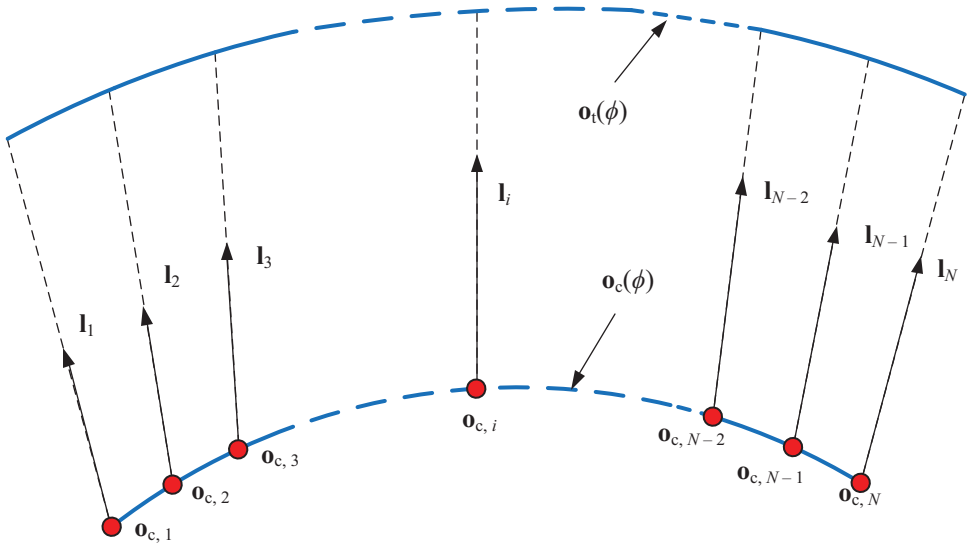

Figure 4.3: Tool path discretized as CL data.

In the CAM system, CL data is the aggregation of vectors $\{\mathbf{o}_{c,i}, \mathbf{l}_i\}, (i = 1 \sim N)$. $\mathbf{o}_{c,i}$ denotes the position of the ith tip point. $\mathbf{l}_i$ indicates the unit vector of the cutter axis corresponding to $\mathbf{o}_{c,i}$. In order to define the cutter motion, the cutter motion between two consecutive CL points needs to be computed.

In five-axis milling, the motion of the tip point is usually a piecewise linear motion. It means the tip point will move along the line connected by two consecutive CL points, as shown in Fig. 4.4. Since the magnitude of the velocity vector does not change the envelope condition, we can assume that the total time of the cutter moving between two consecutive CL points is 1, which means $0 \leq \phi \leq 1$. Then the tip point and its velocity can be represented as

$$\mathbf{o}_{c,i}(\phi) = (1 - \phi) \cdot \mathbf{o}_{c,i} + \phi \cdot \mathbf{o}_{c,i+1} \tag{4.6}$$

$$\mathbf{v}_{\mathrm{o},i}(\phi) = \mathbf{o}_{\mathrm{c},i+1} - \mathbf{o}_{\mathrm{c},i}, 0 \leq \phi \leq 1, i = 1 \sim N-1. \tag{4.7}$$

In Eq. 4.6, $\mathbf{o}_{\mathrm{c},i}(\phi)$ denotes the item $\mathbf{o}_{\mathrm{c}}$ at the instant ϕ during the process of the cutter moving between the ith CL point and the $(i+1)$th CL point. Other similar items can be explained with the same way.

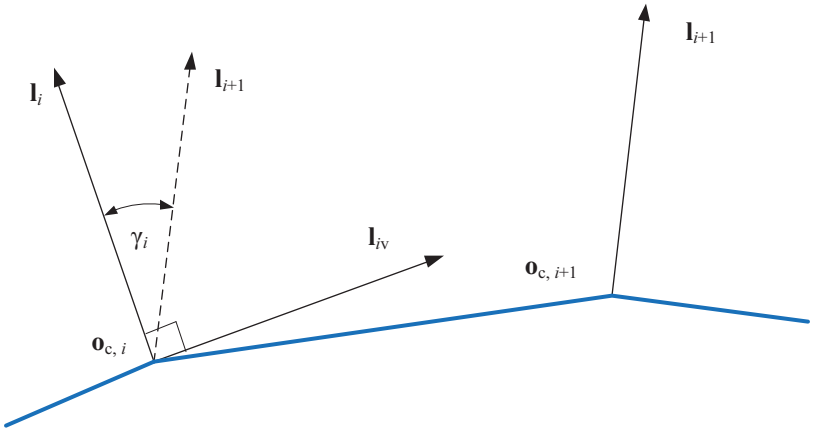

Figure 4.4: Cutter motion between two consecutive CL points.

In order to obtain the cutter axis motion between two consecutive CL points, an additional assumption is necessary. This assumption also introduced by Gong and Wang [71], and it is used to generate the CL data for current CAM systems. The assumption is that the cutter axis is rotate linearly (constant angular velocity) during the cutter moving between two consecutive CL points. As shown in Fig. 4.4, when $\mathbf{l}_{i+1}$ is translated from $\mathbf{o}_{\mathrm{c},i+1}$ to $\mathbf{o}_{\mathrm{c},i}$, the cutter axis motion can be treated as the linear rotation along the axis which pass through $\mathbf{o}_{\mathrm{c}}$ and with direction $\mathbf{l}_i \times \mathbf{l}_{i+1}$. Assume that γ_i is the angle formed by $\mathbf{l}_i$ and $\mathbf{l}_{i+1}$, and $\mathbf{l}_{iv}$ is the a unit vector obtained by rotating

$\mathbf{l}_i$ with angle $\pi/2$. Then we have

$$\sin\gamma_i = \mid \mathbf{l}_i \times \mathbf{l}_{i+1} \mid, \cos\gamma_i = \mathbf{l}_i \cdot \mathbf{l}_{i+1} \tag{4.8}$$

$$\mathbf{l}_{i+1} = \cos\gamma_i \cdot \mathbf{l}_i + \sin\gamma_i \cdot \mathbf{l}_{i\mathrm{v}}. \tag{4.9}$$

According to Eq. (4.9), we have

$$\mathbf{l}_{i\mathrm{v}} = \csc\gamma_i \cdot (-\cos\gamma_i \cdot \mathbf{l}_i + \mathbf{l}_{i+1}). \tag{4.10}$$

The unit vector of the cutter axis during the process of the cutter moving between two consecutive CL points can be expressed as

$$\mathbf{l}_{\phi,i}(\phi) = \cos\phi \cdot \mathbf{l}_i + \sin\phi \cdot \mathbf{l}_{i\mathrm{v}}. \tag{4.11}$$

By substituting Eq. (4.10) into Eq. (4.11), we have

$$\mathbf{l}_{\phi,i}(\phi) = \csc\gamma_i \cdot [\sin(\gamma_i - \phi\cdot\gamma_i) \cdot \mathbf{l}_i + \sin(\phi\cdot\gamma_i) \cdot \mathbf{l}_{i+1}]. \tag{4.12}$$

The velocity of the point on the cutter axis can be calculated as

$$\begin{aligned}\mathbf{v}_{\mathrm{q},i}(h,\phi) &= \mathbf{v}_{\mathrm{o},i}(\phi) + h \cdot \frac{d\mathbf{l}_{\phi,i}(\phi)}{d\phi} \\ &= \mathbf{o}_{\mathrm{c},i+1} - \mathbf{o}_{\mathrm{c},i} + h\cdot\gamma_i\cdot\csc\gamma_i\cdot[-\cos(\gamma_i - \phi\cdot\gamma_i)\cdot\mathbf{l}_i + \cos(\phi\cdot\gamma_i)\cdot\mathbf{l}_{i+1}].\end{aligned} \tag{4.13}$$

When the effective angle and the effective radius are given, the envelope surface of CL data is obtained by substituting Eqs. (4.12) and (4.13) into Eqs. (2.34) and (2.35).

NC code cutter motion

When the CL data is obtained, the post-processor is used to convert the CL data into NC code dedicated for a particular CNC machine tool. Subsequently, the cutter motion in practical machining is determined by implementing the NC code based on the kinematic model and interpolation scheme of the specific CNC machine tool. Therefore, NC code cutter motion is the accurate model of the cutter motion in the practical machining. Depending on the kinematic configurations of the CNC machine tools, the formats of the NC code will be different [84]. Taking an example of a five-axis milling machine with the vertical spindle-rotating configuration, and the combination of the rotary axes CB, then the unit vector of the cutter axis can be expressed as [84]

$$\mathbf{l}_i = [\sin B_i \cdot \cos C_i \;\; \sin B_i \cdot \sin C_i \;\; \cos B_i]^T. \tag{4.14}$$

In current five-axis milling, the cutter configurations corresponding to all CL points can be implemented in high precision. However, the cutter configurations during the process of the cutter moving between two consecutive CL points are depended on the interpolation scheme. Currently, there are two major interpolation schemes in five-axis milling. The first one is the linear interpolation. The motion of each axis is determined by linearly interpolating its values at two consecutive CL points. Consequently, nonlinearity error will be produced due to that the trajectory of the cutter tip point (or cutter center point, cutter contact point) is not a straight line [85,86]. For the other

one, the motion of the rotational axis is determined by linear interpolation, and the motion of the translational axis is implemented with nonlinear interpolation to make the trajectory of the cutter tip point as a straight line [87]. Taking the example of the second interpolation scheme, the cutter tip point trajectory and the cutter axis can be expressed as [87]

$$\mathbf{o}_{\mathrm{c},i}(\phi) = (1-\phi)\cdot\mathbf{o}_{\mathrm{c},i} + \phi\cdot\mathbf{o}_{\mathrm{c},i+1} \tag{4.15}$$

$$\mathbf{l}_{\phi,i}(\phi) = [\sin b_i(\phi)\cdot\cos c_i(\phi)\ \ \sin b_i(\phi)\cdot\sin c_i(\phi)\ \ \cos b_i(\phi)]^T \tag{4.16}$$

where $i = 1 \sim N-1$, $0 \le \phi \le 1$, $b_i(\phi) = (1-\phi)\cdot B_i + \phi\cdot B_{i+1}$, $c_i(\phi) = (1-\phi)\cdot C_i + \phi\cdot C_{i+1}$. According to Eqs. (4.15) and (4.16), the velocity of the point on the cutter axis can be calculated as

$$\begin{aligned}\mathbf{v}_{\mathrm{q},i}(h,\phi) &= \mathbf{v}_{\mathrm{o},i}(\phi) + h\cdot\frac{d\mathbf{l}_{\phi,i}(\phi)}{d\phi} \\ &= \mathbf{o}_{\mathrm{c},i+1} - \mathbf{o}_{\mathrm{c},i} + h\cdot\begin{bmatrix}\Delta B_i\cdot\cos b_i(\phi)\cdot\cos c_i(\phi) - \Delta C_i\cdot\sin b_i(\phi)\cdot\sin c_i(\phi) \\ \Delta B_i\cdot\cos b_i(\phi)\cdot\sin c_i(\phi) + \Delta C_i\cdot\sin b_i(\phi)\cdot\cos c_i(\phi) \\ -\Delta B_i\cdot\sin b_i(\phi)\end{bmatrix}\end{aligned} \tag{4.17}$$

where $\Delta B_i = B_{i+1} - B_i$ and $\Delta C_i = C_{i+1} - C_i$. By substituting Eqs. (4.16) and (4.17) into Eqs. (2.34) and (2.35), the envelope surface of NC code is obtained. As aforementioned, since the NC code cutter motion is the accurate model of cutter motion in practical machining, the envelope surface of NC code is an accurate model to generate the machined surface. The proposed approach is simpler than the method used by Mann et al. [88] due to two reasons. First, since the later method has to calculate the accurate velocity

of the cutter surface point, the kinematic model represented by a series of transformation matrices are inevitable. The other reason is that the grazing point is calculated by numerical method in the later method.

4.1.3 Examples for the calculation of the envelope surface of flank milling cutter

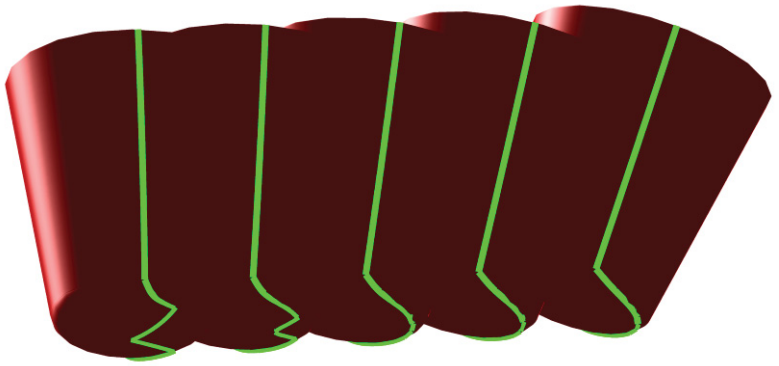

(a) Grazing curves

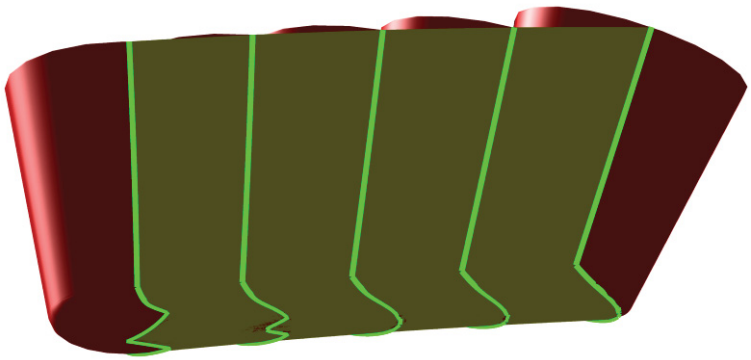

(b) Envelope surface

Figure 4.5: Envelope surface of the APT cutter

With the preparatory calculations, the envelope surface of the milling cutter in five-axis milling can be obtained according to Eqs. (2.34) and (2.35). For example, an APT cutter is given by defining the five parameters $\{H, R_\mathrm{l}, R_\mathrm{t}, \psi_\mathrm{u}, \psi_\mathrm{l}\}$ as $\{45.000, 10.000, 3.000, 10.000°, 10.000°\}$. The cut-

ter motion is described based on the mode of NC code cutter motion, and the NC code data $\{X, Y, Z, B, C\}$ is defined by two CL points with the values $\{0.000, 0.000, 0.000, 0.000°, 0.000°\}$ and $\{50.000, 50.000, 10.000, 18.000°, 18.000°\}$. The computer program is implemented in Matlab language, and the result is shown as Fig. 4.5. This example is also computed with the method proposed by Gong and Wang [71], and the results of both approaches are identical.

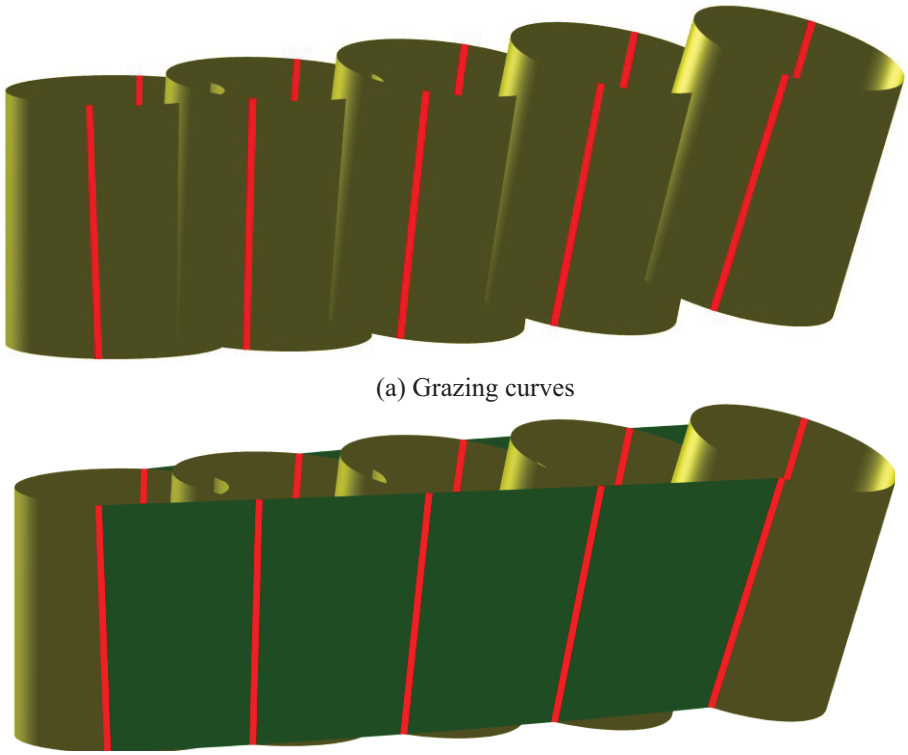

(a) Grazing curves

(b) Envelope surface

Figure 4.6: Envelope surface of the flat-end mill cutter

For the flat end mill, the envelope surface can be obtained according to Eq. (2.38), because the cutter surface of flat-end mill is a cylindrical surface. A flat end mill is introduced to test the proposed method, the parameters of

the flat end mill $\{H, R_{\mathrm{l}}, R_{\mathrm{t}}, \psi_{\mathrm{u}}, \psi_{\mathrm{l}}\}$ are defined as $\{35.000, 15.000, 0.000, 0.000°, 0.000°\}$. The NC code data is defined by two CL points where the values of $\{X, Y, Z, B, C\}$ are $\{0.000, 0.000, 0.000, 0.000°, 0.000°\}$ and $\{60.000, 60.000, 10.000, 18.000°, 27.000°\}$, respectively. The computer program is implemented in Matlab language, and the result is shown as Fig. 4.6. This example is also verified by the method proposed by Gong and Wang [71], and the results are identical.

4.2 Five-axis flank milling spiral bevel gears

4.2.1 The conical cutter for flank milling spiral bevel gears

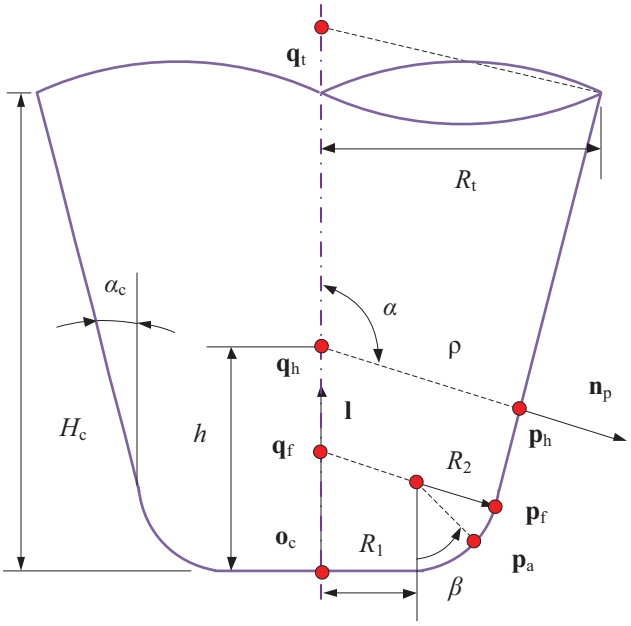

Figure 4.7: The conical cutter for flank milling spiral bevel gears.

Different cutters could be used in flank milling. Here we use conical cutter for five-axis flank milling since it can be also treated as the general cutter

which is used to represent fillet end mill cutters and flat end mill cutters. As shown in Fig. 4.7, the side surface of the conical cutter is composed of two surfaces of revolution, upper and fillet surfaces. They are generated by a straight line with the taper angle α_c and the arc with the radius R_2, respectively. The bottom radius of the conical cutter is R_1. For a point $\mathbf{p}_h$ on the upper surface, we have

$$\mathbf{p}_h(h,\theta) = \mathbf{o}_c + h \cdot \mathbf{l} + \rho(h) \cdot \mathbf{n}_p(h,\theta) \tag{4.18}$$

where $\mid \mathbf{o}_c\mathbf{q}_f \mid \leq h \leq \mid \mathbf{o}_c\mathbf{q}_t \mid$, $0 \leq \theta < 2\pi$, and

$$\begin{aligned} \mid \mathbf{o}_c\mathbf{q}_t \mid &= H_c + R_t \cdot \tan\alpha_c \\ R_t &= R_1 + R_2 \cdot \cos\alpha_c + [H_c - R_2 \cdot (1 - \sin\alpha_c)] \cdot \tan\alpha_c \\ \mid \mathbf{o}_c\mathbf{q}_f \mid &= R_1 \cdot \tan\alpha_c + R_2 \\ \rho(h) &= R_1 \cdot \sec\alpha_c + R_2 + (h - \mid \mathbf{o}_c\mathbf{q}_f \mid) \cdot \sin\alpha_c. \end{aligned} \tag{4.19}$$

For a point $\mathbf{p}_a$ on the fillet surface, we have

$$\mathbf{p}_a(\beta,\theta) = \mathbf{o}_c + h(\beta) \cdot \mathbf{l} + \rho(\beta) \cdot \mathbf{n}_p(\beta,\theta) \tag{4.20}$$

where $0 < \beta < \pi/2 - \alpha_c$, $0 \leq \theta < 2\pi$, and

$$\begin{aligned} h(\beta) &= R_1 \cdot \cot\beta + R_2 \cdot (1 - \sin\alpha_c + \cos\beta) \\ \rho(\beta) &= R_1 \cdot \csc\beta + R_2. \end{aligned} \tag{4.21}$$

Assume that the angle between $\mathbf{n}_p$ and $\mathbf{l}$ is defined as α. For the point on the upper surface, $\alpha = \pi/2 + \alpha_c$. We have

$$\mathbf{n}_p \cdot \mathbf{l} = \cos\alpha. \tag{4.22}$$

4.2.2 Tool path planning strategies

Tooth surface finish machining

Since the design tooth surface is a non-developable ruled surface, geometric deviations will be produced in the tooth surface finish machining with flank milling. Many works have been done to minimize the geometric deviations in flank milling. The details can be referred to [35]. However, different with the works stated in [35], the criteria for spiral bevel gears is the work performance of a pair of them [2–4]. Based on this idea, the tool path planning strategy is given by considering the contact path of the tooth surface.

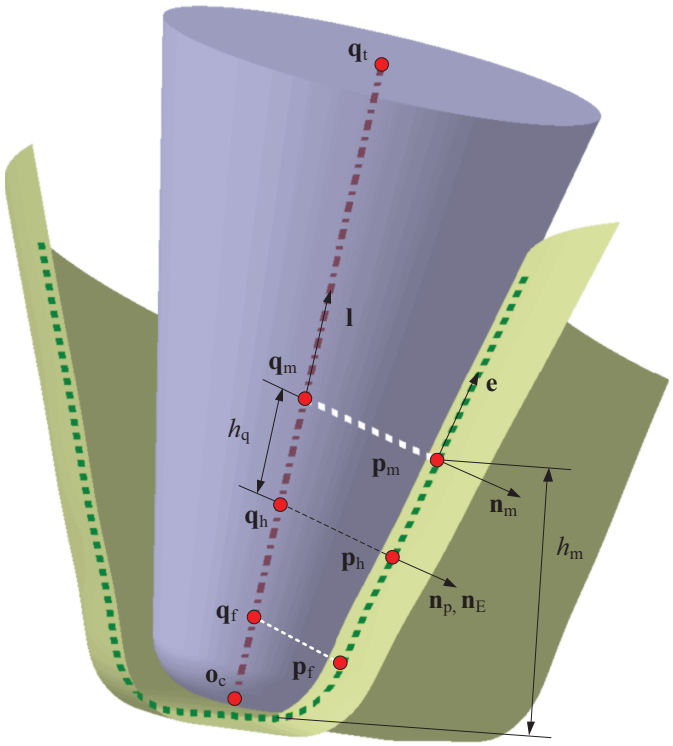

Figure 4.8: Tool path planning strategy for five-axis flank milling tooth surface.

Assuming that $\mathbf{p}_m$ is a point on the contact path of the tooth surface,

$\mathbf{p}_\mathrm{m}$ also is a point lying on the corresponding profile of the tooth surface, as shown in Fig. 4.8. As stated in [2–4], the design contact path is usually chosen as the middle of the tooth surfaces of a pair of spiral bevel gear, of which the parameter h for $\mathbf{p}_\mathrm{m}$ can be obtained as

$$h_\mathrm{m}(\varphi) = \frac{H_\mathrm{p} + c}{2} \tag{4.23}$$

where H_p is calculated in Eq. (3.35); c is the tooth clearance, which is given as a blank design parameter. The detail about the calculation of c can be referred to [78]. Subsequently, the chosen contact paths for both sides of the tooth surface can be obtained by submitting $h = h_\mathrm{m}$ into Eq. (3.40).

The tooth path planning strategy is shown in Fig. 4.8. $\mathbf{n}_\mathrm{m}$ is the unit normal of the tooth surface at $\mathbf{p}_\mathrm{m}$. $\mathbf{e}$ is the unit direction of straight line part of the profile. The cutter axis $\mathbf{l}$ and cutter tip point $\mathbf{o}_\mathrm{c}$ are determined according to the following conditions.

(1) The cutter surface is tangent to the tooth surface at point $\mathbf{p}_\mathrm{m}$. The corresponding tangent point on the cutter surface is $\mathbf{p}_\mathrm{m}$.

(2) $\mathbf{l}$ lies on the profile plane, which is determined by $\mathbf{n}_\mathrm{m}$ and $\mathbf{e}$.

(3) $\mathbf{p}_\mathrm{f}$, which is the intersection point of straight line part and the fillet part of the tooth surface profile, is also the intersection point of straight line part and the fillet part of the cutter surface profile.

With the above three conditions, the tool path can be calculated as follows. First, $\mathbf{p}_\mathrm{m}$ and its unit normal can be obtained in S_g by submitting $h = h_\mathrm{m}$

into Eqs. (3.40) and (3.41) respectively. We have

$$\begin{aligned}[\mathbf{p}_{\mathrm{m,g}}(\varphi) \quad 1] &= \left[\mathbf{r}_{\mathrm{l,p}}(h)\Big|_{h=h_{\mathrm{m}}(\varphi)} \quad 1\right] \cdot \mathbf{M}_{\mathrm{gp}}(\varphi) \\ \mathbf{n}_{\mathrm{m,g}}(\varphi) &= \mathbf{n}_{\mathrm{g}}(\varphi, h)\Big|_{h=h_{\mathrm{m}}(\varphi)}.\end{aligned} \tag{4.24}$$

Second, $\mathbf{e}$ can be obtained in S_{g} as

$$[\mathbf{e}_{\mathrm{g}}(\varphi) \quad 0] = [\mathbf{e}_{\mathrm{p}} \quad 0] \cdot \mathbf{M}_{\mathrm{gp}}(\varphi) = [0 \quad \pm\sin\alpha_g \quad \cos\alpha_g \quad 0] \cdot \mathbf{M}_{\mathrm{gp}}(\varphi). \tag{4.25}$$

Finally, $\mathbf{l}$ and $\mathbf{o}_{\mathrm{c}}$ are obtained in S_{g} as

$$\begin{aligned}\mathbf{l}_{\mathrm{g}}(\varphi) &= \mathbf{e}_{\mathrm{g}}(\varphi) \cdot \cos\alpha_{\mathrm{c}} - \mathbf{n}_{\mathrm{m,g}}(\varphi) \cdot \sin\alpha_{\mathrm{c}} \\ \mathbf{o}_{\mathrm{c,g}}(\varphi) &= \mathbf{q}_{\mathrm{m,g}} - \mid \mathbf{q}_{\mathrm{m}}\mathbf{p}_{\mathrm{m}} \mid \cdot\mathbf{n}_{\mathrm{m,g}} - \mid \mathbf{q}_{\mathrm{m}}\mathbf{o}_{\mathrm{c}} \mid \cdot\mathbf{l}_{\mathrm{g}}.\end{aligned} \tag{4.26}$$

where $\mid \mathbf{q}_{\mathrm{m}}\mathbf{p}_{\mathrm{m}} \mid$ and $\mid \mathbf{q}_{\mathrm{m}}\mathbf{o}_{\mathrm{c}} \mid$ are calculated as follows.

$$\begin{aligned}\mid \mathbf{p}_{\mathrm{m}}\mathbf{p}_{\mathrm{f}} \mid &= (h_{\mathrm{m}} - \mathrm{p}_{\mathrm{fz}}) \cdot \sec\alpha_{\mathrm{g}} \\ \mid \mathbf{q}_{\mathrm{m}}\mathbf{o}_{\mathrm{c}} \mid &= \mid \mathbf{p}_{\mathrm{m}}\mathbf{p}_{\mathrm{f}} \mid \cdot \sec\alpha_{\mathrm{c}} + R_1 \cdot \tan\alpha_{\mathrm{c}} + R_2 \\ \mid \mathbf{o}_{\mathrm{m}}\mathbf{p}_{\mathrm{m}} \mid &= R_1 \cdot \sec\alpha_{\mathrm{c}} + R_2 + \mid \mathbf{p}_{\mathrm{m}}\mathbf{p}_{\mathrm{f}} \mid \cdot \tan\alpha_{\mathrm{c}}.\end{aligned} \tag{4.27}$$

Subsequently, the tooth paths are obtained. For the previous example stated in Table 3.7, the manufacturing cutter data is shown in Table 4.1. The generated tool paths for a tooth slot are obtained and implemented in CATIA V5R20 as shown in Fig. 4.9.

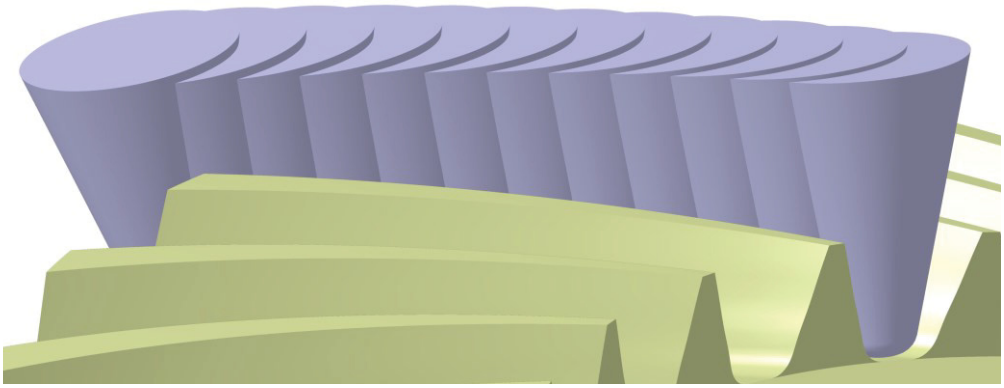

(a) Tool path for convex tooth surface

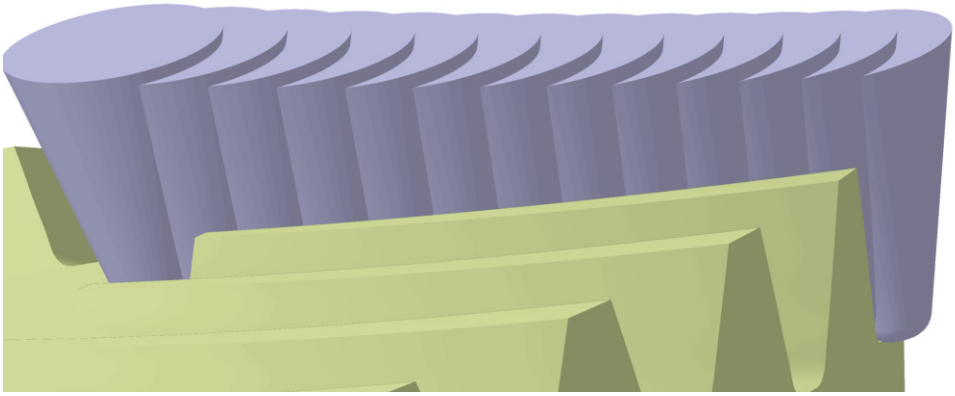

(b) Tool path for concave tooth surface

Figure 4.9: Tool paths planned for one tooth slot.

Table 4.1: Manufacturing data of the spiral bevel gear

Parameter	Value
cutter radius	1.0000 mm
cutter taper angle	15.0000°
cutter fillet radius	1.5000 mm

Rough machining

Since we have the 3D model of the spiral bevel gears, the rough machining tool path can be easily obtained in commercial CAM (Computer-aided Manufacturing) softwares, such CATIA, UG, Msstercam, PowerMILL, etc. With the help of these CAM softwares, the tool path for rough machining each side of every tooth slot can be generated individually. However, it could be more efficient to machining both sides of every slot with one tool path due to the fact that the profiles of booth tooth surface are symmetrical along the lengthwise curve. Hence, it is necessary to introduce the corresponding tool path planing strategy. Two strategies are applied, as shown in Figs. 4.10 and 4.11, respectively. The tool paths are planned along the lengthwise curve.

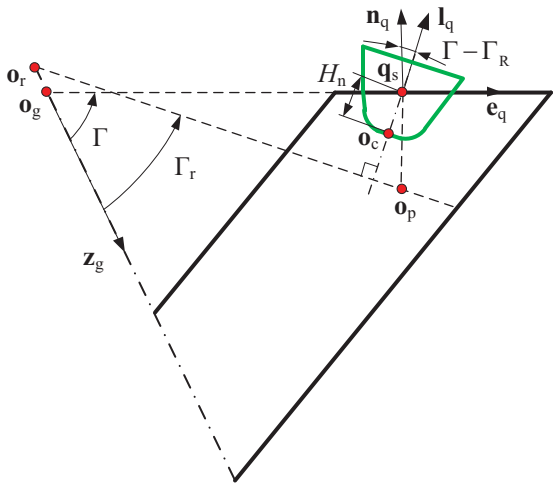

Figure 4.10: Tool path planning strategy I for five-axis roughing.

For case I, taking an arbitrary point $\mathbf{p}_s$, the tool axis is located in the plane formed by $\mathbf{n}_q$ and $\mathbf{e}_q$. The angle between $\mathbf{n}_q$ and $\mathbf{l}_q$ is $\Gamma - \Gamma_R$. The tool tip point is determined by the tool axis and H_n, which is distance of the tool tip

point $\mathbf{o}_\mathrm{c}$ to $\mathbf{q}_\mathrm{s}$. Since it usually takes more than one pass to do roughing for each tooth slot, H_n will be changed. And H_n means the distance at the n^{th} pass. Consequently, the tool axis and tool tip point can be calculated in S_p, which has been stated in Section 3.2.3. Then we have

$$\begin{aligned}\mathbf{l}_{\mathrm{q,p}} &= \begin{bmatrix}\sin(\Gamma-\Gamma_\mathrm{r}) & 0 & \cos(\Gamma-\Gamma_\mathrm{r})\end{bmatrix}^T \\ \mathbf{o}_{\mathrm{c,p}} &= \mathbf{p}_{\mathrm{s,p}} + (H_\mathrm{s}\cdot\sin(\Gamma-\Gamma_\mathrm{r}) - H_\mathrm{n})\cdot\begin{bmatrix}-\cos(\Gamma-\Gamma_\mathrm{r}) & 0 & \sin(\Gamma-\Gamma_\mathrm{r})^T\end{bmatrix}.\end{aligned} \tag{4.28}$$

For case II, the tool axis is always along $\mathbf{n}_\mathrm{q}$. Subsequently, the tool tip point also lies on the $\mathbf{p}_\mathrm{s}\mathbf{o}_\mathrm{q}$. Correspondingly, we have the tool axis and tool tip point in S_p as

$$\begin{aligned}\mathbf{l}_{\mathrm{q,p}} = \mathbf{n}_{\mathrm{q,p}} &= \begin{bmatrix}0 & 0 & 1\end{bmatrix}^T \\ \mathbf{o}_{\mathrm{c,p}} &= \mathbf{q}_{\mathrm{s,p}} - H_\mathrm{n}\cdot\begin{bmatrix}0 & 0 & 1\end{bmatrix}^T.\end{aligned} \tag{4.29}$$

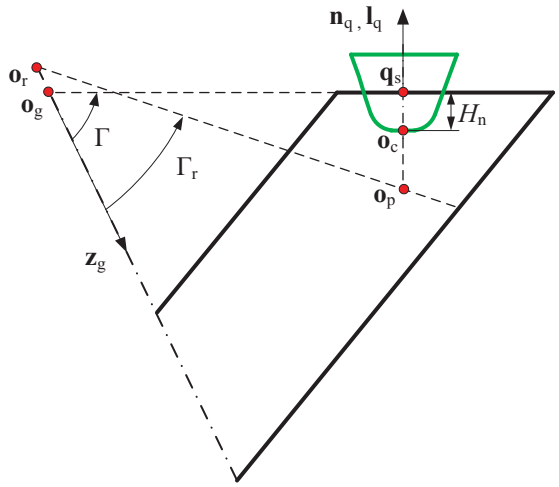

Figure 4.11: Tool path planning strategy II for five-axis roughing.

Interference

Interference are also an important consideration in five-axis tool path planning. Here we takes a simple example for roughing strategy II with a fillet end mill cutter. As shown in Fig. 4.12 (a), the interference are happened at the fillet part of the end mill cutter. The critical case is shown in Fig. 4.12 (b). In order to avoid interference in five-axis flank milling spiral bevel gears, the comprehensive detection should be conducted with the whole 3D models. More details about it can be investigated based on the works of interference in five-axis CNC machining.

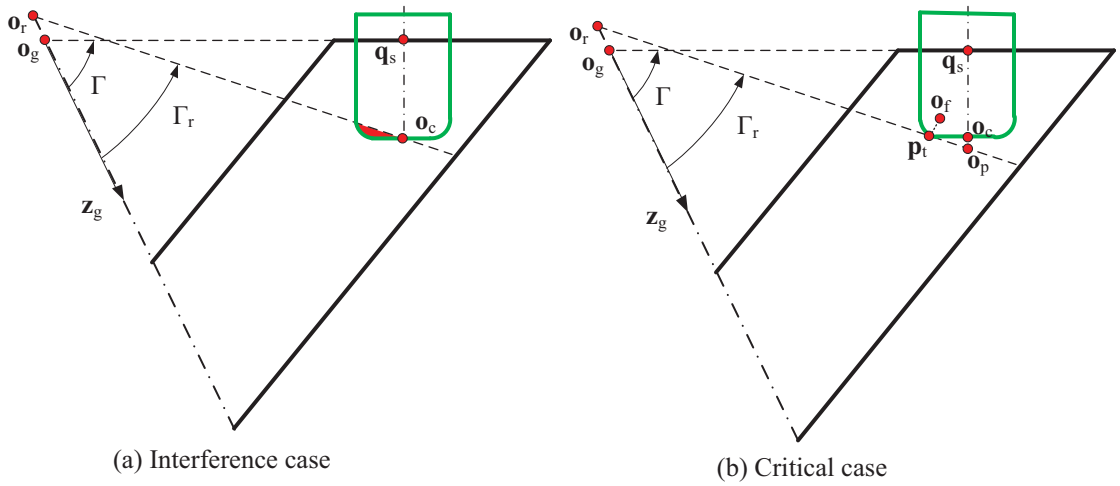

Figure 4.12: The interference in five-axis flank milling spiral bevel gears.

4.3 Closed-form representation of the simulate machined tooth surface

The tooth surface model is the fundamental input to evaluate the work performance of a pair of spiral bevel gears, such as the contact path and

transmission errors. With the considerations of time and cost, the simulate tooth surface model is usually applied before real machining. The simulate machined tooth surface is part of the envelope surface of the flank milling cutter moving along the tool path of the finish machining. Hence, to obtain the simulate machined tooth surface, the envelope surface is calculated first, and then it is used to trimmed the blank to obtain the final tooth surface.

As aforementioned, the envelope surface of the flank milling cutter can be calculated with geometric envelope approach as a closed-from representation. For a given point $\mathbf{p}_{\mathrm{h}}$, as shown in Fig. 4.8, $\mathbf{n}_{\mathrm{p}}$ is the unit normal of the cutter surface at $\mathbf{p}_{\mathrm{h}}$. If $\mathbf{p}_{\mathrm{h}}$ is the grazing point, $\mathbf{n}_{\mathrm{q}}$ can be calculated by the geometric envelope approach as a closed-form result. Since $\mathbf{p}_{\mathrm{h}}$ is the grazing point, $\mathbf{n}_{\mathrm{q}}$ is also the normal of the envelope surface at $\mathbf{p}_{\mathrm{h}}$. Here we use $\mathbf{n}_{\mathrm{E}}$ to represent the normal of the envelope surface. According to Eq. (2.35), the closed-form expression of $\mathbf{n}_{\mathrm{E}}$ can be expressed as

$$\mathbf{n}_{\mathrm{E}} = \frac{\cos\alpha \cdot \mathbf{v}_q^2}{(\mathbf{l} \times \mathbf{v}_q)^2} \cdot \mathbf{l} - \frac{(\mathbf{l} \cdot \mathbf{v}_q) \cdot \cos\alpha}{(\mathbf{l} \times \mathbf{v}_q)^2} \cdot \mathbf{v}_q \pm \frac{\sqrt{(\mathbf{l} \times \mathbf{v}_q)^2 - \cos^2\alpha \cdot \mathbf{v}_q^2}}{(\mathbf{l} \times \mathbf{v}_q)^2} \cdot (\mathbf{l} \times \mathbf{v}_q)\,. \tag{4.30}$$

Subsequently, the closed-form expression of the envelope surface can be obtained according to Eq. (2.34) as

$$\mathbf{s}(h,\phi) = \mathbf{o}_{\mathrm{c}}(\phi) + h \cdot \mathbf{l}(\phi) + \rho(h) \cdot \mathbf{n}_{\mathrm{E}}(h,\phi) = \mathbf{q}_{\mathrm{h}}(\phi) + \rho(h) \cdot \mathbf{n}_{\mathrm{E}}(h,\phi) \tag{4.31}$$

With the geometric envelope approach, the cutter envelope surface can be obtained by calculating all the items in Eqs. (4.30) and (4.31). $\mathbf{l}$ and $\mathbf{o}_{\mathrm{c}}$ have been calculated in Eqs. (4.26). The other terms are calculated as follows.

For the upper surface, h_{q} is used to replace the parameter h in the geometric envelope approach. As shown in Fig. 4.8, h_{q} is the distance from $\mathbf{q}_{\mathrm{m}}$ to $\mathbf{q}_{\mathrm{h}}$. h_{q} is positive when the direction of $\mathbf{q}_{\mathrm{m}}\mathbf{q}_{\mathrm{h}}$ is the same with $\mathbf{l}$, or it is negative. The angle between $\mathbf{n}_{\mathrm{E}}$ and $\mathbf{l}$ is obtained as $\alpha = \alpha_{\mathrm{c}} + \pi/2$. $\rho(h_{\mathrm{q}})$ is the distance between $\mathbf{p}_h$ and $\mathbf{q}_h$. Then we have

$$\begin{aligned} \mathbf{q}_h(\varphi, h_{\mathrm{q}}) &= \mathbf{p}_{\mathrm{m}} - \mid \mathbf{q}_{\mathrm{m}}\mathbf{p}_{\mathrm{m}} \mid \cdot \mathbf{n}_{\mathrm{m}} + h_{\mathrm{q}} \cdot \mathbf{l} \\ \rho(h_{\mathrm{q}}) &= \mid \mathbf{q}_{\mathrm{m}}\mathbf{p}_{\mathrm{m}} \mid + h_{\mathrm{q}} \cdot \sin\alpha_{\mathrm{c}} \end{aligned} \tag{4.32}$$

where

$$\begin{aligned} -\mid \mathbf{q}_{\mathrm{m}}\mathbf{q}_{\mathrm{f}} \mid \leq h_{\mathrm{q}} \leq \mid \mathbf{q}_{\mathrm{m}}\mathbf{q}_{\mathrm{t}} \mid, \\ \mid \mathbf{q}_{\mathrm{m}}\mathbf{q}_{\mathrm{t}} \mid = \mid \mathbf{o}_{\mathrm{c}}\mathbf{q}_{\mathrm{t}} \mid - \mid \mathbf{q}_{\mathrm{m}}\mathbf{o}_{\mathrm{c}} \mid . \end{aligned}$$

According to Eq. (4.32), $\mathbf{v}_q$ is obtained as the velocity of $\mathbf{q}_h$ as

$$\mathbf{v}_q(\varphi, h_{\mathrm{q}}) = \frac{d\mathbf{p}_{\mathrm{m}}}{d\varphi} - \frac{d \mid \mathbf{q}_{\mathrm{m}}\mathbf{p}_{\mathrm{m}} \mid}{d\varphi} \cdot \mathbf{n}_{\mathrm{m}} - \mid \mathbf{q}_{\mathrm{m}}\mathbf{p}_{\mathrm{m}} \mid \cdot \frac{d\mathbf{n}_{\mathrm{m}}}{d\varphi} + h_{\mathrm{q}} \cdot \frac{d\mathbf{l}}{d\varphi} \tag{4.33}$$

where in S_{g} we have

$$\begin{aligned} &\frac{d\mathbf{p}_{\mathrm{m,g}}}{d\varphi} = \mathbf{N}_{\varphi,\mathrm{g}}(\varphi, h_{\mathrm{m}}) + \frac{dh_{\mathrm{m}}}{d\varphi} \cdot (\pm \tan\alpha_{\mathrm{g}} \cdot \mathbf{y}_{\mathrm{p}} + \mathbf{z}_{\mathrm{p}}) \\ &\frac{dh_{\mathrm{m}}}{d\varphi} = \frac{dr_{\mathrm{q}}}{d\varphi} \cdot \frac{\tan(\Gamma - \Gamma_{\mathrm{r}}) + \tan(\Gamma_{\mathrm{o}} - \Gamma)}{2} \\ &\frac{d \mid \mathbf{q}_{\mathrm{m}}\mathbf{p}_{\mathrm{m}} \mid}{d\varphi} = \tan\alpha_{\mathrm{c}} \cdot \sec\alpha_{\mathrm{g}} \cdot \frac{dh_{\mathrm{m}}}{d\varphi} \\ &\frac{d\mathbf{l}_{\mathrm{g}}(\varphi)}{d\varphi} = \cos\alpha_{\mathrm{c}} \cdot \left(\pm \sin\alpha_{\mathrm{g}} \cdot \frac{d\mathbf{y}_{\mathrm{p}}(\varphi)}{d\varphi} + \cos\alpha_{\mathrm{g}} \cdot \frac{d\mathbf{z}_{\mathrm{p}}(\varphi)}{d\varphi} \right) - \sin\alpha_{\mathrm{c}} \cdot \frac{d\mathbf{n}_{\mathrm{m,g}}(\varphi)}{d\varphi}. \end{aligned} \tag{4.34}$$

$\frac{d\mathbf{n}_{\mathrm{m}}}{d\varphi}$ is calculated in S_{g} as shown in Appendix B.

For the fillet surface, β is used to replace the parameter h in the geometric

meshing theory. h and ρ are the functions with respect to β and they are already calculated in Eq. (4.21). Then we have

$$\mathbf{q}_h(\varphi,\beta) = \mathbf{p}_{\mathrm{m}} - \mid \mathbf{o}_{\mathrm{m}}\mathbf{p}_{\mathrm{m}} \mid \cdot\mathbf{n}_{\mathrm{m}} + (h(\beta) - \mid \mathbf{o}_{\mathrm{m}}\mathbf{o}_{\mathrm{c}} \mid) \cdot \mathbf{l}. \tag{4.35}$$

$\mathbf{v}_q$ is obtained as the derivative of $\mathbf{q}_h$ with respect to φ as

$$\begin{aligned}\mathbf{v}_q(\varphi, h_{\mathrm{q}}) =& \frac{d\mathbf{p}_{\mathrm{m}}}{d\varphi} - \frac{d \mid \mathbf{q}_{\mathrm{m}}\mathbf{p}_{\mathrm{m}} \mid}{d\varphi} \cdot \mathbf{n}_{\mathrm{m}} - \mid \mathbf{q}_{\mathrm{m}}\mathbf{p}_{\mathrm{m}} \mid \cdot \frac{d\mathbf{n}_{\mathrm{m}}}{d\varphi} \\ &+ (h(\beta) - \mid \mathbf{q}_{\mathrm{m}}\mathbf{o}_{\mathrm{c}} \mid) \cdot \frac{d\mathbf{l}}{d\varphi} + \frac{d \mid \mathbf{q}_{\mathrm{m}}\mathbf{o}_{\mathrm{c}} \mid}{d\varphi} \cdot \mathbf{l}.\end{aligned} \tag{4.36}$$

where

$$\frac{d \mid \mathbf{q}_{\mathrm{m}}\mathbf{o}_{\mathrm{c}} \mid}{d\varphi} = \sec\alpha_{\mathrm{c}} \cdot \sec\alpha_{\mathrm{g}} \cdot \frac{dh_{\mathrm{m}}}{d\varphi} \tag{4.37}$$

Subsequently, the envelope surface generated by the cutter surface can be obtained. For the previous example stated in Table 4.1, the envelope surfaces of the upper cutter surface for flank milling the convex and concave tooth surfaces, respectively, are obtained as shown in Fig. 4.13. Consequently, the 3D gear model with simulate machined tooth surfaces are obtained in CATIA V5R20, as shown in Fig. 4.14.

4.4 Geometric deviation analysis and comparison

4.4.1 The geometric deviation analysis

Since both the design and simulate machined tooth surfaces are obtained, the comparison can be implemented. The geometric deviation analysis is given for the tooth profiles of both tooth surfaces on the plane Π_{M}. As shown

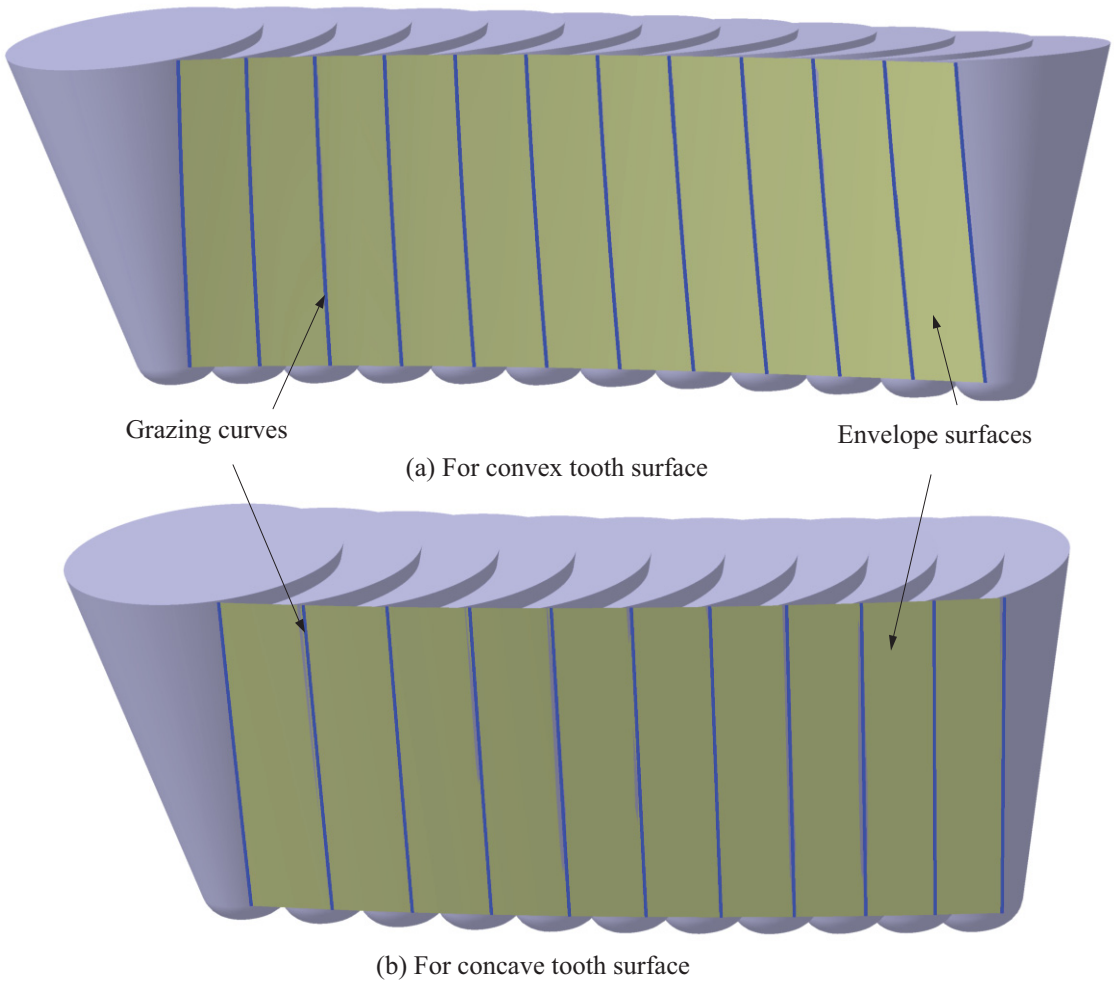

Figure 4.13: The envelope surface of the upper cutter surface for flanking a tooth slot.

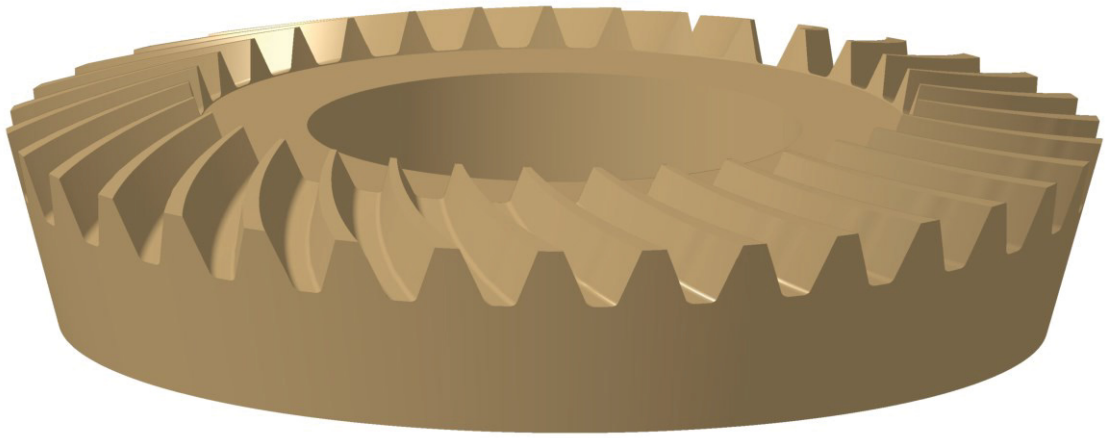

Figure 4.14: 3D gear model with simulate machined tooth surfaces.

in Fig. 4.15, Π_M passes through the mean point $\mathbf{M}$ and is perpendicular to radial direction $\mathbf{o}_g\mathbf{M}$. The result is obtained from CATIA V5R20, as shown in Fig. 4.16. Moreover, several sample points are used to check the geometric deviations. These sample points are chosen as the intersection points of tooth profiles and several lines. L_0 is chosen to pass the contact points. The distances of L_1, L_3 and L_5 above L_0 are 0.5 mm, 1.5 mm and 3.0 mm, respectively. The distances of L_2, L_4 and L_6 below L_0 are 0.5 mm, 1.5 mm and 3.0 mm, respectively. The geometric deviations at the chosen points are shown in Table 4.2.

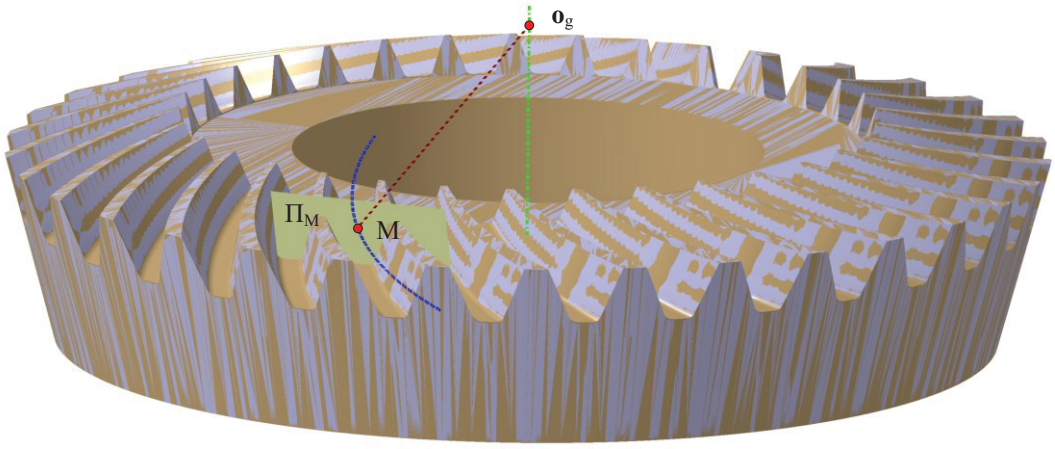

Figure 4.15: The profiles for comparing the geometric deviation.

Compared with the design tooth profile, the machined tooth profile is overcut. The overcut could be explained with the tooth path planning strategy. At a given CL point, the cutter is planned tangent to the design profile. Since the removed material will be more than the cutter shape at this CL point, the overcut is generated. Also the geometric deviation is bigger when the distance to the contact point is farther. According to the results, the geometric deviations are very small. Especially for the area near the contact point, it

only around 1 μm. It satisfies most critical quality requirements.

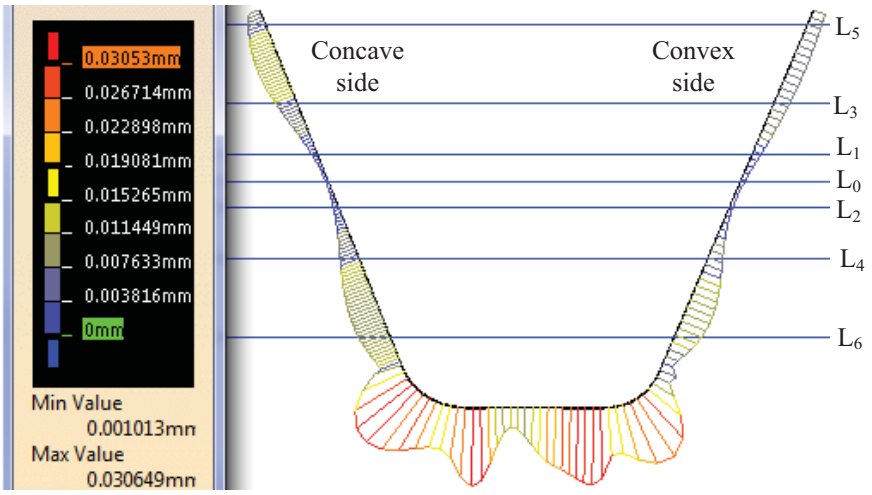

Figure 4.16: Geometric deviation analysis for the proposed design.

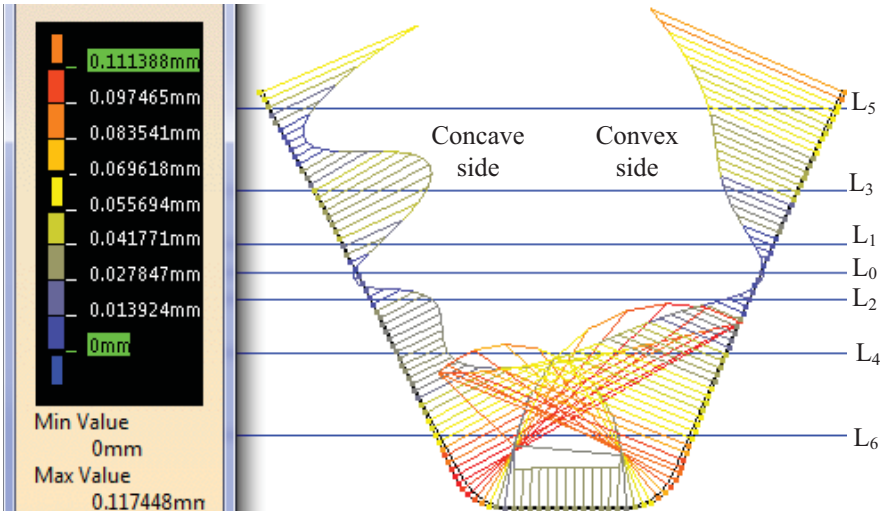

Figure 4.17: Geometric deviation analysis for the face-milled model.

4.4.2 Comparison with the generated face-milled tooth surface model

As a comparison, the generated face-milled tooth surface model, which is obtained from the conventional generated face-milled method, is also used to

do flank milling. The blank data of the generated face-milled tooth surface model is the same blank data in Table 3.7. The manufacturing data and calculation details can be referred to [77]. With this tooth surface model, the tool path planning strategy is also the same as the example of the proposed model. Subsequently, the corresponding geometrical deviations are also obtained in Fig. 4.17 and Table 4.2. According to the results, the areas around the contact points are overcut, but the other areas are undercut. The overcut can be explained as the same as Fig. 4.16. The reason of the undercut is that both sides of the profile of the face-milled tooth surface are convex shapes.

Compared to the generated face-milled model, the proposed model reduces the geometric deviations effectively. Moreover, another advantage of the proposed approach is that the tooth surface model is obtained as the closed-form representation, which is easier and more efficient for the further calculations [77]. On the contrary, numerical model is obtained from the generated face-milled model. To calculate the design contact path of the generated face-milled model, the numerical method is used as stated as Eqs. (3.2.1) and (3.2.1) in [4] or Eq. (21.5.4) in [2]. Subsequently, the simulate machined tooth surface is obtained by solving more complicated implicit equations with numerical methods.

Table 4.2: Geometric deviations at chosen points (μm)[I]

		L_0	L_1	L_2	L_3	L_4	L_5	L_6
Proposed model	Convex side	1.2	2.7	1.5	5.5	5.8	5.3	9.6
	Concave side	1.0	1.8	2.1	7.4	7.6	6.8	10.8
Conventional model	Convex side	1.2	−9.3	−4.2	−31.7	−30.3	−67.5	−69.0
	Concave side	1.1	−23.8	−7.8	−28.8	−18.3	−35.4	−66.8

I: Positive and negative mean overcut and undercut, respectively.

Chapter 5

Conclusion and future works

5.1 Conclusion

Based on industry demands, five-axis flanking milling is studied in this thesis to cut spiral bevel gear. A new ruled tooth surface is proposed to design spiral bevel gears. Subsequently, the design model is used to do tool path planning with a new tool path planning approach. Furthermore, the simulate machined tooth surface is computed as part of the envelope surface, which is formed by the flank milling cutter moving along the planned tool path. Consequently, the geometric deviation is obtained by comparing the design and simulate machined result. The result of the geometric deviation shows that the proposed flank milling approach is appropriate to the spiral bevel gear manufacturing. Moreover, the further comparison between the proposed model and the conventional face-milled model also shows the priority of the proposed model in five-axis flank milling spiral bevel gears. Several distinct works in this thesis are summarized as follows.

(1) A new geometric envelope approach is proposed to calculate the envelope surface as a closed-form vector representation. The calculation of envelope surface is a significant work in the fields of gear manufacturing and CNC machining. Comparing to the other methods, the geometric envelope approach has several distinct features to make its calculation more efficient and straightforward. First, the result is directly obtained as a closed-form representation with respect to two parameters. One is related to the shape of the cutter (or generating surface) and the other is related to the motion of the cutter. Second, since the expression is a vector form, a convenient coordinate system can be chosen for the further calculation. Third, the curvature of the envelope surface can be calculated according to the differential geometry knowledge. The new geometric envelope approach is more efficient than the previous methods to calculate the envelope surface and its curvature.

(2) A new ruled tooth surface design is proposed to five-axis flank milling spiral bevel gears. Although the current tooth surface models are closed to the ruled surface, there is no ruled tooth surface design available. Hence, the proposed ruled tooth surface design give a useful example to design the tooth surface, especially for five-axis flank milling.

(3) The tool path planning of five-axis flank milling spiral bevel gears is conducted according to characteristic of the tooth action of a pair of spiral bevel gears. Different to other parts machined by five-axis flank milling, the tooth surfaces are manufactured to be engaged as a pair. Therefore, the proposed tool path planning strategy gives a good example to apply the well-established knowledge of five-axis flank milling to cut spiral bevel gears.

5.2 Future works

The final goal of the design and manufacturing spiral bevel gears is about their work performances. Lots of works have been done in conventional approaches to improve the work performances. Since five-axis flank milling is still a new topic to spiral bevel gears, the similar works as the conventional approaches also should be done for five-axis flank milling. Moreover, there are many works, which has been done in five-axis flank milling other parts, also need to be investigated to conduct properly for cutting spiral bevel gears. Here, a summarization of the future works for flank milling spiral bevel gears is stated as the following aspects.

(1) The applications of five-axis flank milling to spiral bevel gears

Although five-axis flank milling has been well-established to machine some parts, it is not yet for spiral bevel gears. Subsequently, many investigations need to be applied to spiral bevel gears, such as tool path planning strategies for different machining processes (the major concern of this thesis is about the strategy for tooth surface finish machining), machining error control, tool interference, machining efficiency.

(2) Other design models

Since any reasonable shapes can be chosen for the length curve and the profile, other design models may be applied to improve the work performances of the flank milling spiral bevel gears. Moreover, the tooth flank modification could also be a useful tool to improve work performances.

(3) Pinion design and manufacturing

With the given machined gear model, the pinion could be designed and manufactured to conjugate with the gear. It is challenging to find the reasonable design and manufacturing for pinion.

(4) Work performance analysis and optimization

It is usually an iteration process for designing and manufacturing spiral bevel gears to satisfy their work performances, such as contact path localization, bearing stress and transmission errors. The work performance analysis and optimization is significant for five-axis flank milling spiral bevel gears.

5.3 Publications related to the thesis

[1] Yuansheng Zhou, Zezhong Chevy Chen. A new geometric meshing theory for a closed-form vector representation of the face-milled generated gear tooth surface and its curvature analysis. Mechanism and Machine Theory, 2015, 83 (1), 91-108.

[2] Yuansheng Zhou, Zezhong Chevy Chen, Xujing Yang. An accurate, efficient envelope approach to modeling the geometric deviation of the machined surface for a specific five-axis CNC machine tool. International Journal of Machine Tools and Manufacture, 2015, 95, 67-77.

[3] Yuansheng Zhou, Zezhong Chevy Chen. Five-axis flank milling and modeling the spiral bevel gear with a ruled tooth surface design. Journal of Manufacturing Science and Engineering, Under review.

Bibliography

[1] H. J. Stadtfeld, "Face hobbing-lapping or face milling-grindinga question of application and environment?," *The Gleason Works*, 2006.

[2] F. L. Litvin and A. Fuentes, *Gear geometry and applied theory*. Cambridge University Press, 2004.

[3] F. L. Litvin, *Theory of gearing*. AVSCOM technical report, National Aeronautics and Space Administration, Scientific and Technical Information Division, 1989.

[4] F. L. Litvin and Y. Zhang, "Local synthesis and tooth contact analysis of face-milled spiral bevel gears," tech. rep., DTIC Document, 1991.

[5] F. L. Litvin, N. X. Chen, and J. S. Chen, "Computerized determination of curvature relations and contact ellipse for conjugate surfaces," *Computer Methods in Applied Mechanics and Engineering*, vol. 125, no. 1, pp. 151–170, 1995.

[6] P. H. Feng, D. P. Townsend, R. F. Handschuh, and F. L. Litvin, "Determination of principal curvatures and contact ellipse for profile crowned

helical gears," *Journal of Mechanical Design*, vol. 121, no. 1, pp. 107–111, 1999.

[7] A. N. Pressley, *Elementary differential geometry*. Springer, 2010.

[8] Z. H. Fong and C. B. Tsay, "A mathematical model for the tooth geometry of circular-cut spiral bevel gears," *Journal of Mechanical Design*, vol. 113, no. 2, pp. 174–181, 1991.

[9] C. B. Tsay and J. Y. Lin, "A mathematical model for the tooth geometry of hypoid gears," *Mathematical and Computer Modelling*, vol. 18, no. 2, pp. 23 – 34, 1993.

[10] Y. P. Shih, G. C. Lin, and Z. H. Fong, "Mathematical model for a universal face hobbing hypoid gear generator," *Journal of Mechanical Design*, vol. 129, no. 1, pp. 38–47, 2007.

[11] M. Lelkes, D. Play, and J. Ma?rialigeti, "Numerical determination of cutting parameters for the control of klingelnberg spiral bevel gear geometry," *Journal of Mechanical Design*, vol. 124, no. 4, pp. 761–771, 2002.

[12] Q. Fan, "Computerized modeling and simulation of spiral bevel and hypoid gears manufactured by gleason face hobbing process," *Journal of Mechanical Design*, vol. 128, no. 6, pp. 1315–1327, 2006.

[13] M. Vimercati, "Mathematical model for tooth surfaces representation of face-hobbed hypoid gears and its application to contact analysis and

stress calculation," *Mechanism and Machine Theory*, vol. 42, no. 6, pp. 668–690, 2007.

[14] S. Xie, *An Accurate Approach to Modeling the Genuine Tooth Surfaces of the Face-Milled Spiral Bevel and Hypoid Gears*. PhD thesis, Concordia University Montreal Quebec, Canada, 2011.

[15] M. Wasif, *A new approach to CNC programming for accurate multi-axis face-milling of hypoid gears*. PhD thesis, Concordia University, 2012.

[16] C. K. Chen, S. T. Chiou, Z. H. Fong, C. K. Lee, and C. H. Chen, "Mathematical model of curvature analysis for conjugate surfaces with generalized motion in three dimensions," *Proceedings of the Institution of Mechanical Engineers, Part C: Journal of Mechanical Engineering Science*, vol. 215, no. 4, pp. 487–502, 2001.

[17] F. Di Puccio, M. Gabiccini, and M. Guiggiani, "Alternative formulation of the theory of gearing," *Mechanism and machine theory*, vol. 40, no. 5, pp. 613–637, 2005.

[18] F. Di Puccio, M. Gabiccini, and M. Guiggiani, "An invariant approach for gear generation with supplemental motions," *Mechanism and machine theory*, vol. 42, no. 3, pp. 275–295, 2007.

[19] P. Wang and Y. Zhang, "An invariant approach for curvature analysis of conjugate surfaces," *Mechanism and Machine Theory*, vol. 64, pp. 175–199, 2013.

[20] D. R. Wu and J. s. Luo, *A geometric theory of conjugate tooth surfaces*. World Scientific, 1992.

[21] D. B. Dooner, "On the three laws of gearing," *Journal of Mechanical Design*, vol. 124, no. 4, pp. 733–744, 2002.

[22] N. Chen, "Curvatures and sliding ratios of conjugate surfaces," *Journal of Mechanical Design*, vol. 120, no. 1, pp. 126–132, 1998.

[23] Y. Hong-Sen and C. Wen-Teng, "Curvature analysis of spatial cam-follower mechanisms," *Mechanism and machine theory*, vol. 34, no. 2, pp. 319–339, 1999.

[24] N. Ito and K. Takahashi, "Differential geometrical conditions of hypoid gears with conjugate tooth surfaces," *Journal of Mechanical Design*, vol. 122, no. 3, pp. 323–330, 2000.

[25] F. Di Puccio, M. Gabiccini, and M. Guiggiani, "Generation and curvature analysis of conjugate surfaces via a new approach," *Mechanism and machine theory*, vol. 41, no. 4, pp. 382–404, 2006.

[26] F. Di Puccio, M. Gabiccini, and M. Guiggiani, "Comparison of different methods in gear curvature analysis using a new approach," *Proceedings of the Institution of Mechanical Engineers, Part C: Journal of Mechanical Engineering Science*, vol. 219, no. 11, pp. 1279–1294, 2005.

[27] S. Suh, W. Jih, H. Hong, and D. Chung, "Sculptured surface machining of spiral bevel gears with cnc milling," *International Journal of Machine Tools and Manufacture*, vol. 41, no. 6, pp. 833–850, 2001.

[28] S.-H. Suh, D.-H. Jung, S.-W. Lee, and E.-S. Lee, "Modelling, implementation, and manufacturing of spiral bevel gears with crown," *The International Journal of Advanced Manufacturing Technology*, vol. 21, no. 10-11, pp. 775–786, 2003.

[29] J. T. Alves, M. Guingand, and J.-P. de Vaujany, "Designing and manufacturing spiral bevel gears using 5-axis computer numerical control (cnc) milling machines," *Journal of Mechanical Design*, vol. 135, no. 2, p. 024502, 2013.

[30] R. Huston and J. Coy, "Ideal spiral bevel gears–a new approach to surface geometry," *Journal of Mechanical Design*, vol. 103, no. 1, pp. 127–132, 1981.

[31] R. Huston and J. J. Coy, "Surface geometry of circular cut spiral bevel gears," *Journal of Mechanical Design*, vol. 104, no. 4, pp. 743–748, 1982.

[32] R. Drago, "Discussion: Ideal spiral bevel gears–a new approach to surface geometry (huston, rl, and coy, jj, 1981, asme j. mech. des., 103, pp. 127–132)," *Journal of Mechanical Design*, vol. 103, no. 1, pp. 132–132, 1981.

[33] H. Tönshoff, C. Gey, and N. Rackow, "Flank milling optimization-the flamingo project," *Air & Space Europe*, vol. 3, no. 3, pp. 60–63, 2001.

[34] H.-T. Young, L.-C. Chuang, K. Gerschwiler, and S. Kamps, "A five-axis rough machining approach for a centrifugal impeller," *The International Journal of Advanced Manufacturing Technology*, vol. 23, no. 3-4, pp. 233–239, 2004.

[35] R. F. Harik, H. Gong, and A. Bernard, "5-axis flank milling: A state-of-the-art review," *Computer-Aided Design*, vol. 45, no. 3, pp. 796–808, 2013.

[36] D. Blackmore, M. C. Leu, and F. Shih, "Analysis and modelling of deformed swept volumes," *Computer-Aided Design*, vol. 26, no. 4, pp. 315–326, 1994.

[37] D. Blackmore, M. C. Leu, and L. P. Wang, "The sweep-envelope differential equation algorithm and its application to nc machining verification," *Computer-Aided Design*, vol. 29, no. 9, pp. 629–637, 1997.

[38] G. Wang, J. Sun, and X. Hua, "The sweep-envelope differential equation algorithm for general deformed swept volumes," *Computer Aided Geometric Design*, vol. 17, no. 5, pp. 399–418, 2000.

[39] K. Abdel-Malek and H.-J. Yeh, "Geometric representation of the swept volume using jacobian rank-deficiency conditions," *Computer-Aided Design*, vol. 29, no. 6, pp. 457–468, 1997.

[40] K. Abdel-Malek and S. Othman, "Multiple sweeping using the denavit–hartenberg representation method," *Computer-Aided Design*, vol. 31, no. 9, pp. 567–583, 1999.

[41] K. Abdel-Malek, W. Seaman, and H.-J. Yeh, "Nc verification of up to 5 axis machining processes using manifold stratification," *Journal of manufacturing science and engineering*, vol. 123, no. 1, pp. 99–109, 2001.

[42] V. Boltyanskii, "Envelopes, translated from the russian by rb brown," 1964.

[43] W. Wang and K. Wang, "Geometric modeling for swept volume of moving solids," *IEEE Computer Graphics and Applications*, vol. 6, no. 12, pp. 8–17, 1986.

[44] R. R. Martin and P. Stephenson, "Sweeping of three-dimensional objects," *Computer-Aided Design*, vol. 22, no. 4, pp. 223–234, 1990.

[45] J. D. Weld and M. C. Leu, "Geometric representation of swept volumes with application to polyhedral objects," *The International Journal of Robotics Research*, vol. 9, no. 5, pp. 105–117, 1990.

[46] Y. J. Kim, G. Varadhan, M. C. Lin, and D. Manocha, "Fast swept volume approximation of complex polyhedral models," *Computer-Aided Design*, vol. 36, no. 11, pp. 1013–1027, 2004.

[47] J. Rossignac, J. J. Kim, S. Song, K. Suh, and C. Joung, "Boundary of the volume swept by a free-form solid in screw motion," *Computer-Aided Design*, vol. 39, no. 9, pp. 745–755, 2007.

[48] H. Erdim and H. T. Ilieş, "Classifying points for sweeping solids," *Computer-Aided Design*, vol. 40, no. 9, pp. 987–998, 2008.

[49] B. Juttler and M. G. Wagner, "Computer-aided design with spatial rational b-spline motions," *Journal of Mechanical Design*, vol. 118, no. 2, pp. 193–201, 1996.

[50] J. Xia and Q. Ge, "On the exact representation of the boundary surfaces of the swept volume of a cylinder undergoing rational bézier and b-spline motions," *Journal of Mechanical Design*, vol. 123, no. 2, pp. 261–265, 2001.

[51] J. Yang and K. Abdel-Malek, "Approximate swept volumes of nurbs surfaces or solids," *Computer Aided Geometric Design*, vol. 22, no. 1, pp. 1–26, 2005.

[52] Z. C. Chen and W. Cai, "An efficient, accurate approach to representing cutter-swept envelopes and its applications to three-axis virtual milling of sculptured surfaces," *Journal of Manufacturing Science and Engineering*, vol. 130, no. 3, p. 031004, 2008.

[53] E. L. Bohez, N. T. H. Minh, B. Kiatsrithanakorn, P. Natasukon, H. Ruei-Yun, and L. T. Son, "The stencil buffer sweep plane algorithm for 5-axis cnc tool path verification," *Computer-Aided Design*, vol. 35, no. 12, pp. 1129–1142, 2003.

[54] J. W. Park, Y. H. Shin, and Y. C. Chung, "Hybrid cutting simulation via discrete vector model," *Computer-Aided Design*, vol. 37, no. 4, pp. 419–430, 2005.

[55] M. Yang and E. Lee, "Nc verification for wire-edm using an r-map," *Computer-Aided Design*, vol. 28, no. 9, pp. 733–740, 1996.

[56] J. C. Chiou and Y. S. Lee, "A shape-generating approach for multi-axis machining g-buffer models," *Computer-Aided Design*, vol. 31, no. 12, pp. 761–776, 1999.

[57] S. R. Maeng, N. Baek, S. Y. Shin, and B. K. Choi, "A z-map update method for linearly moving tools," *Computer-Aided Design*, vol. 35, no. 11, pp. 995–1009, 2003.

[58] Y. C. Chung, J. W. Park, H. Shin, and B. K. Choi, "Modeling the surface swept by a generalized cutter for nc verification," *Computer-Aided Design*, vol. 30, no. 8, pp. 587–594, 1998.

[59] D. Roth, S. Bedi, F. Ismail, and S. Mann, "Surface swept by a toroidal cutter during 5-axis machining," *Computer-Aided Design*, vol. 33, no. 1, pp. 57–63, 2001.

[60] S. Mann and S. Bedi, "Generalization of the imprint method to general surfaces of revolution for nc machining," *Computer-aided design*, vol. 34, no. 5, pp. 373–378, 2002.

[61] S. W. Lee and A. Nestler, "Complete swept volume generation, part i: Swept volume of a piecewise c1-continuous cutter at five-axis milling via gauss map," *Computer-Aided Design*, vol. 43, no. 4, pp. 427–441, 2011.

[62] S. W. Lee and A. Nestler, "Complete swept volume generationpart ii: Nc simulation of self-penetration via comprehensive analysis of envelope profiles," *Computer-Aided Design*, vol. 43, no. 4, pp. 442–456, 2011.

[63] Z. J. Hu and Z. K. Ling, "Swept volumes generated by the natural quadric surfaces," *Computers & graphics*, vol. 20, no. 2, pp. 263–274, 1996.

[64] J. C. Chiou and Y. S. Lee, "Swept surface determination for five-axis numerical control machining," *International Journal of Machine Tools and Manufacture*, vol. 42, no. 14, pp. 1497–1507, 2002.

[65] J. C. Chiou, "Accurate tool position for five-axis ruled surface machining by swept envelope approach," *Computer-Aided Design*, vol. 36, no. 10, pp. 967–974, 2004.

[66] J. C. Chiou and Y. S. Lee, "Optimal tool orientation for five-axis tool-end machining by swept envelope approach," *Journal of Manufacturing Science and Engineering*, vol. 127, no. 4, pp. 810–818, 2005.

[67] C. Lartigue, E. Duc, and A. Affouard, "Tool path deformation in 5-axis flank milling using envelope surface," *Computer-Aided Design*, vol. 35, no. 4, pp. 375–382, 2003.

[68] K. Weinert, S. Du, P. Damm, and M. Stautner, "Swept volume generation for the simulation of machining processes," *International Journal of Machine Tools and Manufacture*, vol. 44, no. 6, pp. 617–628, 2004.

[69] S. Du, T. Surmann, O. Webber, and K. Weinert, "Formulating swept profiles for five-axis tool motions," *International Journal of Machine Tools and Manufacture*, vol. 45, no. 7, pp. 849–861, 2005.

[70] L. Zhu, G. Zheng, and H. Ding, "Formulating the swept envelope of rotary cutter undergoing general spatial motion for multi-axis nc machining," *International Journal of Machine Tools and Manufacture*, vol. 49, no. 2, pp. 199–202, 2009.

[71] H. Gong and N. Wang, "Analytical calculation of the envelope surface for generic milling tools directly from cl-data based on the moving frame method," *Computer-Aided Design*, vol. 41, no. 11, pp. 848–855, 2009.

[72] L. Zhu, X. Zhang, G. Zheng, and H. Ding, "Analytical expression of the swept surface of a rotary cutter using the envelope theory of sphere congruence," *Journal of Manufacturing Science and Engineering*, vol. 131, no. 4, p. 041017, 2009.

[73] E. Aras, "Generating cutter swept envelopes in five-axis milling by two-parameter families of spheres," *Computer-Aided Design*, vol. 41, no. 2, pp. 95–105, 2009.

[74] J. Rossignac and J. J. Kim, "Helsweeper: Screw-sweeps of canal surfaces," *Computer-Aided Design*, vol. 44, no. 2, pp. 113–122, 2012.

[75] S. Izumiya, K. Saji, and N. Takeuchi, "Circular surfaces," *Advances in Geometry*, vol. 7, no. 2, pp. 295–313, 2007.

[76] L. Cui, D. Wang, and J. S. Dai, "Kinematic geometry of circular surfaces with a fixed radius based on euclidean invariants," *Journal of Mechanical Design*, vol. 131, no. 10, p. 101009, 2009.

[77] Y. Zhou and Z. C. Chen, "A new geometric meshing theory for a closed-form vector representation of the face-milled generated gear tooth surface and its curvature analysis," *Mechanism and Machine Theory*, vol. 83, pp. 91–108, 2015.

[78] A. STANDARD, "Design manual for bevel gears," *ANSI/AGMA*, pp. 2005–D03, 2005.

[79] H. Stadtfeld, *Advanced Bevel Gear Technology: Manufacturing, Inspection and Optimization; Collected Publications*. The Gleason works, 2000.

[80] M. Peternell, H. Pottmann, and B. Ravani, "On the computational geometry of ruled surfaces," *Computer-Aided Design*, vol. 31, no. 1, pp. 17–32, 1999.

[81] C. Menzel, S. Bedi, and S. Mann, "Triple tangent flank milling of ruled surfaces," *Computer-Aided Design*, vol. 36, no. 3, pp. 289–296, 2004.

[82] C. Li, S. Mann, and S. Bedi, "Error measurements for flank milling," *Computer-Aided Design*, vol. 37, no. 14, pp. 1459–1468, 2005.

[83] P.-Y. Pechard, C. Tournier, C. Lartigue, and J.-P. Lugarini, "Geometrical deviations versus smoothness in 5-axis high-speed flank milling," *International Journal of Machine Tools and Manufacture*, vol. 49, no. 6, pp. 454–461, 2009.

[84] O. R. Tutunea-Fatan and M. S. H. Bhuiya, "Comparing the kinematic efficiency of five-axis machine tool configurations through nonlinearity errors," *Computer-Aided Design*, vol. 43, no. 9, pp. 1163–1172, 2011.

[85] H. Liang, H. Hong, and J. Svoboda, "A combined 3d linear and circular interpolation technique for multi-axis cnc machining," *Journal of manufacturing science and engineering*, vol. 124, no. 2, pp. 305–312, 2002.

[86] O. R. Tutunea-Fatan and H.-Y. Feng, "Determination of geometry-based errors for interpolated tool paths in five-axis surface machining," *Journal of manufacturing science and engineering*, vol. 127, no. 1, pp. 60–67, 2005.

[87] Y. Koren and R.-S. Lin, "Five-axis surface interpolators," *CIRP Annals-Manufacturing Technology*, vol. 44, no. 1, pp. 379–382, 1995.

[88] S. Mann, S. Bedi, G. Israeli, and X. L. Zhou, "Machine models and tool motions for simulating five-axis machining," *Computer-Aided Design*, vol. 42, no. 3, pp. 231–237, 2010.

[89] J. Craig, *Introduction to Robotics: Mechanics and Control*. Addison-Wesley series in electrical and computer engineering: control engineering, Pearson/Prentice Hall, 2005.

Appendix A

HTM and its derivatives for generated face-milled approach

According to the kinematic relation described in Fig. 3.3, the HTM from S_g to S_b is calculated as

$$\begin{aligned}\mathbf{M}_{\mathrm{bg}}(\phi_c) =& \mathbf{R}_Z(-\phi_b)\cdot\mathbf{T}\begin{pmatrix}0\\0\\-\Delta X_D\end{pmatrix}\cdot\mathbf{R}_Y\left(-(\frac{\pi}{2}-\gamma_m)\right)\cdot\mathbf{T}\begin{pmatrix}0\\\Delta E_m\\-\Delta X_B\end{pmatrix}\\ &\cdot\mathbf{R}_Z(\phi_c)\cdot\mathbf{T}\begin{pmatrix}S_r\cdot\cos q_2\\S_r\cdot\sin q_2\\0\end{pmatrix}\end{aligned} \tag{A.1}$$

where $\mathbf{R}$ and $\mathbf{T}$ are rotation and translation HTM, respectively [89]. For example, $\mathbf{R}_Z(-\phi_b)$ is the rotation HTM by rotating along Z axis with a angle $-\phi_b$, and $\mathbf{T}\left([0,\ 0,\ -\Delta X_D]^T\right)$ is the translation HTM with the translational

vector $[0,\ 0,\ -\Delta X_D]^T$. They are given as

$$\mathbf{T}\begin{pmatrix} S_r \cdot \cos q_2 \\ S_r \cdot \sin q_2 \\ 0 \end{pmatrix} = \begin{bmatrix} 1 & 0 & 0 & S_r \cdot \cos q_2 \\ 0 & 1 & 0 & S_r \cdot \sin q_2 \\ 0 & 0 & 1 & 0 \\ 0 & 0 & 0 & 1 \end{bmatrix}$$

$$\mathbf{R}_Z(\phi_c) = \begin{bmatrix} \cos\phi_c & -\sin\phi_c & 0 & 0 \\ \sin\phi_c & \cos\phi_c & 0 & 0 \\ 0 & 0 & 1 & 0 \\ 0 & 0 & 0 & 1 \end{bmatrix}$$

$$\mathbf{T}\begin{pmatrix} 0 \\ \Delta E_m \\ -\Delta X_B \end{pmatrix} = \begin{bmatrix} 1 & 0 & 0 & 0 \\ 0 & 1 & 0 & \Delta E_m \\ 0 & 0 & 1 & -\Delta X_B \\ 0 & 0 & 0 & 1 \end{bmatrix}$$

$$\mathbf{R}_Y\left(-(\frac{\pi}{2} - \gamma_m)\right) = \begin{bmatrix} \sin\gamma_m & 0 & -\cos\gamma_m & 0 \\ 0 & 1 & 0 & 0 \\ \cos\gamma_m & 0 & \sin\gamma_m & 0 \\ 0 & 0 & 0 & 1 \end{bmatrix}$$

$$\mathbf{T}\begin{pmatrix} 0 \\ 0 \\ -\Delta X_D \end{pmatrix} = \begin{bmatrix} 1 & 0 & 0 & 0 \\ 0 & 1 & 0 & 0 \\ 0 & 0 & 1 & -\Delta X_D \\ 0 & 0 & 0 & 1 \end{bmatrix}$$

$$\mathbf{R}_Z(-\phi_b) = \begin{bmatrix} \cos\phi_b & \sin\phi_b & 0 & 0 \\ -\sin\phi_b & \cos\phi_b & 0 & 0 \\ 0 & 0 & 1 & 0 \\ 0 & 0 & 0 & 1 \end{bmatrix}$$

With (A.1), the components of $\mathbf{M}_{\mathrm{bg}}(\phi_c)$ are calculated as

$$\begin{aligned}
M_{11} &= \cos\phi_b \cdot \cos\phi_c \cdot \sin\gamma_m + \sin\phi_b \cdot \sin\phi_c \\
M_{12} &= -\cos\phi_b \cdot \sin\phi_c \cdot \sin\gamma_m + \sin\phi_b \cdot \cos\phi_c \\
M_{13} &= -\cos\phi_b \cdot \cos\gamma_m \\
M_{14} &= N_1 \cdot \cos\phi_b \cdot \sin\gamma_m + N_2 \cdot \sin\phi_b + N_3 \\
M_{21} &= -\sin\phi_b \cdot \cos\phi_c \cdot \sin\gamma_m + \cos\phi_b \cdot \sin\phi_c \\
M_{22} &= \sin\phi_b \cdot \sin\phi_c \cdot \sin\gamma_m + \cos\phi_b \cdot \cos\phi_c \\
M_{23} &= \sin\phi_b \cdot \cos\gamma_m \\
M_{24} &= -N_1 \cdot \sin\phi_b \cdot \sin\gamma_m + N_2 \cdot \cos\phi_b + N_4 \\
M_{31} &= \cos\phi_c \cdot \cos\gamma_m \\
M_{32} &= -\sin\phi_c \cdot \cos\gamma_m \\
M_{33} &= \sin\gamma_m \\
M_{34} &= N_1 \cdot \cos\gamma_m - \Delta X_B \cdot \sin\gamma_m - \Delta X_D
\end{aligned} \tag{A.2}$$

where

$N_1 = S_r \cdot \cos(q_2 + \phi_c), N_2 = S_r \cdot \sin(q_2 + \phi_c),$

$N_3 = \Delta E_m \cdot \sin\phi_b + \Delta X_B \cdot \cos\phi_b \cdot \cos\gamma_m, N_4 = \Delta E_m \cdot \cos\phi_b - \Delta X_B \cdot \sin\phi_b \cdot \cos\gamma_m$

In order to calculate $\mathbf{v}_h(h, \phi_c)$, $dM_{i3}/d\phi_c$ and $dM_{i4}/d\phi_c$ $(i = 1, 2, 3)$ are calculated according to (A.2) as

$$
\begin{aligned}
\frac{dM_{13}}{d\phi_c} &= \sin\phi_b \cdot \cos\gamma_m \cdot \frac{d\phi_b}{d\phi_c} \\
\frac{dM_{23}}{d\phi_c} &= \cos\phi_b \cdot \cos\gamma_m \cdot \frac{d\phi_b}{d\phi_c} \\
\frac{dM_{33}}{d\phi_c} &= 0 \\
\frac{dM_{14}}{d\phi_c} &= N_2 \cdot \cos\phi_b \cdot \left(\frac{d\phi_b}{d\phi_c} - \sin\gamma_m\right) + N_1 \cdot \sin\phi_b \cdot \left(1 - \sin\gamma_m \cdot \frac{d\phi_b}{d\phi_c}\right) + N_4 \cdot \frac{d\phi_b}{d\phi_c} \\
\frac{dM_{24}}{d\phi_c} &= N_2 \cdot \sin\phi_b \cdot \left(\sin\gamma_m - \frac{d\phi_b}{d\phi_c}\right) + N_1 \cdot \cos\phi_b \cdot \left(1 - \sin\gamma_m \cdot \frac{d\phi_b}{d\phi_c}\right) - N_3 \cdot \frac{d\phi_b}{d\phi_c} \\
\frac{dM_{34}}{d\phi_c} &= -N_2 \cdot \cos\gamma_m
\end{aligned}
\tag{A.3}
$$

For gear curvature analysis, $d^2M_{i3}/d\phi_c^2$ and $d^2M_{i4}/d\phi_c^2$ ($i = 1, 2, 3$) are cal-

culated according to Eq. (A.3) as

$$
\begin{aligned}
\frac{d^2M_{13}}{d\phi_c^2} &= \cos\phi_b \cdot \cos\gamma_m \cdot \left(\frac{d\phi_b}{d\phi_c}\right)^2 + \sin\phi_b \cdot \cos\gamma_m \cdot \frac{d^2\phi_b}{d\phi_c^2} \\
\frac{d^2M_{23}}{d\phi_c^2} &= -\sin\phi_b \cdot \cos\gamma_m \cdot \left(\frac{d\phi_b}{d\phi_c}\right)^2 + \cos\phi_b \cdot \cos\gamma_m \cdot \frac{d^2\phi_b}{d\phi_c^2} \\
\frac{d^2M_{33}}{d\phi_c^2} &= 0 \\
\frac{d^2M_{14}}{d\phi_c^2} &= M_{24} \cdot \frac{d^2\phi_b}{d\phi_c^2} - M_{14} \cdot \left(\frac{d\phi_b}{d\phi_c}\right)^2 + 2 \cdot (N_1 \cdot \cos\phi_b + N_2 \cdot \sin\phi_b \cdot \sin\gamma_m) \cdot \frac{d\phi_b}{d\phi_c} \\
&\quad - M_{14} + N_3 \\
\frac{d^2M_{24}}{d\phi_c^2} &= -M_{14} \cdot \frac{d^2\phi_b}{d\phi_c^2} - M_{24} \cdot \left(\frac{d\phi_b}{d\phi_c}\right)^2 + 2 \cdot (-N_1 \cdot \sin\phi_b + N_2 \cdot \cos\phi_b \cdot \sin\gamma_m) \cdot \frac{d\phi_b}{d\phi_c} \\
&\quad - M_{24} + N_4 \\
\frac{d^2M_{34}}{d\phi_c^2} &= -N_1 \cdot \cos\gamma_m
\end{aligned}
\tag{A.4}
$$

Appendix B

The derivation of $\dfrac{d\mathbf{n}_{\mathrm{m,g}}(\varphi)}{d\varphi}$

According to Eqs. (3.41) and (4.24), we have

$$\mathbf{n}_{\mathrm{m,g}}(\varphi) = \pm \frac{\mathbf{N}_{\varphi,\mathrm{g}} \times \mathbf{N}_{h,\mathrm{g}}}{\mid \mathbf{N}_{\varphi,\mathrm{g}} \times \mathbf{N}_{h,\mathrm{g}} \mid}\Bigg|_{h=h_{\mathrm{m}}(\varphi)}. \tag{B.1}$$

Assuming that $\mathbf{T}_{\mathrm{m}}(\varphi) = (\mathbf{N}_{\varphi,\mathrm{g}} \times \mathbf{N}_{h,\mathrm{g}})\Big|_{h=h_{\mathrm{m}}(\varphi)}$, the derivative of Eq. (B.1) with respect to φ can be obtained as

$$\begin{aligned}
\frac{d\mathbf{n}_{\mathrm{m,g}}(\varphi)}{d\varphi} &= \pm \frac{\mathbf{T}'_{\mathrm{m}} \cdot \mid \mathbf{T}_{\mathrm{m}} \mid - \mathbf{T}_{\mathrm{m}} \cdot \mid \mathbf{T}_{\mathrm{m}} \mid'}{\mid \mathbf{T}_{\mathrm{m}} \mid^2} \\
&= \pm \frac{\mathbf{T}'_{\mathrm{m}} \cdot \mid \mathbf{T}_{\mathrm{m}} \mid - \mathbf{T}_{\mathrm{m}} \cdot \dfrac{\mathbf{T}_{\mathrm{m}} \cdot \mathbf{T}'_{\mathrm{m}}}{\mid \mathbf{T}_{\mathrm{m}} \mid}}{\mid \mathbf{T}_{\mathrm{m}} \mid^2} \\
&= \pm \frac{\mathbf{T}'_{\mathrm{m}} \cdot \mid \mathbf{T}_{\mathrm{m}} \mid^2 - \mathbf{T}_{\mathrm{m}} \cdot (\mathbf{T}_{\mathrm{m}} \cdot \mathbf{T}'_{\mathrm{m}})}{\mid \mathbf{T}_{\mathrm{m}} \mid^3}.
\end{aligned} \tag{B.2}$$

In order to calculate $\dfrac{d\mathbf{n}_{\mathrm{m,g}}(\varphi)}{d\varphi}$, $\mathbf{T}_{\mathrm{m}}(\varphi)$ and $\mathbf{T}'_{\mathrm{m}}$ are calculated as follows. According to Eq. (3.42), we have

$$
\begin{aligned}
\mathbf{T}_{\mathrm{m}}(\varphi) &= \left(\mathbf{N}_{\varphi,\mathrm{g}} \times \mathbf{N}_{h,\mathrm{g}}\right)\Big|_{h=h_{\mathrm{m}}(\varphi)} \\
&= \pm \mathrm{r}_{\mathrm{ly,p}} \cdot \tan\alpha_{\mathrm{g}} \cdot \left(\frac{d\mathbf{y}_{\mathrm{p}}}{d\varphi} \times \mathbf{y}_{\mathrm{p}}\right) + \mathrm{r}_{\mathrm{ly,p}} \cdot \left(\frac{d\mathbf{y}_{\mathrm{p}}}{d\varphi} \times \mathbf{z}_{\mathrm{p}}\right) \\
&\pm h_{\mathrm{m}} \cdot \tan\alpha_{\mathrm{g}} \cdot \left(\frac{d\mathbf{z}_{\mathrm{p}}}{d\varphi} \times \mathbf{y}_{\mathrm{p}}\right) + h_{\mathrm{m}} \cdot \left(\frac{d\mathbf{z}_{\mathrm{p}}}{d\varphi} \times \mathbf{z}_{\mathrm{p}}\right) \\
&+ \frac{d\mathbf{o}_{\mathrm{p}}}{d\varphi} \times \left(\pm \tan\alpha_{\mathrm{g}} \cdot \mathbf{y}_{\mathrm{p}} + \mathbf{z}_{\mathrm{p}}\right).
\end{aligned}
\tag{B.3}
$$

The derivative of $\mathbf{T}_{\mathrm{m}}(\varphi)$ with respect to φ can be calculated as

$$
\begin{aligned}
\mathbf{T}'_{\mathrm{m}} = \frac{d\mathbf{T}_{\mathrm{m}}(\varphi)}{d\varphi} &= \pm \frac{d\mathrm{r}_{\mathrm{ly,p}}}{d\varphi} \cdot \tan\alpha_{\mathrm{g}} \cdot \left(\frac{d\mathbf{y}_{\mathrm{p}}}{d\varphi} \times \mathbf{y}_{\mathrm{p}}\right) \pm \mathrm{r}_{\mathrm{ly,p}} \cdot \tan\alpha_{\mathrm{g}} \cdot \left(\frac{d^2\mathbf{y}_{\mathrm{p}}}{d\varphi^2} \times \mathbf{y}_{\mathrm{p}}\right) \\
&+ \frac{d\mathrm{r}_{\mathrm{ly,p}}}{d\varphi} \cdot \left(\frac{d\mathbf{y}_{\mathrm{p}}}{d\varphi} \times \mathbf{z}_{\mathrm{p}}\right) + \mathrm{r}_{\mathrm{ly,p}} \cdot \left(\frac{d^2\mathbf{y}_{\mathrm{p}}}{d\varphi^2} \times \mathbf{z}_{\mathrm{p}} + \frac{d\mathbf{y}_{\mathrm{p}}}{d\varphi} \times \frac{d\mathbf{z}_{\mathrm{p}}}{d\varphi}\right) \\
&\pm \frac{dh_{\mathrm{m}}}{d\varphi} \cdot \tan\alpha_{\mathrm{g}} \cdot \left(\frac{d\mathbf{z}_{\mathrm{p}}}{d\varphi} \times \mathbf{y}_{\mathrm{p}}\right) \pm h_{\mathrm{m}} \cdot \tan\alpha_{\mathrm{g}} \cdot \left(\frac{d^2\mathbf{z}_{\mathrm{p}}}{d\varphi^2} \times \mathbf{y}_{\mathrm{p}} + \frac{d\mathbf{z}_{\mathrm{p}}}{d\varphi} \times \frac{d\mathbf{y}_{\mathrm{p}}}{d\varphi}\right) \\
&+ \frac{dh_{\mathrm{m}}}{d\varphi} \cdot \left(\frac{d\mathbf{z}_{\mathrm{p}}}{d\varphi} \times \mathbf{z}_{\mathrm{p}}\right) + h_{\mathrm{m}} \cdot \left(\frac{d^2\mathbf{z}_{\mathrm{p}}}{d\varphi^2} \times \mathbf{z}_{\mathrm{p}}\right) + \frac{d^2\mathbf{o}_{\mathrm{p}}}{d\varphi^2} \times \left(\pm \tan\alpha_{\mathrm{g}} \cdot \mathbf{y}_{\mathrm{p}} + \mathbf{z}_{\mathrm{p}}\right) \\
&+ \frac{d\mathbf{o}_{\mathrm{p}}}{d\varphi} \times \left(\pm \tan\alpha_{\mathrm{g}} \cdot \frac{d\mathbf{y}_{\mathrm{p}}}{d\varphi} + \frac{d\mathbf{z}_{\mathrm{p}}}{d\varphi}\right).
\end{aligned}
\tag{B.4}
$$

It is worthwhile mentioning that the derivatives of $\dfrac{d\mathbf{T}_{\mathrm{m}}(\varphi)}{d\varphi}$ and $\dfrac{d\left(\mathbf{N}_{\varphi,\mathrm{g}} \times \mathbf{N}_{h,\mathrm{g}}\right)}{d\varphi}$ are different. Because both $\mathrm{r}_{\mathrm{ly,p}}$ and h_{m} in the former item are dependent on φ, but both $\mathrm{r}_{\mathrm{ly,p}}$ and h_{m} in the later item are independent of φ. According to Eqs. (3.34), (3.35) and (4.23), we have

$$
\begin{aligned}
\frac{dh_{\mathrm{m}}(\varphi)}{d\varphi} &= \frac{1}{2} \cdot \frac{dr_{\mathrm{q}}}{d\varphi} \cdot \left(\tan(\gamma - \gamma_{\mathrm{r}}) + \tan(\gamma_{\mathrm{o}} - \gamma)\right) \\
\frac{d\mathrm{r}_{\mathrm{ly,p}}}{d\varphi} &= \pm \tan\alpha_{\mathrm{g}} \cdot \frac{dh_{\mathrm{m}}(\varphi)}{d\varphi}.
\end{aligned}
\tag{B.5}
$$

According to Eq. (3.43), we have

$$
\begin{aligned}
\frac{d^2\mathbf{x}_{\mathrm{p}}(\varphi)}{d\varphi^2} &= \sin\Gamma\cdot\frac{d^2\theta_{\mathrm{s}}}{d\varphi^2}\cdot\begin{bmatrix}-\sin(\theta_{\mathrm{ms}}+\theta_{\mathrm{s}})\\ \cos(\theta_{\mathrm{ms}}+\theta_{\mathrm{s}})\\ 0\end{bmatrix}-\sin\Gamma\cdot\left(\frac{d\theta_{\mathrm{s}}}{d\varphi}\right)^2\cdot\begin{bmatrix}\cos(\theta_{\mathrm{ms}}+\theta_{\mathrm{s}})\\ \sin(\theta_{\mathrm{ms}}+\theta_{\mathrm{s}})\\ 0\end{bmatrix}\\
\frac{d^2\mathbf{y}_{\mathrm{p}}(\varphi)}{d\varphi^2} &= \frac{d^2\theta_{\mathrm{s}}}{d\varphi^2}\cdot\begin{bmatrix}\cos(\theta_{\mathrm{ms}}+\theta_{\mathrm{s}})\\ \sin(\theta_{\mathrm{ms}}+\theta_{\mathrm{s}})\\ 0\end{bmatrix}+\left(\frac{d\theta_{\mathrm{s}}}{d\varphi}\right)^2\cdot\begin{bmatrix}-\sin(\theta_{\mathrm{ms}}+\theta_{\mathrm{s}})\\ \cos(\theta_{\mathrm{ms}}+\theta_{\mathrm{s}})\\ 0\end{bmatrix}\\
\frac{d^2\mathbf{z}_{\mathrm{p}}(\varphi)}{d\varphi^2} &= \cos\Gamma\cdot\frac{d^2\theta_{\mathrm{s}}}{d\varphi^2}\cdot\begin{bmatrix}-\sin(\theta_{\mathrm{ms}}+\theta_{\mathrm{s}})\\ \cos(\theta_{\mathrm{ms}}+\theta_{\mathrm{s}})\\ 0\end{bmatrix}-\cos\Gamma\cdot\left(\frac{d\theta_{\mathrm{s}}}{d\varphi}\right)^2\cdot\begin{bmatrix}\cos(\theta_{\mathrm{ms}}+\theta_{\mathrm{s}})\\ \sin(\theta_{\mathrm{ms}}+\theta_{\mathrm{s}})\\ 0\end{bmatrix}\\
\frac{d^2\mathbf{o}_{\mathrm{p}}(\varphi)}{d\varphi^2} &= \frac{d^2\mathbf{q}_{\mathrm{s}}}{d\varphi^2}-\tan(\Gamma-\Gamma_{\mathrm{r}})\cdot\left(\frac{d^2r_{\mathrm{q}}}{d\varphi^2}\cdot\mathbf{z}_{\mathrm{p}}+2\cdot\frac{dr_{\mathrm{q}}}{d\varphi}\cdot\frac{d\mathbf{z}_{\mathrm{p}}}{d\varphi}\right)-H_{\mathrm{s}}\cdot\frac{d^2\mathbf{z}_{\mathrm{p}}}{d\varphi^2}.
\end{aligned}
\tag{B.6}
$$

According to Eq. (3.25), we have

$$
\frac{d^2\mathbf{q}_{\mathrm{s}}(\varphi)}{d\varphi^2}=\sin\Gamma\cdot\begin{bmatrix}\left\{\cos(\theta_{\mathrm{ms}}+\theta_{\mathrm{s}})\cdot\dfrac{d^2r_{\mathrm{q}}}{d\varphi^2}-2\cdot\sin(\theta_{\mathrm{ms}}+\theta_{\mathrm{s}})\cdot\dfrac{d\theta_{\mathrm{s}}}{d\varphi}\cdot\dfrac{dr_{\mathrm{q}}}{d\varphi}\right.\\ \left.-r_{\mathrm{q}}\cdot\left[\sin(\theta_{\mathrm{ms}}+\theta_{\mathrm{s}})\cdot\dfrac{d^2\theta_{\mathrm{s}}}{d\varphi^2}+\cos(\theta_{\mathrm{ms}}+\theta_{\mathrm{s}})\cdot\left(\dfrac{d\theta_{\mathrm{s}}}{d\varphi}\right)^2\right]\right\}\\ \left\{\sin(\theta_{\mathrm{ms}}+\theta_{\mathrm{s}})\cdot\dfrac{d^2r_{\mathrm{q}}}{d\varphi^2}+2\cdot\cos(\theta_{\mathrm{ms}}+\theta_{\mathrm{s}})\cdot\dfrac{d\theta_{\mathrm{s}}}{d\varphi}\cdot\dfrac{dr_{\mathrm{q}}}{d\varphi}\right.\\ \left.+r_{\mathrm{q}}\cdot\left[\cos(\theta_{\mathrm{ms}}+\theta_{\mathrm{s}})\cdot\dfrac{d^2\theta_{\mathrm{s}}}{d\varphi^2}-\sin(\theta_{\mathrm{ms}}+\theta_{\mathrm{s}})\cdot\left(\dfrac{d\theta_{\mathrm{s}}}{d\varphi}\right)^2\right]\right\}\\ \cot\Gamma\cdot\dfrac{d^2r_{\mathrm{q}}}{d\varphi^2}\end{bmatrix}
\tag{B.7}
$$

where

$$\frac{d^2 r_{\mathrm{q}}}{d\varphi^2} = -\frac{1}{r_{\mathrm{q}}} \cdot \left(\frac{dr_{\mathrm{q}}}{d\varphi}\right)^2 + \frac{r_{\mathrm{c}}}{r_{\mathrm{q}}} \cdot \left[r_{\mathrm{c}} - \mathrm{q_{cx}} \cdot \cos\left(\theta_{\mathrm{mc}} + \theta_{\mathrm{t}} + \varphi\right) - \mathrm{q_{cy}} \cdot \sin\left(\theta_{\mathrm{mc}} + \theta_{\mathrm{t}} + \varphi\right)\right]$$

$$\frac{d^2 \theta_{\mathrm{s}}}{d\varphi^2} = \frac{-2}{r_{\mathrm{q}}} \cdot \frac{d\theta_{\mathrm{s}}}{d\varphi} \cdot \frac{dr_{\mathrm{q}}}{d\varphi} + \frac{r_{\mathrm{c}} \cdot \csc\Gamma}{r_{\mathrm{q}}^2} \cdot \left[-\mathrm{q_{cx}} \cdot \sin\left(\theta_{\mathrm{mc}} + \theta_{\mathrm{t}} + \varphi\right) + \mathrm{q_{cy}} \cdot \cos\left(\theta_{\mathrm{mc}} + \theta_{\mathrm{t}} + \varphi\right)\right].$$

Submitting Eqs. (3.43), (B.5) $\sim$ (B.7) into Eq. (B.4), $\dfrac{d\mathbf{T}_{\mathrm{m}}(\varphi)}{d\varphi}$ can be obtained. Subsequently, $\dfrac{d\mathbf{n}_{\mathrm{m,g}}(\varphi)}{d\varphi}$ can be obtained by submitting Eqs. (B.3) and Eq. (B.4) into Eq. (B.2).